ANUL LI **2006**

S T U D I A

UNIVERSITATIS BABEŞ–BOLYAI

PHYSICA

1

Editorial Office: 400015 – Cluj–Napoca Republicii no. 24, Phone: 0264-405352

SUMAR - SOMMAIRE - CONTENTS - INHALT

STUDIA UNIVERSITATIS BABEŞ-BOLYAI, PHYSICA, LI, 1, 2006

REVISED EQUILIBRIUM STRUCTURES OF SMALL WATER CLUSTERS

TITUS A. BEU*, ANA-MARIA FLORESCU

ABSTRACT. New ground state structures of small water clusters, $n \leq 20$, obtained by the recently published site-site model potential TIP5P [1], are reported. The binding energies and the symmetry of the obtained configurations are compared with data reported for previous model potentials. The TIP5P potential is found to generally yield more stable structures.

1. Introduction

We have performed equilibrium structure calculations for water clusters of sizes $n = 2 \div 20$ using the recent TIP5P (transferable intermolecular potential) model of Mahoney and Jorgensen [1], with a view to subsequent IR-spectroscopy calculations. We carried out potential energy minimizations using a steepest descent-type approach (with analytically evaluated gradients) started from randomly chosen initial configurations. The configurations are described by the center of mass positions and the Euler angles of the component molecules. Typically, several millions of minimizations have been necessary to reach the global minima. We compare our results with the water clusters reported by Wales and Hodges [3], obtained by Monte Carlo minimization and using the already "classical" TIP4P potential model [2], and with the structures obtained by Maheshwary and al [4] by first principles methods.

2. Potential Model

Due to the great interest in simulating water and aqueous solutions, there have been elaborated several potential functions for describing the interactions within the water dimer. The most frequently used potentials involve a rigid water monomer with several interaction sites. These site-site potentials have been generally obtained by fitting their parameters to the experimental temperature and pressure dependences of the liquid density, dielectric constant, dipole and quadrupole moment, and the OO and OH radial distribution functions, respectively. The most accurate potential functions have turned out to be the TIP4P and TIP5P models. The TIP4P model gives better results for the dipole and quadrupole moment, while TIP5P yields better results

* University "Babeş-Bolyai", Faculty of Physics M. Kogălniceanu 1, RO-3400 Cluj-Napoca, Romania
E-mail: tbeu@phys.ubbcluj.ro

for the radial distribution functions and for the temperature dependence of the density. Both models imply a rigid monomer with the OH bond length of 0.9572 Å and the HOH bond angle of 104.52°, and having, re spectively, four and five interaction sites. The charge on the O atom is transferred to the supplementary interaction sites, the O-O interactions being modeled by Lennard-Jones contributions. All other sites interact by electrostatic potentials.

The two supplementary interaction sites featured by the TIP5P model are located tetragonally along the lone-pair directions, 0.7Å apart from the oxygen atom, in a plane perpendicular to that of the O-H bonds. An electrostatic charge of 0.241e is placed on the hydrogen atoms, whereas the supplementary sites are assigned equal charges of opposite sign. The parameters of the Lennard-Jones potential are $\varepsilon = 0.6694$ kJ/mol and $\sigma = 3.12$ Å. The TIP4P model [2] has only one supplementary interaction site, located on the bisector of the HOH bond angle at a 0.15 Å from the oxygen, carrying an electrostatic charge of 0.520e.

Table 1.
Binding energies (in kJ/mol) of small $(H_2O)_n$ clusters

n	TIP4P	TIP5P	*n*	TIP4P	TIP5P
2	-26.087	-28.388	12	-492.904	-494.909
3	-69.993	-62.728	13	-532.967	-535.489
4	-116.590	-118.957	14	-582.991	-591.653
5	-152.109	-159.505	15	-628.367	-631.910
6	-197.779	-197.941	16	-681.187	-684.504
7	-243.571	-242.071	17	-723.802	-726.355
8	-305.516	-303.203	18	-773.226	-780.035
9	-344.433	-349.546	19	-821.030	-822.705
10	-391.020	-399.050	20	-872.982	-869.481
11	-431.486	-440.594			

3. Results and Discussion

For clusters composed of 2 to 5 water monomers, we have obtained the same geometric structures as those reported by Hodges and Wales [3], but slightly lower binding energy values. The dimer has an almost linear hydrogen bond, with an O-O distance of 2.715 Å for TIP5P and 2.748 Å for TIP4P. For the TIP5P trimer the energy is higher than the one obtained by using the TIP4P potential and both structures have a triangular shape (figure 1). The tetramer has a square shape with C_2 symmetry (figure 1). The pentamer is a pentagon with an apparent (but not rigorous) symmetry.

The TIP5P hexamer is a regular hexagon with D_{2h} symmetry, quite different from the cage-like TIP4P hexamer, and also with a lower binding

energy (roughly by 1.5 kJ/mol- Table 1). The TIP5P configurations with n = 3, 7 and 8 are the only ones featuring higher energies than those yielded by the TIP4P model. The H_2O heptamer is a cube-like structure with a missing corner, while the octamer is a cube with D_{2d} symmetry (figure 2). The cubic structure of the octamer suggests a high degree of stability, since the heptamer and nonamer structures are based on it.

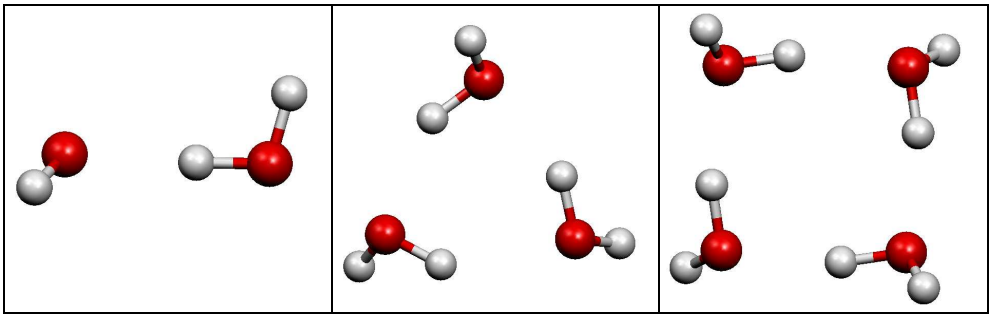

Figure 1. Geometric structures of the TIP5P water dimer, trimer, and tetramer.

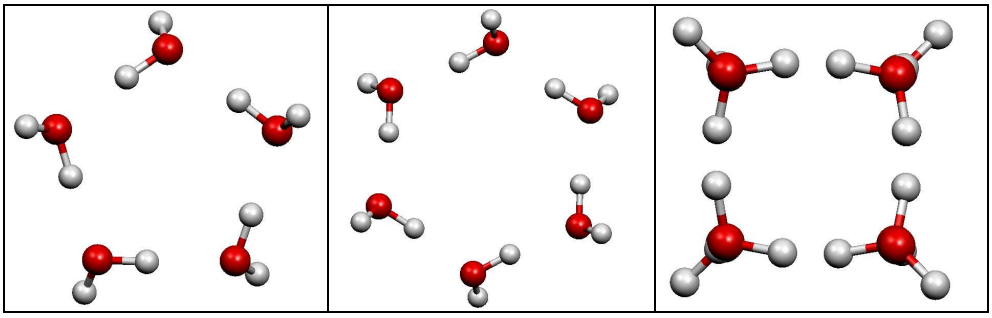

Figure 2. Geometric structures of the TIP5P water pentamer, hexamer, and octamer.

For all clusters with n larger than eight the TIP5P model renders lower bonding energies than TIP4P (table 1). The decamer is a pentagonal prism, composed of the two overlapping pentagonal rings. The TIP5P dodecamer (figure 3) has a less regular structure (two pentagons and two additional molecules in the plane between them), whereas the TIP4P structure consists of two adjacent cubes. It is noteworthy that all our structures with $n \leq 10$ (except for n = 6) are identical with those computed by Maheshwary et al. [4] by first principles (Hartree-Fock and DFT) methods. For larger clusters, their optimizations lead to different configurations which correspond to less stable geometries in our calculations. However, it is known that Hartree-Fock and DFT methods in conjunction with the 6-31g(d) basis set are not very well suited for describing hydrogen bonded systems, so the results of Maheshwary et al. for larger clusters should be regarded with reservation.

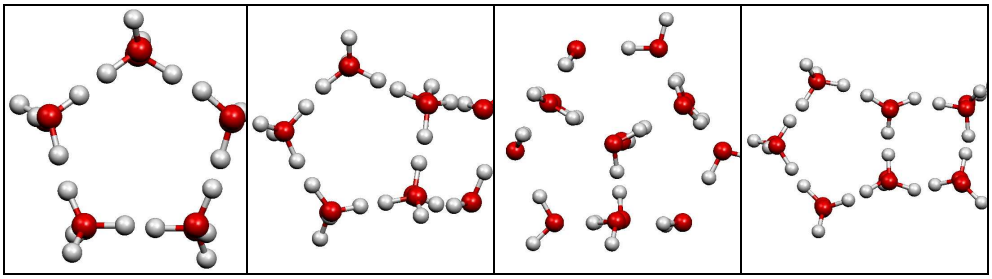

Figure 3 Geometric structures of the TIP5P water clusters of sizes n = 10, 12, 14, and 15.

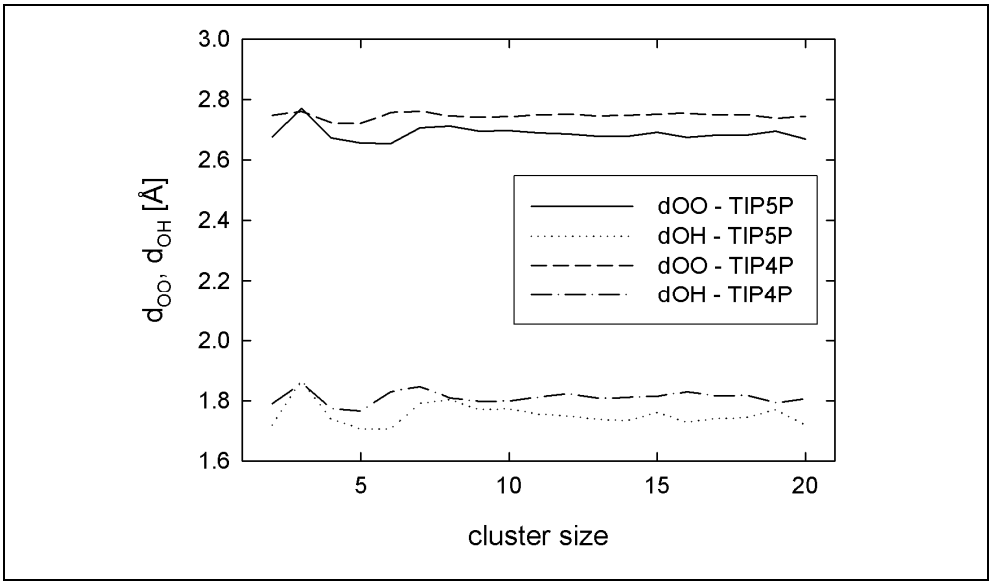

Figure 5. OO and OH bond length dependence of cluster size

For values of n ranging from 14 to 19 our structures seem less symmetric than the ones computed by Wales and Hodges. For n = 15 the cluster consists of a pentagonal prism and a cube, and an extra molecule situated in a plane comprised between the faces of the cube (figure 3). The clusters formed by 16 and 18 molecules are hollow structures composed of rings formed by four, five or six molecules, respectively, while the clusters formed by 17 and 19 molecules do not seem to have a regular structure. The TIP4P structures consist either of pentagonal prisms or cubes. The TIP5P structures are less regular than the TIP4P counterparts probably due to the supplementary interaction site, which seems to make it more difficult to reach the equilibrium configuration.

The TIP5P cluster with n = 20 appears to be less stable than the TIP4P equivalent but we suspect not having reached the global minimum

yet. Our TIP5P cluster has a dodecahedral form, while the TIP4P configuration consists of three edge-sharing pentagonal prisms.

For all *n* values, the TIP5P clusters are more compact than the TIP4P counterparts, with lower values for both the O-O distance and the hydrogen bond length, indicating more stable clusters. For the TIP5P clusters, the average O-O distance has an irregular dependence on *n* with a maximum for *n* = 3, minima for *n* = 4, 5, and 6, while for larger values of *n* the bond length tends to saturate. It is interesting to notice that although the TIP5P clusters are more stable they have a lower density of hydrogen bonds per clusters than for the TIP4P ones.

The hydrogen bond length tends towards a constant value as the cluster size increases for both potential models, but for the TIP5P cluster the dependence has about the same form as for the O-O distance, presenting a clear maximum for *n* = 3 and minima for the symmetric clusters. The bond length dependence we have obtained is consistent with the one obtained by Maheshwary et al through HF and DFT calculations [4]. Indeed, the limiting O-O bond lengths for *n* > 10 are 2.67 Å (TIP5P), 2.74 Å (TIP4P), 2.88 Å (HF), and 2.73 Å (DFT), with our results more consistent with the DFT values. As concerns the O-H bond lengths, they are 1.72 Å (TIP5P), 1.81 Å (TIP4P), 1.99 Å (HF), and 1.79 Å (DFT), showing again the same consistencey with the DFT results.

Conclusions

New minimum energy structures of $(H_2O)_n$ clusters, obtained by a combination of stochastic and deterministic energy minimizations, are presented. The TIP5P site-site model potential employed yields with few exceptions lower ground-state energies for the clusters with $n \leq 20$, and also different geometries for some of them. Regular prismatic and cubic substructures enter the geometries of the lowest energy TIP5P isomers for the most cluster sizes.

REFERENCES

1. M.W. Mahoney and W.L. Jorgensen, J. Chem. Phys. 112, 20 (2000).
2. W.L. Jorgensen, J. Chandrasekhar, J.D. Madura, R.W. Impey, M.L. Klein J. Chem. Phys. 79, 2 (1983).
3. D. J. Wales and M. P. Hodges, Chem. Phys. Lett. 286, 65 (1998).
4. S. Maheshwary, N Patel, N. Sathyamurthy, A. D. Kulkarni, S R. Gadre J. Phys. Chem. A, 105 (2001).

STUDIA UNIVERSITATIS BABEŞ-BOLYAI, PHYSICA, LI, 1, 2006

THE STUDY OF MOLECULAR MOVEMENTS IN BINARY LIQUIDS MIXTURES BY PROTON N.M.R RELAXATION

GHEORGHE CRISTEA[1], VIRGIL IONCU[2]

ABSTRACT. In this paper the proton N.M.R. relaxation phenomenon has been used for studding the rotational and translational molecular movement in the following binary liquids mixture: isopropyl alcohol-CCl_4, n-amyl alcohol-CCl_4 and benzene-CCl_4. All the three liquids, diluted in diamagnetic CCl_4, contain protons and, therefore, excited by an electromagnetic radiofrequency pulse, give an N.M.R. signal which decays as a result of spin-lattice and spin-spin proton relaxation. The experiment consists in determination of T_1 (the spin -lattice relaxation tine) and T_2 (the spin-spin relaxation time) which are tight linked with rotational and translational molecular movements. We argued that in these mixtures only dipole-dipole, intra- and intermolecular, relaxation mechanism is effective. Separating, experimentally, the two dipole-dipole relaxation mechanisms we were able to determine rotational correlation time (τ_R) and translational correlation time (τ_D) of the molecular motion. Knowing these two parameters we determined the rotational diffusion coefficient (D_R) and the translational diffusion coefficient (D) of alcohol and benzene molecules, respectively.

Keywords. Molecular motion, N.M.R. proton relaxation and paramagnetic binary liquid mixtures.

Introduction

The link between molecular motion in liquids and nuclear magnetic relaxation is achieved through the local magnetic field fluctuations. In order to induce relaxation transitions between energetic levels of the spin system the frequency of field fluctuations have to by close to magnetic resonance frequency, by which the spin system is excited. This circumstance allows the experimental study of the intensity and character of molecular motion in liquids by measuring the magnetic relaxation time (rate) of excited nuclear spins of the molecules. The typical molecular motions causing the local magnetic field fluctuations are the rotational and translational diffusion of the molecules (Blombergen *et al*. 1949, Wangsness & Bloch 1953, Kubo & Tomita 1954). The vibrational motion in molecules have to high frequency, compared with radiofrequences used in N.M.R. experiments, to be effective in stimulating the relaxation processes.

[1] Western University “Vasile Goldis” Arad, Blvd. Revolutiei no. 81, Arad 2900, Romania e-mail: gcristea@phys.ubbcluj.ro
[2] "Babes-Bolyai" University, Cluj-Napoca, Str, Kogalniceanu no. 1, Cluj 3400, Romania

In the most general case, there are five relaxation mechanisms effective in stimulating the nuclear magnetic relaxation process. They are the following: 1) dipole-dipole interaction; 2) scalar interaction; 3) electric quadrupole interaction; 4) spin rotational interaction and 5) the chemical shift anisotropy (Carrington & McLachlan 1978, Ludin & Fedin 1986). The separation of their contribution to the measured relaxation rate is an extremely difficult task, in the most general case. This presumes to have a sophisticated experimental technique, permitting measurement of relaxation rates versus radiofrequency or/and temperature (Grűner & Hertz 1972). Because we do not dispose of such facilities spin systems in which two of the relaxation mechanisms vanishes and other two are too weak to be taken into account has been chosed for study. The studied spin systems are: isopropyl alcohol ($CH_3CHOHCH_3$), n-amyl alcohol [$CH_3(CH_2)_3CH_2OH$] and benzene (C_6H_6), all mixed with carbon tetrachloride.

The main parameter which characterizes the molecular motion in liquids is the correlation time τ_c (Debye 1945). The most important mechanisms stimulating the nuclear magnetic relaxation in liquids are intramolecular dipole-dipole interaction and intermolecular dipole-dipole interaction. In the equations expressing the relaxation rate through intramolecular dipole-dipole interaction the correlation time identifies with rotational correlation time (τ_R). In the equations expressing relaxation rate through intermolecular dipole-dipole interaction the correlation time identifies with the translational correlation time (τ_D).

Theoretical Considerations

As we mentioned above, in the spin systems chosen by as for study only the dipole-dipole interaction mechanism of relaxation is effective Vashman & Pronin 1986). Indeed, the electric quadrupolar relaxation mechanism manifests only in spin systems containing nuclear spins I > 1/2. The natural abundance of ^{17}O oxygen's isotope (0,037%), having I = 5/2, is too low to have significant influence on relaxation times. There are some studies on alcohol mixture enriched in ^{17}O (Farrar *et al.* 1999). The scalar interaction is present only in spin systems containing at least two different spins, which is not the case. The chemical shift anisotropy contribution to nuclear relaxation appears only in intense magnetic fields and for nuclei heavier than the proton (McConnel & Holm 1956), hence can by neglected. Finally, we may eliminate also from analyses the spin rotational contribution to nuclear relaxation since it appears only in liquids containing ^{16}F and ^{13}C (1,1%) nuclei (Abragam 1963). Therefore, it remains to concentrate our attention only dipole-dipole mechanism of relaxation.

In turn, the dipole-dipole relaxation has two components: a) the relaxation induced by intramolecular dipole-dipole interaction and b) the relaxation induced by intermolecular dipole-dipole interaction. In the

intramolecular dipole-dipole relaxation the local fluctuations of magnetic field appear as a result of rotational movement of magnetic nuclei within the same molecule. In the intermolecular dipole-dipole relaxation the local fluctuations of magnetic field appear as a result of translational movement of magnetic nuclei in a molecule relative de magnetic nuclei in a neighbor molecule.

The theory of nuclear relaxation processes in liquid state has been elaborated in the 1950's (Blombergen *et al*. 1949, Wangsness & Bloch 1953, Kubo & Tomita 1954) and improve later (Alaxandroff 1975). The spin-lattice ($1/T_1$) and spin-spin ($1/T_2$) relaxation rates, induced by intramolecular dipole-dipole interaction, in systems containing a single type of nuclear spins, like those studied by as, are:

$$\left(\frac{1}{T_1}\right)_{dd}^{int\ ra} = \left(\frac{\mu_0}{4\pi}\right)^2 \frac{2}{5}\hbar^2\gamma_p^4 I(I+1)\left(\frac{\tau_c}{1+\omega_I^2\tau_c^2} + \frac{4\tau_c}{1+4\omega_I^2\tau_c^2}\right)\sum_{i,j>i} R_{ij}^{-6} \tag{1}$$

$$\left(\frac{1}{T_2}\right)_{dd}^{int\ ra} = \left(\frac{\mu_0}{4\pi}\right)^2 \frac{2}{5}\hbar^2\gamma_p^4 I(I+1)\left(\frac{3}{2}\tau_c + \frac{5}{2}\frac{\tau_c}{1+\omega_I^2\tau_c^2} + \frac{\tau_c}{1+4\omega_I^2\tau_c^2}\right)\sum_{i,j<i} d_{ij}^{-1} \tag{2}$$

Here $\hbar = 1.05.10^{-34}\,J.s$ is reduced Planck's constant, $\gamma_p = 2{,}675.10^{-4}\,T^{-1}.s^{-1}$ - proton nuclear gyromagnetic ratio, $\mu_0 = 4\pi.10^{-7}\ N/A^2$ - magnetic permeability of vacuum, τ_c - the correlation time for intramolecular dipole-dipole interaction, R_{ij} - the distance between the two interacting nuclei, $<d_{ij}> \cong 2a_0$ - the smallest average distance between interacting spins belonging to different molecules and ω_I - the magnetic resonance frequency. **Observation:** The factor $(\mu_0/4\pi)^2$ does not appear in original form of Eqs. (1) and (2). We introduced it here in order to express the Eqs. in International System (S. I.) of units (Farar et all. 1999).

When the strong line narrowing condition, ($\omega_I^2\tau_c^2 << 1$), is fulfilled and for nuclei having I = 1/2, both dipole-dipole relaxation rates became equal. In our case $\omega_I^2\tau_c^2 \cong 10^{-5}$ so that:

$$\left(\frac{1}{T_{1,2}}\right)_{dd}^{int\ ra} = \left(\frac{\mu_0}{4\pi}\right)^2 \frac{3}{2}\hbar^2\gamma_p^4\tau_c\sum_{i,j<i} R_{ij}^{-6} \tag{3}$$

In the same conditions, the two relaxation rates induced by intermolecular dipole-dipole interactions are equal and can be written as:

$$\left(\frac{1}{T_{1,2}}\right)_{dd}^{int\ er} = \left(\frac{\mu_0}{4\pi}\right)^2 \frac{\pi\hbar^2\gamma_p^4 N_I\tau_c}{a_0^2}\left(1+\frac{2a_0^2}{5D_s\tau_c}\right)\sum_{i,j}\frac{1}{<d_{ij}>} \tag{4}$$

Here N_l is the sample spin concentration, a_0 - the molecule radius, presumed of spherical shape, D_s - translational diffusion (selfdiffusion) coefficient and d_{ij} the minimum distance betweem closest two different molecules.

Generally, the correlation time τ_c has the following significance:
For the intramolecular dipole-dipole interaction it has three components:

$$\frac{1}{\tau_c} = \frac{1}{\tau_R} + \frac{1}{\tau_S} + \frac{1}{\tau_B} \tag{5}$$

For the intermolecular dipole-dipole interaction it has just two components:

$$\frac{1}{\tau_c} = \frac{1}{\tau_D} + \frac{1}{\tau_S} \tag{6}$$

Here, τ_R denotes the correlation time of rotational motion of the molecules, τ_D - the correlation time of translational motion of the molecules, τ_{RS} - the correlation time of S which do not relaxes and τ_B - the correlation time of the ligand attached to the solvated complex stratum. The following relationships: $\tau_R << \tau_{S.,}\tau_B$ and $\tau_D << \tau_S$ are satisfied in pure and mixed liquids. This means that intramolecular contribution to the experimentally measured relaxation rate $\tau_c = \tau_R$ in Eq. (3). Also, the intermolecular contribution to the experimentally measured relaxation rate $\tau_c = \tau_D$ in Eq. (4) (Powles & Hartland 1960).

Material and Method

As mentioned already, the following mixtures of liquids were studied: the isopropyl alcohol ($CH_3CHOHCH_3$), the n-amyl alcohol [$CH_3(CH_2)_3CH_2OH$] and benzene (C_6H_6), all suspended with carbon tetrachloride (CCl_4). All chemicals were purchased from Merck Company and have had proanalysis degree of purity (>99%).

The experimental measurements of spin-spin (T_2) relaxation time were carried out at room temperature with Aremi-78 N.M.R. apparatus, at radiofrequence of 25 Hz, using the Meiboom-Gill pulse sequences (Meiboom & Gill 1958). In order to diminish the translational diffusion in the sample the spin-echo decay was followed in 178 points, associating to each point four 180^0 pulses. The decay of the spin-echo has been fitted with a single exponential function, by the UC-1 unit, which proved digital display of the relaxation time value.

In order to separate the intramolecular and intermolecular dipole-dipole contributions to the global measured relaxation time the measurements were carried out for five different concentrations of the alcohol and benzene in CCl_4: 1; 0.8; 0.6; 0.4; 0.2; alcohol volume part. The carbon tetrachloride has been choused as diluting because it is a magnetically inert substance.

Results and Discussions

Since, as we demonstrated already, in the studied by as liquid systems, containing hydrogen nuclei, the only effective relaxation mechanism is the dipole-dipole interaction, with its intramolecular and enter-molecular contributions. In these circumstances the experimentally measured relaxation rate can be expressed as (Dupan at al. 1971):

$$\left(\frac{1}{T_{1,2}}\right)_{dd}^{exp\ er} = \left(\frac{1}{T_{1,2}}\right)_{dd}^{int\ ra} + C\left(\frac{1}{T_{1,2}}\right)_{dd}^{int\ er} \quad (7)$$

Here C is the volume part (concentration) of the studied compound in CCl_4. The Eq. (7) is a first grade equation of the type y = b + ax in which the variable x = C, the ordinate b = $(1/T_{1,2})_{dd}^{int\ ra}$, and the slop a = $(1/T_{1.2})_{dd}^{int\ er}$. One may observe that the two contributions are separated in Eq. (7) so they can by individually determined experimentally.

Fig. 1 shows the dependence of relaxation rate *vs*. isopropyl alcohol part (concentration) in the liquid mixture. By extrapolation the graphic toward the low concentration limit, its intersection with ordinate axes gives b = $(1/T_{1,2})_{dd}^{int\ ra}$ and the slop of the line gives a = $(1/T_{1.2})_{dd}^{int\ er}$. The values of these parameters were obtained by fittig measured relaxation rate with a first-degree equation and are specified in Fig.1, together with the fitting standard error.

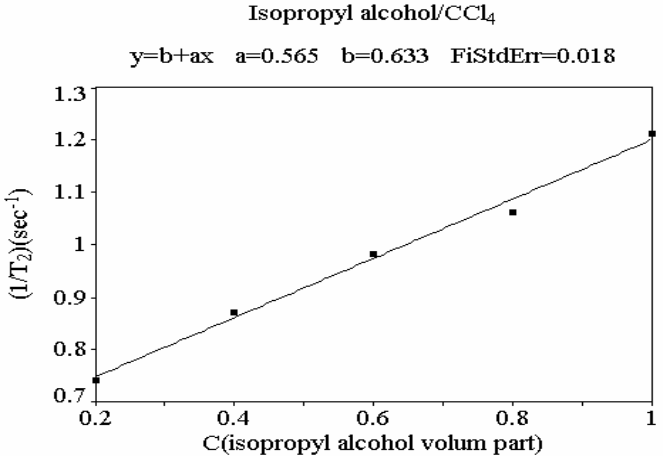

Fig. 1. Concentration dependence of experimentally measured relaxation rate vs. isopropyl alcohol

In a similar way were processed the experimental data for the other two studied compounds. The results are shown in Fig. 2 for the n-amyl alcohol - CCl_4

mixture and in Fig. 3 for benzene - CCl_4 mixture. The values of *a* and *b* parameters can be read on the corresponding graphic.

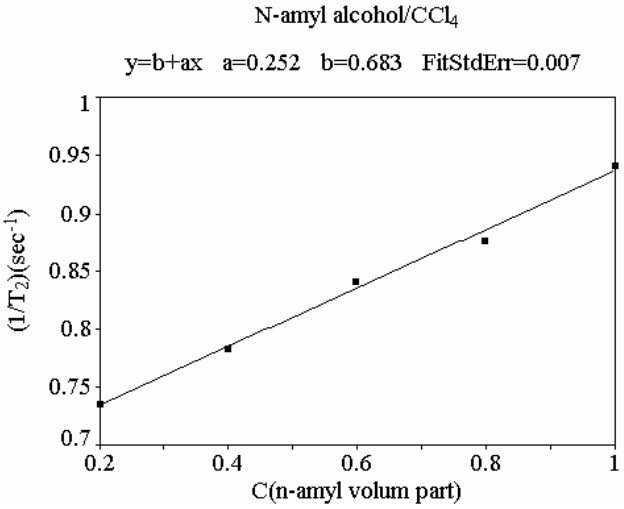

Fig. 2. Concentration dependence of experimentally measured relaxation rate vs. n-amyl alcohol

To proceed farther we have to calculate first the molecular radius (a_0), the spin concentration (N_I) and the sum $\sum_{i,j>i} R_{ij}^{-6}$ for each sample.

Molecular radii were calculated supposing that molecules are spherical and have the closest hexagonal packing. This type packing, characteristic for liquids, has the structure coefficient $\alpha = 0.74$. In this case the molecular radius is $a_0 = (3\alpha M / 4\pi\rho N_A)^{1/3}$.

The spin concetrations has been calculated only for the samples having 1:1 volume ratio, using the usual formula $N_I = \rho N_A N_p / M$. Here M is the molecular mass and ρ the density of the studied compounds; also, N_p is the number of protons in a single molecule and N_A is Avogadro's number.

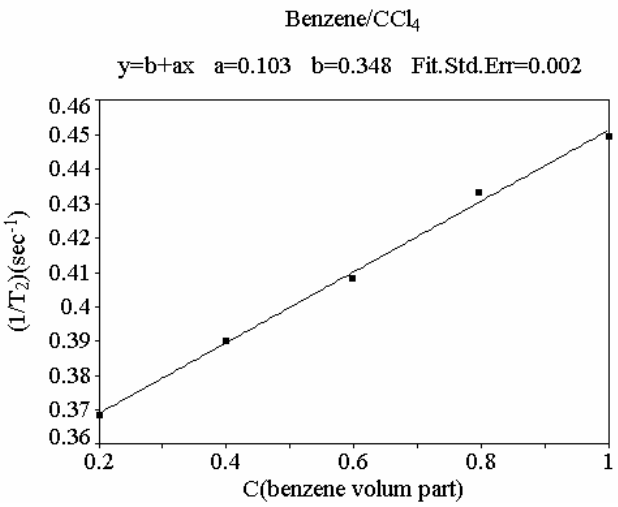

Fig. 3. Concentration dependence of experimentally measured

The sum $\sum_{i,j>i}' R_{ij}^{-b}$ was calculated taking into account the length of chemical bounds and the angles between them (Hell 2002) according with Fig. 4. The structural formulae of the studied compounds are shown in Fig. 4 and the obtained values for these parameters are summarized in Table 1

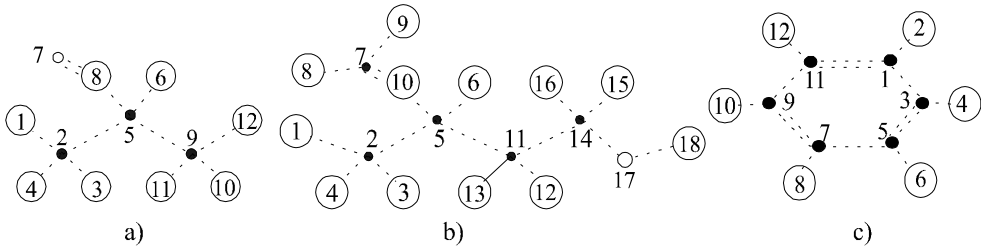

Fig. 4. Structural formulae of compounds: a) isopropyl alcohol; b) n-amyl alcohol: c) benzene

The rotational correlation times τ_R may by calculated by simply replacing the *b* and $\sum_{i,j>i} R_{ij}^{-6}$ values, for each sample, in Eq. (3). Also, the translational correlation times τ_D may by calculated by replacing the values of a, a_0 and $d_{ij} = 2a_0$ in Eq. (4). The value of parameters *a* and *b* obtained experimentally as well as the calculated values for τ_R and τ_D are given in Table 2.

Table. 1.
The value of the calculated parameters

Sample	a_0(Å)	$N_l\ 10^{28}$ (m^{-3})	Suma R_{ij}^{-6} ($Å^{-6}$)
Isopropyl alcohol	6.09	12.6	0.25
n-amyl alcohol	6.82	13.3	0.38
Benzene	6.38	8.14	0.096

Knowing the correlation time for the rotational and the translational molecular motion we have calculated the rotational diffusion coefficient and translational diffusion coefficient of molecules, using the formulae (Vashman & Pronin, 1986): The obtained values are summarized in Table 3.

$$D_R = \frac{1}{6\tau_R} \qquad \text{and} \qquad D_s = \frac{a_0^2}{3\tau_D} \tag{8}$$

The rotational and translational correlation times may by also calculated using the classical formulae obtained by Stokes-Einstein-Debye, supposing that polar and spherical molecules of radius execute Brownion movement (rotational and translational) in a continuum viscous fluid.

Table 2.
Relaxation rates and correlation times experimentally obtained

Sample	$\left(\frac{1}{T_2}\right)_{dd}^{intra}$	$\tau_R.10^{12}$ (s)	$\left(\frac{1}{T_2}\right)_{dd}^{inter}$	$\tau_D.10^{12}$ (s)
i-propyl alcohol	0.640 s^{-1}	2.99	0.565	4.94
n-amyl alcohol	0.383 s^{-1}	1.19	0.251	1.95
Benzene	0.347 s^{-1}	4,28	0.103	2.14

According to Stokes-Einstein-Debye theory (Hill 1954), for the rotational molecular motion:

$$D_R = \frac{kT}{8\pi\eta a_0} \qquad \text{and} \qquad \tau_R = \frac{8\pi\eta a_0^3}{3kT} \tag{9}$$

Here η is the viscosity coefficient of the liquid mixture. Similarly, for the translational molecular movement, the following relationships are thru:

$$D_s = \frac{kT}{6\pi\eta a_0} \quad \text{and} \quad \tau_D = \frac{2\pi\eta a_0^3}{kT} \tag{10}$$

One realizes that the relationships between diffusion coefficient and the correlation time, expressed by Eqs. (8), could by obtained by multiplying the Eqs. (9), respectively by multiplying Eqs. (10). We used these formulae for calculating the viscosity of these liquids. The obtained values are also inserted in Table 3.

Tabelul 3.

The diffusion coefficients and the viscosities

Sample	$D_R.10^{-10}$ (rad^2/s)	$D_s.10^8$ (m^2/s)	$\eta.10^{-3}$(Pa.s)
i-propyl alcohol	5.53	2.50	1.83
n-amyl alcohol	14.0	7.95	0.77
Benzene	3.9	6.34	1.15

It should be mentioned, however, that the agreement between the correlation times measured by nuclear magnetic relaxation experiments and those theoretically calculated using macroscopic properties of liquids is quite poor. This is why there is a strong tendency, in the last time, to consider the correlation times measured by nuclear magnetic relaxation as independent parameters, characterizing the molecular motion in liquid and liquid mixtures. For this reason, it has little sense to compare the correlation times values obtained by nuclear magnetic relaxation measurements with those obtained from measuring the viscosity, diffusion coefficients or light scattering.

However, if we assimilate the correlation times measured by nuclear magnetic relaxation method with those obtained from viscosity or diffusion coefficient measurements it is possible to determine other important parameters describing molecular motion in liquid mixture.

Conclusions

The nuclear magnetic relaxation measurement technique is an extremely powerful method for studying molecular motion in liquids. In the simplest case only the correlation times can be measured but when one may perform measurements as function of temperature or/and frequency and corroborated with other means of study it provides a large aria of possibilities.

In our experimental conditions we were able to determine, by nuclear magnetic proton relaxation measurements, the rotational and translational correlation times, the corresponding diffusion coefficients and viscosity coefficients of three liquid mixture, at room temperature. The obtained results are of the same order of magnitude as those obtained by other researchers on similar samples. The observed differences could be due to fact that the studied molecules are not spherical or/and molecular packing is not a closest hexagonal one, as we supposed to be.

BIBLIOGAPHY

1. Abragam A. Iadernâi magnetism, Izd. Iostranoi Literaturâ, 1963, Moscva
2. Alexandrov I., V., Teoria iadernovo magnitnovo rezenansa, 1964, Izd, "Nauka" Moscva
3. Blombergen N., Purcell E., N., Pound R., V., 1949, Phys. Rev. 73, pg. 679
4. Carrington A. & McLachlan, 1978, Chapman &Holl, New-York
5. Debye p., Polar Molecules, 1945, Dover Publications Inc., New-York
6. Dupan J., C., Brifnet A., Delma J., J. Chem. Phys. 1971, 54, pg. 2648
7. Farrar T C., Wendt M. A., Zeidler M. D., 1999, J. Chem. Soc., Vol, 10, No. 4 321.
8. Grűner M., Hertz H., G., Advances Mol. Relax. Procesess, 1972, 3, pg. 75
9. Hill N., E., Proc. Phys. Soc., London, 1954, 67B, pg. 149
10. Hell H., 2002, http://www.bbc.co.uk/dna/h2g2/A791246
11. Kubo R., Tomita K., J. Phys., Soc. Japan, 1954, 9, pg. 888
12. Lösche A., Kerninduction, 1957,Veb Deutscher Verlag der Wissenschaften, Berlin.
13. Ludin A., G., Fedin E., J., Spectroscopia RMN, 1986
14. McConnell H., M., Holm C., H., J. Chem. Phys. 1956, 25, pg. 1289
15. Meiboom S., Gill D., Rev. Scient. Instrum. 1958, 29, pg. 688
16. Powles J., G., Harland A., 1960, Proc. Phys. Soc. 75, pg. 617
17. Thomas C., J. Braz. Chem. Soc., 1999, 10(4), pg. 321
18. Vashman A., A., Pronin I., S., Iadernaia magnitnaia relaxationaia spectroscopia, 1986, Energoatomizdat. Moscva
19. Wangsness R., K., Bloch F., Phys. Rev., 1953, 89, pg. 728

STUDIA UNIVERSITATIS BABEŞ-BOLYAI, PHYSICA, LI, 1, 2006

STRUCTURAL AND DIELECTRIC STUDIES OF FERROELECTRIC RELAXOR LEAD INDIUM NIOBATE COMPOUND

I.ARDELEAN[a] ,I.BARBUR[a] ,V.CIOBOTA[a] ,G.BORODI[b] ,V.TIMAR[a]

ABSTRACT. X-ray diffraction and dielectric measurements were performed on polycrystalline $Pb_2In\ NbO_6$ (PIN). The X-ray measurements indicate formation of single-phase perovskite structure with partial of In and Nb ions ordering. The existence of two ε(T) maximum indicate coexistence of completely ordered and disordered regions in PIN compound.

Introduction

Based on X-rays and transmission electron microscopy(TEM) studies [1], the complex lead perovskite compounds $Pb(B'B'')O_3$ and their solid solutions can be divided into three subgroups depending on B-site ordering of the cations: random occupation or disordered, nanoscale or short coherent long-range order and long coherent long range order of B-site cations.

According to dielectric an optical properties, these compounds are assigned to the normal ferroelectrics (antiferroelectrics) or relaxor ferroelectrics. The transition behaviour in normal ferroelectrics shows a 1^{st} or 2^{nd} order phase transition. The relaxor ferroelectrics are characterized by a diffuse and dispersive phase transition.

Within the complex perovskites $Pb(B'_xB''_{1-x})O_3$ (x=1/2) family, many of the compounds have shown long-range order (LRO) of B cations [2]. If the B cations are randomly occupying the lattice there is no superstructure and the ordinary perovskite cell describes the compound.

Variation in the degree of the LRO is brought by annealing at high temperature and the subsequent quenching is registered by its effect on dielectric characteristics in the Curie point region. Therefore, the temperature of the ferroelectric phase transition T_C proved to be dependent on the degree of the compositional ordering. This enables one to use the temperature of ferroelectric transition as a measure of disorder.

In this contribution we present structural and dielectric studies on Pb_2InNbO_6 (PIN) polycrystalline samples. PIN belongs to trioxides $Pb^{2+}B^{3+}B^{5+}O_6$ with perovskite-type structure which form a large group of compounds possessing either ferroelectric (FE) or antiferroelectric (AFE)

[a] Faculty of Physics, Babes-Bolyai University,400084, Cluj-Napoca, Romania
[b] National Institute for Research and Development of Isotopic and Molecular Technologies,400293, Cluj-Napoca, Romania

diffuse and dispersive phase transition [2]. Reports on phase transition in PIN are somewhat contradictory. Kupriyanov and Fesenko [3] found the first the transition at 90°C through the observation of a peak in dielectric constant measured on ceramic compound of PIN. It was demonstrated that it is possible to increase the degree of ordering of the In and Nb ions [4,5] with the corresponding increase in transition temperature from 60°C (disordered state) to 190°C (ordered state).

In order to obtain new aspects regarding sinthesis and phase transition in PIN, we report structural and dielectric measurements on ceramic samples of this compound.

Experimental

The polycrystalline samples of PIN were prepared by reacting corresponding proportions of PbO, In_2O_3 and Nb_2O_5 species using high-purity grade chemicals. The mixture was calcinated at 700°C for 20 hours and sintered at 900°C for 2 hours. All the samples were prepared in air atmosphere and at normal pressure.

The X-ray diffraction measurements were performed at a DRON-2-type diffractometer using CrK_α radiation.

The dielectric constant and loss tangent were measured in the temperature range 300-600 K at 1 kHz using a digital automatic bridge KEITHLEY 3300 LCZ.

Results and Discussion

The shape of lines of X-ray diffraction patterns (which are different from those of components) suggested the formation of a single-phase compound (Fig.1). The diffraction patterns confirm an orthorombic structure having the cell parameters: a=10.672Å; b=15.103Å; c=4.182Å; $\alpha=\beta=\gamma=90°$. These parameters correspond to a doubled cell as a result of In and Nb ions ordering. The doubled unit cell gives rise to a superlattice reflections. The most intense diffraction lines in figure 1 are indexed as single perovskite structure, and lines of lower intensity as suprastructure lines.

The examination of X-ray measurements of PIN compound at room temperature shows that, as with all perovskite crystal that undergo dispersive phase transition, they are twinned. It is possible that some of lines of lower intensity to belong to unwanted pyrochlore phase which, unfortunately, was not completely eliminated.

The temperature dependence of the relative dielectric constant for PIN compound is shown in figure2.The presence of two ε(T) maximum are observed. A small peak at 87°C is responsible for disordered state and a greater peak at 208 °C corresponding to ordered state of In and Nb ions in PIN.

The anomalies in lost tangent are observed at the same temperatures (Fig.3).

As it has been shown[5], the temperature dependence of dielectric constant shows how the degree of In and Nb ions order influence the transition behaviour. The disordered sample displays a very brood transition indicating a brood gaussian distribution of micro-domain regions(called “Kanzig” regions) transition temperatures.

In our ceramic compound of PIN, coexistence of completely ordered and disordered regions causes two ε(T) anomalies indicating the presence of the intermediate stage of ordering process.

Conclusions

The Pb_2InNbO_6 polycrystalline samples were prepared by usual ceramic method at normal pressure and air atmosphere. The X-ray diffraction measurements indicate the formation of single-phase compound.

From the temperature dependence of relative dielectric constant and loss tangent we have observed two anomalies at 87°C and 208°C. This fact suggests an intermediate stages of the ordering process in PIN.

Figure Captions

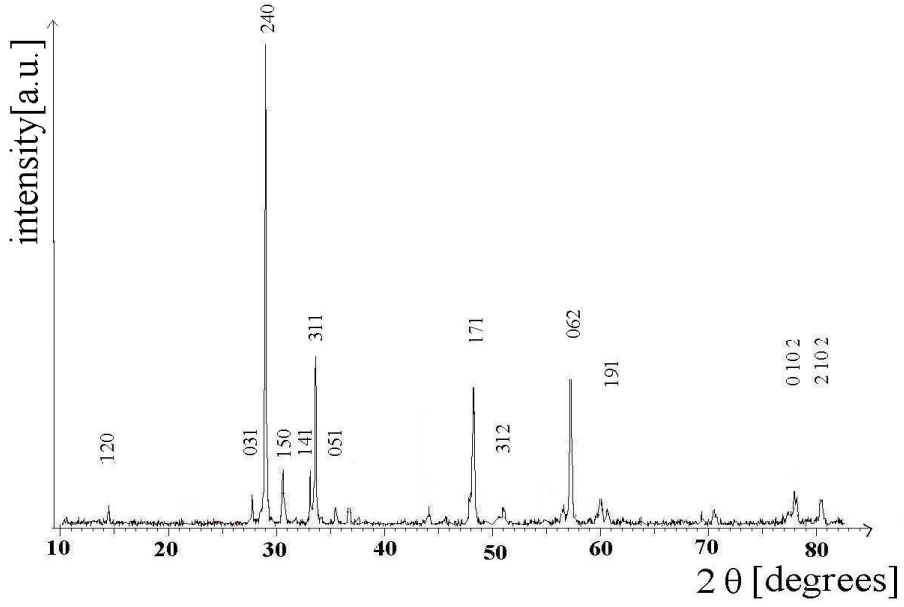

Fig.1. The X-ray diffraction patterns for PIN compound

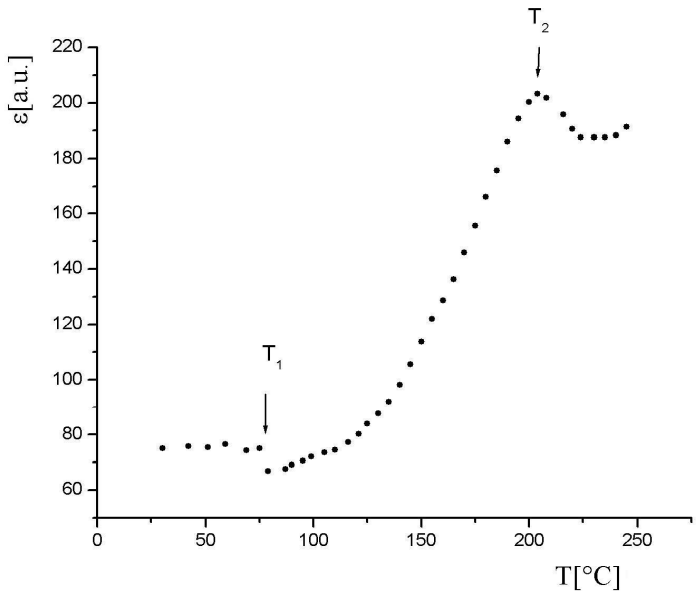

Fig.2. Temperature dependence of the relative dielectric constant (ε) for PIN compound

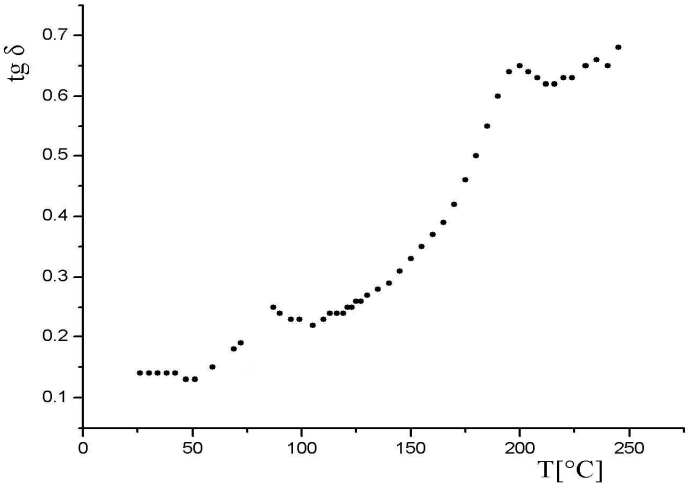

Fig.3. Temperature dependence of the loss tangent (tgδ) for PIN compound

REFERENCES

1. C.A.Randall and A.S.Bhalla, Jpn.J.Appl.Phys., 29, 327(1990)
2. F.S.Galasso, Perovskites and High-T_C Superconductors, Gordon and Breach Sci.Pub., London,1990
3. M.F.Kupriyanov and E.G.Fesenko, Sov. Phys.-Crystallogr. 10, 189(1965)
4. A.A.Bokov, I.P.Rayevskii, V.G.Smotrakov and O.I.Prokopalo, Phys.Stat.Sol.(a) 93, 411(1986)
5. P.Goves, J.Phys.C: Solid State Phys. 19,111(1986)

STUDIA UNIVERSITATIS BABEŞ-BOLYAI, PHYSICA, LI, 1, 2006

EFFECT OF YTTRIUM ADDITION ON THE LOCAL ORDER IN BISMUTH-BORATE GLASSES DOPED WITH GADOLINIUM

S. SIMON[1*], D. ENIU[2]

ABSTRACT. Glass samples of $xY_2O_3(100-x)[yB_2O_3 \cdot Bi_2O_3]$ systems ($0 \le x \le 30$, $y = 1, 3$) were prepared by splat-quenching technique. The effect of yttrium addition on the local order in glasses was investigated by electron paramagnetic resonance of Gd^{3+} ions doped in samples. The results indicate that Gd^{3+} ions may occupy both yttrium and bismuth sites in the investigated glass samples, what further shows that yttrium can be disposed on bismuth sites. By increasing the yttrium content in the two bismuth borate glass matrices the distribution of Gd^{3+} ions on sites of different crystal field strength is reversed.

Introduction

Bismuthate glasses are interesting because their properties are exploited in applications such as, wave-guides in nonlinear optics, scintillation detectors in high-energy physics, excellent IR transmission and high polarisability [1-4]. The optical non-linear properties of B_2O_3-Bi_2O_3 glass systems can be influenced by addition of strontium [5]. Considering the proximate element after strontium, yttrium, that has a relative large cationic radius,1.04 Å, we investigated the changes induced by yttrium oxide in the local order of bismuth borate glass matrices $3B_2O_3 \cdot Bi_2O_3$ and $B_2O_3 \cdot Bi_2O_3$, particularly on the bismuth sites, having in view that the nonlinear optical properties are firstly related to the heavy metal oxide.

The local structure changes induced by yttrium oxide addition up to 30 mol % in the two bismuth borate glass matrices were investigated by Gd^{3+} electron paramagnetic resonance (EPR).

Experimental

Samples belonging to $xY_2O_3(100-x)[yB_2O_3 \cdot Bi_2O_3]$ glass systems, where $0 \le x \le 30$ mol % and $y = 1$ and 3, were doped with 0.5 mol % Gd_2O_3 in order to use Gd^{3+} EPR centers for investigation of structural changes in their vicinity. The glass samples under investigation were prepared by mixing appropriate amounts of H_3BO_3, $Bi_2O_2CO_3$, Y_2O_3 and Gd_2O_3, all analar (analytical reagent) grade chemicals. A homogeneous mixture of powders was prepared and fired in sintercorundum crucibles at 1300 ºC for 30 min in an automatically temperature controlled furnace. The glass samples were

[1] Babes-Bolyai University, Faculty of Physics, 400084 Cluj-Napoca, Romania
* Corresponding author: simons@phys.ubbcluj.ro
[2] University of Medicine and Pharmacy, Faculty of Pharmacy, 400010 Cluj-Napoca, Romania

prepared by splat-cooling technique, by quenching and pressing the melt between steel plates at room temperature. With respect to samples colours one remarks that the glass matrix $3B_2O_3 \cdot Bi_2O_3$ (x = 0) is dark brown-reddish while the glass matrix $B_2O_3 \cdot Bi_2O_3$ is yellowish. By adding yttrium to 3:1 matrix the glasses with low Y_2O_3 content ($x \leq 10$) become brighter and further, for high Y_2O_3 content ($20 \leq x \leq 30$) the samples become yellowish. The glasses formed with $B_2O_3 \cdot Bi_2O_3$ matrix are yellowish for low Y_2O_3 content ($0 \leq x \leq 10$) and become brown-reddish for high Y_2O_3 content ($20 \leq x \leq 30$).

The glass state of the as-quenched samples was attested by X-ray diffraction analysis. Electron paramagnetic resonance spectra were recorded on powder samples at room temperature in X band on an ADANI spectrometer. DPPH with a g value of 2.0036 was used as a standard field marker.

Results and Discussion

The X-ray diffractograms of all the samples consist of a large structureless line and confirms the vitreous state of the samples.

Taking into account that ionic radius of Gd^{3+} (1.08 Å) is a bit higher than of Y^{3+} (1.04 Å), but smaller than Bi^{3+} ionic radius (1.17 Å) it is expected that gadolinium ions are most probably disposed in sites corresponding to bismuth without to exclude the possibility to occupy also yttrium sites. The spectra of Gd^{3+} ions can reflect if their surroundings, and by extension the surrounding off bismuth ions, are distorted by yttrium addition.

The Gd^{3+} EPR spectra of the samples formed in the two systems with different lower Y_2O_3 content are shown in Figures 1-5. For all compositions are recorded resonance signals around g ≈ 2.0, 2.8, 4.3, 4.8 and 5.9. The Gd^{3+} EPR spectra are the superposition of the well known U type spectrum [6-8], with lines at g ≈ 5.9, 2.85, and 2.0 and of a weak resonance line at g ≈ 4.8, that is unusual in X band for the vitreous sample [9]. The signal with g ≈ 4.3 is assigned to Fe^{3+} impurities.

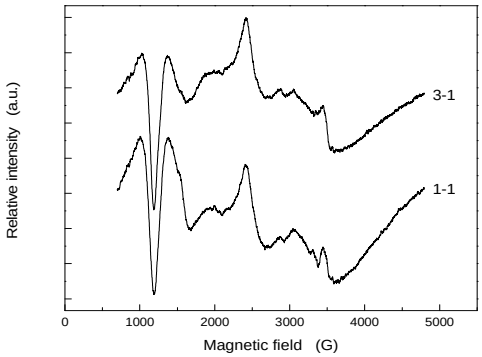

Fig. 1. Gd^{3+} EPR spectra recorded from $3B_2O_3 \cdot Bi_2O_3$ and $B_2O_3 \cdot Bi_2O_3$ glass matrices.

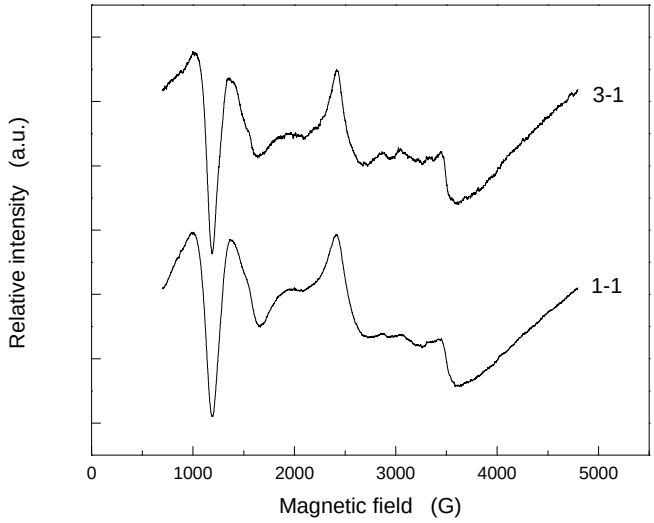

Fig. 2. Gd^{3+} EPR spectra recorded from glasses with 5 mol % Y_2O_3.

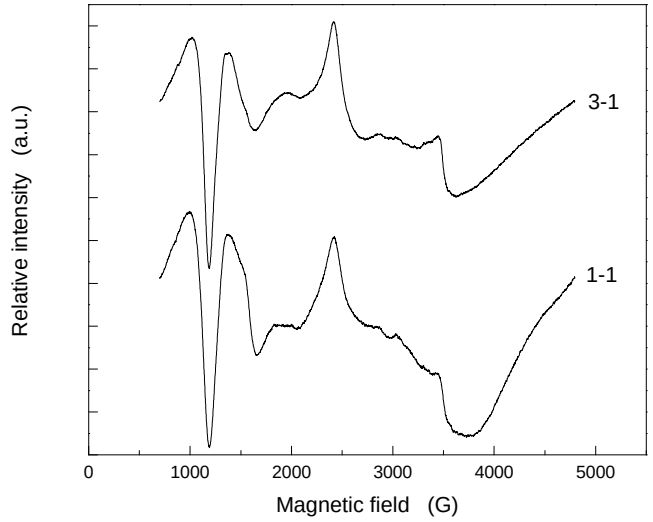

Fig. 3. Gd^{3+} EPR spectra recorded from glasses with 10 mol % Y_2O_3.

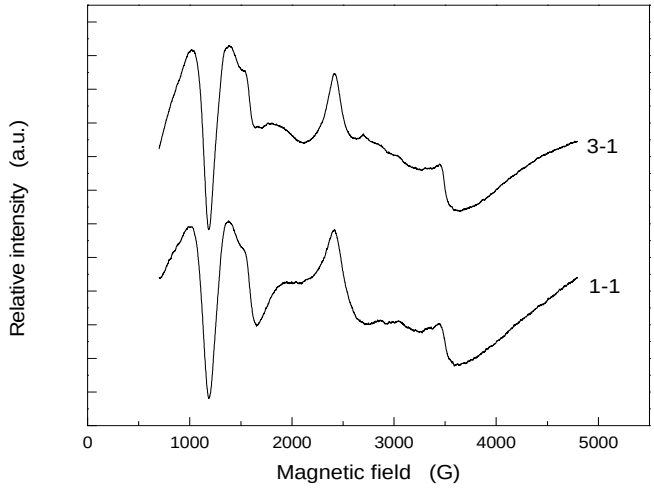

Fig. 4. Gd^{3+} EPR spectra recorded from glasses with 20 mol % Y_2O_3.

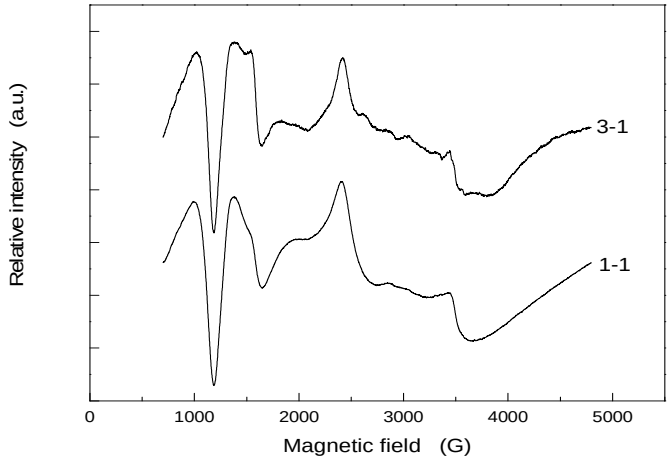

Fig. 5. Gd^{3+} EPR spectra recorded from glasses with 30 mol % Y_2O_3.

The energy levels of these ions in an external magnetic field $\vec{B}$ are described, in a first approximation, by the spin Hamiltonian [6]:

$$\mathcal{H} = g_o \beta \vec{B} \vec{S} + D\left[S_z^2 - \frac{1}{3}S(S+1)\right] + E\left(S_x^2 - S_y^2\right)$$

where the first term is the Zeeman term and the following second order terms describe the crystal field effects, D and E are the axial and rhombic constants of the energy level splitting in zero magnetic field, respectively. Although, in particular for Gd^{3+}, higher order terms can, in general, not be neglected, Gd^{3+} EPR spectra in glasses are well described by this Hamiltonian. The lines at $g \approx 2$ are assigned to paramagnetic ions in sites characterized by relatively weak crystalline fields, for which Zeeman term dominates. The lines with $g > 2$ are attributed to paramagnetic ions in sites of relatively strong crystal field, where the crystal field terms are comparable or larger than the Zeeman term [7].

The well known fact that the line widths of EPR spectra of glass samples with low paramagnetic ions concentration are broader than those of crystalline samples reflects much larger inhomogeneities in the local structure of glasses.

The U type Gd^{3+}-EPR spectrum is characteristic for Gd^{3+} ions in structurally disordered systems [6]. The lines from U spectrum with $g \approx 5.9$, 2.8 and 2.0 are assigned to Gd^{3+} ions in sites with intermediate crystal fields having coordination numbers higher than 6, while the $g \approx 4.8$ line is characteristic for Gd^{3+} ions in sites of strong crystal fields having a lower coordination number [10]. Such species with unsaturated coordination usually occur only at the surface of oxide systems and they are particularly an important presence in porous materials [7, 11]. Their large presence in the vitreous $xGd_2O_3(100\text{-}x)[4Bi_2O_3 \cdot PbO]$ system proves that the glass matrix $[4Bi_2O_3 \cdot PbO]$ is extremely stiff and imposes to part of the Gd^{3+} ions a coordination uncommon for these ions in vitreous oxide matrices [9].

The linewidth, amplitude and intensity of the main resonance lines are summarised in Tables 1 and 2. The intensity was computed as product of amplitude and linewidth square. One remarks that in the samples without yttrium the linewidth of all resonance signals is sensible narrower then in yttrium containing samples and, in general, it increases with Y_2O_3 content. On the other hand, considering the line intensity proportional to the number of resonance centers giving rise to a certain resonance line, it was appreciated that the doped gadolinium ions are preferentially disposed in sites of intermediate crystal field having coordination numbers higher than 6. By introducing Y_2O_3 into B_2O_3-Bi_2O_3 matrices the changes in the distribution of Gd^{3+} on different sites are not univocal. This result is due most likely to the possibility of Gd^{3+}ions to occupy also Bi^{3+} sites and this assumption is supported by shape and parameters of EPR spectra recorded from samples without yttrium of both systems.

The resonance lines for samples with higher bismuth content (Table 2) are narrower than the corresponding ones for the glass samples with lower bismuth content (Table 1) and similar yttrium concentration, denoting a diminished structural disorder degree by decreasing the B_2O_3 to Bi_2O_3 ratio from 3:1 to 1:1.

Table 1.
Linewidth, amplitude and intensity of the main resonance lines recorded around g ≈ 2.0, 2.8 and 5.9 from $xY_2O_3(100-x)[3B_2O_3 \cdot Bi_2O_3]$ glasses.

x (mol%)	ΔB (G)			Amplitude (a.u.)			Intensity (a.u.)			Site distribution (%)		
	g			*g*			*g*			*g*		
	5.9	*2.8*	*2.0*	*5.9*	*2.8*	*2.0*	*5.9*	*2.8*	*2.0*	*5.9*	*2.8*	*2.0*
0	157	227	102	13.42	6.93	3.89	3.31	3.31	0.40	47	47	6
5	167	244	108	6.36	3.09	1.58	1.77	1.84	0.18	47	48	5
10	173	250	107	12.83	6.72	3.49	3.84	4.17	0.73	44	48	8
20	184	256	105	6.6	2.34	0.657	2.22	1.51	0.05	58	40	2
30	189	264	107	10.8	3.88	1.66	3.85	2.70	0.17	57	40	3

Table 2.
Linewidth, amplitude and intensity of the main resonance lines recorded around g ≈ 2.0, 2.8 and 5.9 from $xY_2O_3(100-x)[B_2O_3 \cdot Bi_2O_3]$ glasses.

x (mol%)	ΔB (G)			Amplitude (a.u.)			Intensity (a.u.)			Site distribution (%)		
	g			*g*			*g*			*g*		
	5.9	*2.8*	*2.0*	*5.9*	*2.8*	*2.0*	*5.9*	*2.8*	*2.0*	*5.9*	*2.8*	*2.0*
0	178	240	119	8.75	4.76	1.83	2.77	2.74	0.25	48	47.6	4.4
5	189	270	139	12.13	7.09	4.79	4.33	5.19	0.92	41.5	49.6	8.9
10	193	280	155	10.01	6.54	3.78	3.73	5.13	0.91	38.2	52.5	9.3
20	195	300	166	10.52	6.17	2.74	4.06	5.55	0.76	39.2	53.5	7.3
30	197	310	206	17.85	10.5	5.12	6.72	10.09	2.17	35.5	53	11.5

The distribution of gadolinium ions on sites of different crystal field strength in $3B_2O_3 \cdot Bi_2O_3$ glass matrix is comparable as yttrium oxide is added up to 10 mol %, but for x ≥ 20 mol % the gadolinium ions are preponderantly disposed in sites with stronger crystal field giving rise to the resonance signal at g ≈ 5.9. In contrast, in the samples formed with $B_2O_3 \cdot Bi_2O_3$ glass matrix by addition of yttrium oxide the gadolinium ions preferentially occupy the sites with lower crystal field strength that are related to the resonance lines with low g values.

Conclusions

The composition dependence of Gd^3 EPR parameters of the investigated glass samples points out that in the investigated glass samples Gd^{3+}ions mainly occupy bismuth sites. The structural disorder degree is diminished in the glass system with higher bismuth content, but the progressive addition of yttrium has an opposite effect on the local order. By addition of yttrium oxide into $3B_2O_3 \cdot Bi_2O_3$ glass matrix increases the number of

gadolinium ions disposed on sites of stronger crystal field strength while in $B_2O_3 \cdot Bi_2O_3$ glass matrix is noticed the tendency to increase the number of gadolinium ions in sites of lower crystal field strength.

Acknowledgement

This research was partially supported by Romanian National University Research Council.

REFERENCES

1. G. Murugan, K. B. R. Varma, J. Non-Cryst. Solids, 279 (1),p. 1—13 (2001)
2. I.Ardelean, Gh.Ilonca, V.Simon, O.Cozar, V.Ioncu, S.Filip, Solid State Commun. 98, 651 (1996)
3. S. Hazra, A. Ghosh, Phys. Rev, B 56, 13 (1997)
4. C. Stehle, C. Vira, D. Hogan, S. Feller, M. Affatigato, Phys. Chem. Glasses, 39, 2, 836 (1998)
5. G. S. Murugan, G. N. Subbanna, K. B. R. Varma, Ferroelectr. Lett., 26, 1 (1999)
6. D.L. Griscom, J. Non-Cryst. Solids, 67, 81 (1984)
7. L.E. Iton, C.M. Brodbeck, S.L. Suib and G.D. Stucky, J. Chem. Phys., 79, 1185 (1983)
8. R. P. Sreekanth Chakradhar, K. P. Ramesh, J L. Rao, J. Ramakrishna, Modern Physics Letters B, 18(2 & 3):pp.83-97 (2004)
9. S. Simon, R. Pop, V. Simon, M. Coldea, J. Non-Cryst. Solids, 331, 1 (2003)
10. C. Legein, J.Y. Buzaré, G. Silly and C. Jacoboni, J. Phys.: Cond. Matter. 1996, **8**, 4339
11. S. Simon, Mod. Phys. Lett. B, 12&13, 375 (2001)

STUDIA UNIVERSITATIS BABEŞ-BOLYAI, PHYSICA, LI, 1, 2006

DTA INVESTIGATION OF Fe_2O_3-Ca(Ba,Sr)O-B_2O_3 GLASSES

P. RIEDL, E. TATARU, V. SIMON*

ABSTRACT. Glass stability of Fe_2O_3-MO-B_2O_3 systems (M = alkaline earth element) established from differential thermal analysis and the structural role of iron oxide in the investigated glasses are reported. The results suggest structural changes characteristic for the transition from short range to intermediate range order as the cationic field strength of the alkaline earths increases. In contrast, the iron addition has an opposite effect and determines a higher glass stability of these systems.

Introduction

The preparation of the magnetic glass ceramics widely follows the route of the well-known glass crystallization method [1-3] for precipitation of ferrite powders in a quenched melt. The crystallization of glasses after special heat treatment [4] presents wide possibilities to modify the properties and to create new materials for various applications. The preparation of glass–crystalline materials with participation of ferrite phases is of permanent scientific and practical interest [5–15]. These systems are also candidates in obtaining ferrimagnetic microspheres useful as thermoseeds for hyperthermia of cancers because they can heat cancers locally by hysteresis loss of the ferrimagnetic materials under an alternating magnetic field [16].

The preparation of glasses in the MO-Fe_2O_3-B_2O_3 system (M = alkaline earth element: Ca, Sr or Ba) is described and the results concerning the glass stability obtained by differential thermal analysis are presented in this paper.

Experimental

The compositional range of the investigated ternary systems $xFe_2O_3(100\text{-}x)[37B_2O_3{\cdot}63CaO]$, $xFe_2O_3(100\text{-}x)[37B_2O_3{\cdot}63SrO]$ and $xFe_2O_3(100\text{-}x)[42B_2O_3{\cdot}58BaO]$, with x up to 40 mol %, was chosen according to eutectic composition known from the phase diagrams of CaO-B_2O_3, SrO-B_2O_3 and BaO-B_2O_3 binary glasses [17-19].The glass samples were prepared by mixing corresponding amounts of B_2O_3, Fe_2O_3, and $CaCO_3$, $SrCO_3$ or $BaNO_3$.The batches containing calcium or strontium oxide were melted at 1300^{o}C, while that containing barium oxide were melted at 1100^{o}C. The melts were supercooled at room temperature by two plates quenching technique.

* Babes-Bolyai University, Faculty of Physics

X-ray diffraction analysis was carried out on a DRON diffractometer and thermal differential analysis curves were recorded on a MOM type derivatograph at a heating rate of 10^{o}C/min.

Results and discussion

The X-ray diffraction patterns recorded from as prepared samples consist of a large line typical for vitreous systems without lines denoting the presence of any crystalline phase.

For all samples the thermogravimetric and differential thermogravimetric curves do not evidence any weight loss up to 1000^{o}C. The DTA curves of the three glass matrices (Fig. 1) depend on the alkaline earth oxide playing glass network modifier role. Ionic radius, ionic field strength, single bond strength with oxygen and electronegativity of the cations entering in the investigated glasses [20] (Table 1) can explain the observed differences. The range between glass transition temperature, T_g, and the temperature of the first exothermic crystallisation peak, T_{c1}, characterise the glass stability against crystallisation, $S = T_{c1} - T_g$ [21]. The other maxima corresponding to exothermic events, if exist, are assigned either to structural arrangement changes of the crystalline phases previously developed, i.e. to reconstructive reactions inside the existing crystalline phases [22, 23] or to crystallisation of new phases from the vitreous host glass. The lack of endothermal events in the DTA curve denotes the structural stability, at least up to 1000^{o}C, of the crystalline phases grown in these glass matrices.

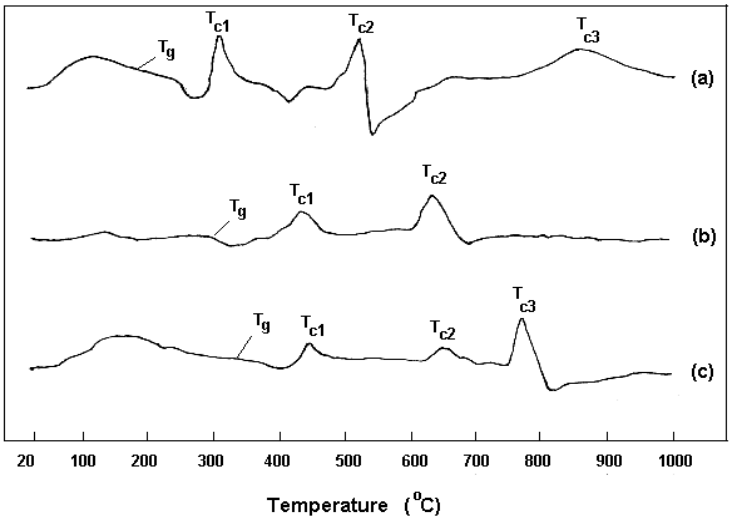

Fig. 1. DTA curves for (a) $42B_2O_3 \cdot 58BaO$, (b) $37B_2O_3 \cdot 63SrO$ and (c) $37B_2O_3 \cdot 63CaO$ samples.

Table 1.
Ionic radius, field strength, electronegativity and single bond strength for the cations entering the investigated glasses.

Cation	Ionic radius (Å)	Cationic field strength ($Å^{-2}$)	Electronegativity (Pauling units)	B-O strength (kJ/mol)
B^{3+}	0.25	48	2.04	808.8 ±20.9
Ba^{2+}	1.49	0.90	0.89	561.9 ±13.4
Sr^{2+}	1.32	1.15	0.95	425.5 ±16.7
Ca^{2+}	1.14	1.54	1.00	402.1 ±16.7
Fe^{3+}	0.69	6.30	1.83	390.4 ±17.2

Boric oxide forms glasses readily all by itself. The properties of borate glasses are strongly tied to strength of the B-O bonds (Table 1). Vitreous B_2O_3 has an unusual intermediate range structure, wherein linked triangles form planar rings. The boroxol rings are very well defined structural unit and they are unusual because this does not occur in crystalline B_2O_3 polymorphs. Probably due to these rings B_2O_3 glass is *very* difficult to crystallize. In alkali borate glasses nonbridging oxygens and tetrahedral boron formation occur. In alkaline earth borate glasses the network is considered [24] to be composed of borate arrangements containing charged BO_{b4}^- tetrahedra and $BO_{b2}O^-$ triangles as well as neutral BO_{b3} units. O_b denotes bridging oxygens, i.e. oxygen atoms bonded to two structural units. The fraction of four coordinated boron atoms increases with increasing metal ion size (Ca, Sr and Ba) The glass transition temperature in glass series is found to scale approximatively linearly the cationic field strength (Fig. 3), which is in agreement with results reported for other alkaline earth borate glasses [24].

The addition of Fe_2O_3 to the alkaline earth borate matrices has a pronounced effect on the increase of glass stability. In Figure 2 are displayed the DTA runs from iron containing glass samples. The crystallisation process is clearly observed only for CaO-B_2O_3 glass matrix, but also in this case the glass stability, S, is considerably increased (290^oC) with respect to the glass matrix (115 ^oC). The data summarised in Table 2 show that the glass stability effect of the transition metal cations is completely different of that observed for alkaline earth cations and can support the assumption that iron ions may play also glass network former role.

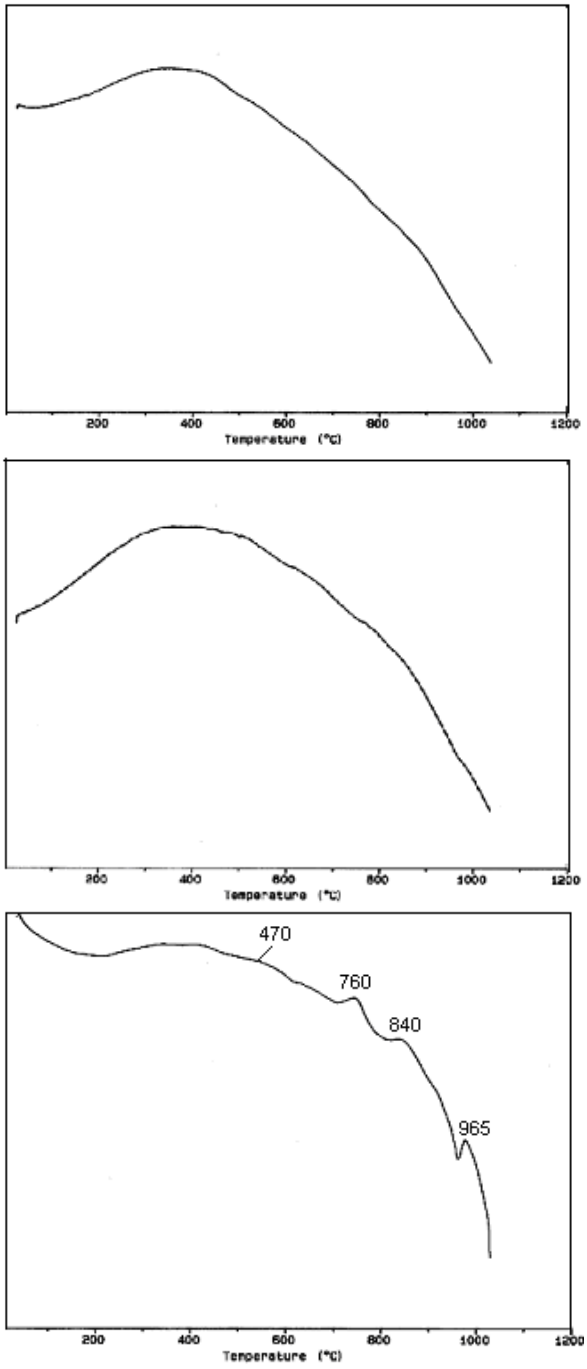

Fig. 2. DTA curves for (a) $40Fe_2O_3 \cdot 60[42B_2O_3 \cdot 58BaO]$, (b) $30Fe_2O_3 \cdot 70[37B_2O_3 \cdot 63SrO]$ and (c) $30Fe_2O_3 \cdot 70[37B_2O_3 \cdot 63CaO]$ samples.

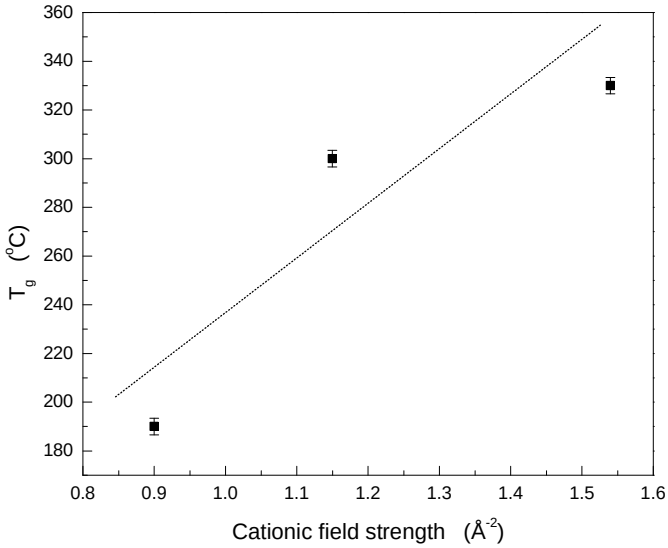

Fig. 3. Glass transition temperature versus cationic field strength.
The dotted line is guide to the eyes.

Table 2.
Glass transition, crystallisation temperatures and glass stability.

Cation	Ionic radius (Å)	Cationic field strength (Å^{-2})	Electronegativity (Pauling units)	B-O strength (kJ/mol)
B^{3+}	0.25	48	2.04	808.8 ±20.9
Ba^{2+}	1.49	0.90	0.89	561.9 ±13.4
Sr^{2+}	1.32	1.15	0.95	425.5 ±16.7
Ca^{2+}	1.14	1.54	1.00	402.1 ±16.7
Fe^{3+}	0.69	6.30	1.83	390.4 ±17.2

Conclusions

Vitreous state ternary systems were obtained by introducing up to 40 mol % Fe_2O_3 into eutectic composition of binary B_2O_3-CaO, B_2O_3-SrO and B_2O_3-BaO glass matrices. The glass stability of the investigated alkaline earth borate glass matrices depends on the alkaline earth cation. Fe_2O_3 addition enhances the glass stability, which supports the assumption that iron can act also as glass network former.

REFERENCES

1. Th. Klupsch, E. Steinbeiss, R. Mueller, C. Ulbrich, W. Schueppel,
1. H. Steinmetz, Th. Hoeche, J. Magn. Magn. Mat. 196-197 (1999) 264-265
2. B.T. Shirk, W.R. Buessem, J. Am. Ceram. Soc. 53 (1970) 192.
3. P. Goernert, E. Sinn, W. Schuppel, H. Pfeiffer, M. Rosler,. Th. Schubert, M. Jurisch, R. Selleger, IEEE Trans. Magn. 26 (1990) 12.
4. A. Staneva, E. Gattef, Y. Dimitriev, M.l Mikhov, J. Geshev, Solid State Sciences 6 (2004) 47
5. M. Tashiro, S. Sakka, T. Kokubo, J. Ceram. Assoc. Jpn. 72 (1964) 20.
6. H. Tanigawa, H. Tanaka, K. Osaka, Giujtsu Shikenso Kiho 15 (1964) 285.
7. J. Schuele, S. Shtrikman, D. Treves, J. Appl. Phys. 36 (1965) 1010.
8. R.R. Shaw, J.H. Heasley, J. Am. Ceram. Soc. 50 (1967) 297.
9. J. Sestak, K. Zaveta, F. Roskovecv, F. Zounova, J. Am. Ceram. Soc. 55 (1972) 537.
10. J. Sestak, J. Therm. Anal. 5 (1973) 669.
11. E.A.Weaver, US patent 4,042,519, August, 1977.
12. M.R. Guire, R.C. O'Handley, K. Kalonji, M.D. Dyar, J. Non-Cryst. Solids 81 (1986) 351.
13. E. Hanga, E. Tataru, M. Morariu, I. Diamadescu, L. Amandescu, N. Popescu-Pogrion, Phys. Status Solidi (a) 67 (1981) 725.
14. P. Auric, N. Van Dang, A.K. Bandyopadhyay, J. Zarzycki, J. Non-Cryst. Solids 50 (1982) 97.
15. W.J.S. Blackburn, B.P. Tilley, J. Mat. Sci., 9 (1974) 1265
16. M. Kawashita, Int. J. Appl. Ceram. Technol. 2 (2005) 173
17. E.T. Carlson, J. Res. Natl. Bur. Stand. (U.S.), 9, (1932) 825
18. H. Witzmann, G. Herzog, Z. Phys. Chem., 225, (1964) 197
19. E.M. Levin, G.M. Ugrinic, J. Res. Natl. Bur. Stand. (U.S.), **51** (1953) 197
20. J.A. Kerr in CRC Handbook of Chemistry and Physics, D.R. Lide, (ed.) CRC Press, Boca Raton, Florida, USA, 81-st edition, 2000
21. E.B. Araujo , J.A. Eiras , E.F. de Almeida J.A.C.de Paiva&A.S.B.Sombra, Phys.Chem.Glasses, 40, 5 (1999) 273.
22. L. Barbieri, A.B. Corradi, C. Leonelli, C. Siligardi, T. Manfredini, G.C. Pellacani,
23. Mat. Res. Bull., 32 (1997) 637
24. J.M. Jewell, M.Spess, R.L. Ortolano, J.E. Shelby, J. Am. Ceram. Soc., 74 (1991) 92
25. Y. D. Yiannopoulos, G. D. Chryssikos, E. I. Kamitsos, Phys. Chem.Glasses, 42 (2001) 164

STUDIA UNIVERSITATIS BABEŞ-BOLYAI, PHYSICA, LI, 1, 2006

ZERO MAGNETIC FIELD INFLUENCE ON MALE REPRODUCTIONS CELLS PROGRESSIVE MOTILITY DISTRIBUTION

Z.TRUTA[1], STELA LERINTIU[2], MARINELA GARLOVANU[2], V.V.MORARIU[3]

ABSTRACT. Human male reproductions cells progressive motility distributions was investigated in zero magnetic field (ZMF) and geomagnetic field (GMF) as control. Rapid progressive , slow progressive and immobile cells categories were studied in vitro at 22^0C. This experiment was done on ten patients with normozoospermia. The purpose was to characterize relationships between common semen quality and fertility estimates in ZMF and GMF as control. A difference in proportion of rapid progressive, slow progressive and immobile spermatozoa categories in ZMF and GMF was recorded.

Rapid progressive cells were observed in greater proportion in ZMF than GMF. When comparison was made on slow progressive cells the results was different, the proportion was greater in GMF than ZMF in most of cases. These results demonstrate that in ZMF we can increase the rapid progressive spermatozoa proportion significantly (10-20% from 3 to 18 hours after the ejaculate) and as a result the fertility estimate for in vivo and in vitro cases.

1. Introduction

Human semen contains seminal liquid and spermatozoa (reproductive cells). The reproductive cells number, motility, velocity, shape and form characterize the semen common quality and fertility. For mostly normal shapes and number of cells, the proportion of rapid progressive cells determines the fertility estimate in vivo or in vitro. Semen biochemical properties are mostly given by the extra cellular medium. Among these properties, pH and buffering capacity, osmolarity, ionic strength, and rheological properties play dominant roles in the physico-chemical processes that govern drug release kinetics and delivery vehicle distribution [1].

The exposure to various kinds of radiation influence in a different way the human reproductive cells, stimulating or inhibiting certain functions. Exposure to electromagnetic, electric, magnetic, static or variable fields influence the movement of cells, which is based on specific cell organelles (cilia, flagella), depending of the molecular mechanism involved [2].

Sperm motility is generated by highly organized, microtubule-based structure, called the axoneme, which is constructed from approximately 250 proteins. The force of flagellar movement is exerted by the sliding of outer-

[1] Faculty of Phisics, Babes-Bolyai University, 400084, Cluj-Napoca, Romania
[2] I.V.F.Laboratory, Cluj-Napoca, Romania
[3] INCDTIM, 4000293, Cluj-Napoca, Romania

doublet microtubules driven by the molecular motors, the dyneins [8]. The average curvilinear velocity increase with temperature with a rate of about 1μm/s for 1^0C between 25 – 31^0C for normal human spermatozoa [3]. Zero magnetic fields enhance the velocity and motility of human spermatozoa [4]. In some cases velocity is reduced to absolute stoppage at ZMF exposure (ependymal cilia, [5]).

Extremely low frequency electromagnetic fields exposure might impair mammalian female reproductive potentiality by reducing the capacity of the follicles to rich developments stage. However, no induction of chromosome aberrations in human spermatozoa exposed to extremely low frequency electromagnetic field was reported [6].

Exposure to radio electromagnetic radiation negatively impact human semen quality and fertility. DNA damage to caudal epididymal spermatozoa was assessed by quantitative QPCR as well as alkaline and pulsed field gel electrophoresis [7].

Our goal was to investigate the rapid progressive, slow progressive and immobile cells proportion changes response in human semen as result to ZMF exposure.

2. Experimental

Human semen is a viscous material, a mixture of components produced by several different glands. Its pH is reported between 7.3 - 8.4 by most studies [9]. In our experiments we studied the spermatozoa cells, which make up only the small portion of the whole semen, 1% to 5% of the total volume (Mortimer, 1994). Rapid progressive, slow progressive and immobile spermatozoa was counted using an inversed research microscope and a Makler counting chamber with a grid of 100μm and a height of 10μm ($1:10^6$ counting scale). The counting was done on 10 squares in 5 or 6 different locations of the specimen and the results was normalized and mediated for each counting measurement set. We used the length of time since ejaculate as the main variable and we divided the experiment time in 3 or 4 hours time intervals. The counting was done repeatedly by 2 researchers at each measurement time on homogenized specimen at 22^0C. We used a secondary system composed of a CCD camera, connected to our research microscope, and a PC with video imaging, for counting and velocity measurements control.

3. Results and Discutions

We present the averaged proportion of rapid progressive spermatozoa in the whole semen as the most important proportion that characterize the common semen quality and the fertility estimates in vivo and in vitro (Fig.1).

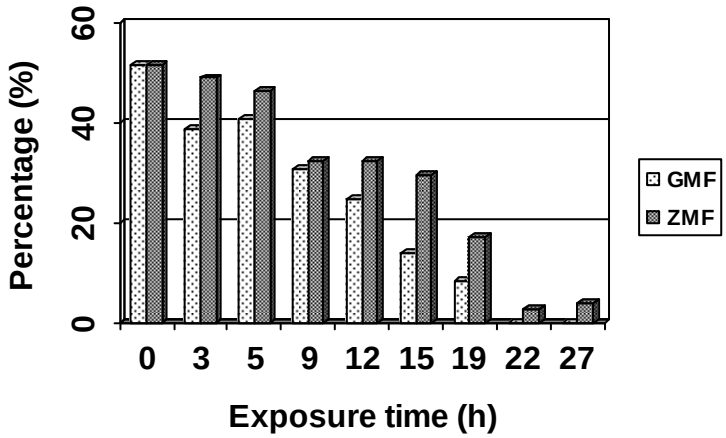

Fig.1. Percentage of rapid progressive cells in ZMF and GMF, at 22^0 C

We recorded a difference of 25,7% between the ZMF and GMF proportion of the rapid progressive cells after 3 hours of exposures in the first period of time after ejaculate (Fig.1). These differences in proportion, for this group of cells, was maintained for the next 20 hours between 10 and 30% until there was no more rapid progressive spermatozoa in the GMF expose specimen (Fig.1). After 27 hours of exposure we still recorded a percentage of 3.2% of rapid progressive spermatozoa in ZMF although in GMF this group of cells were practically inexistent at 22 hours after ejaculate (Fig.1).

In (Fig.2) we present the averaged proportion of slow progressive cells.

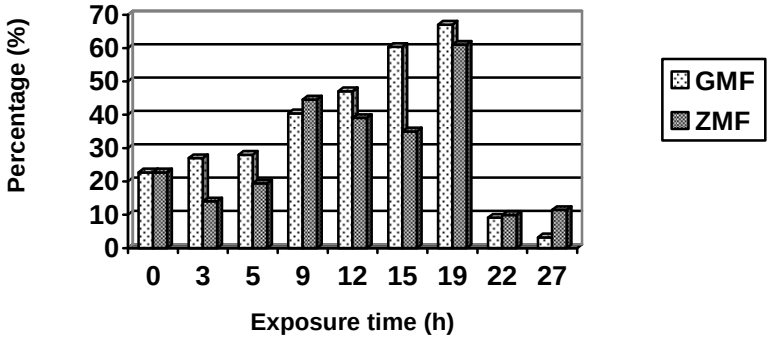

Fig. 2. Percentage of slow progressive cells in ZMF and GMF, at 22^0 C

In the case of slow progressive spermatozoa we did not record a consistent difference between the ZMF and GMF exposed specimen (Fig.2). Naturally the spermatozoa velocity is decreasing after the ejaculation from the initial value (25 to 50µm/s) to stoppage, when the spermatozoa are immobile. When the velocity is under 16µm/s the cell is considerate to belong to the slow progressive group. After 5 hours of exposure the ZMF slow progressive spermatozoa group was with 64,6% higher then GMF (Fig.2). The difference shifted after 12 hours, when we recorded 30,64% higher proportion for GMF exposed specimen related to ZMF (Fig.2).

For this category of cells the only consistent difference appeared to be after 22 hours of exposure when there were no more rapid progressive cells to shift naturally to the slow progressive group, all spermatozoa counted in de semen at the time specified being slow progressive or immotile (Fig.2).

In (Fig.3) we present the averaged proportion of immobile cells.

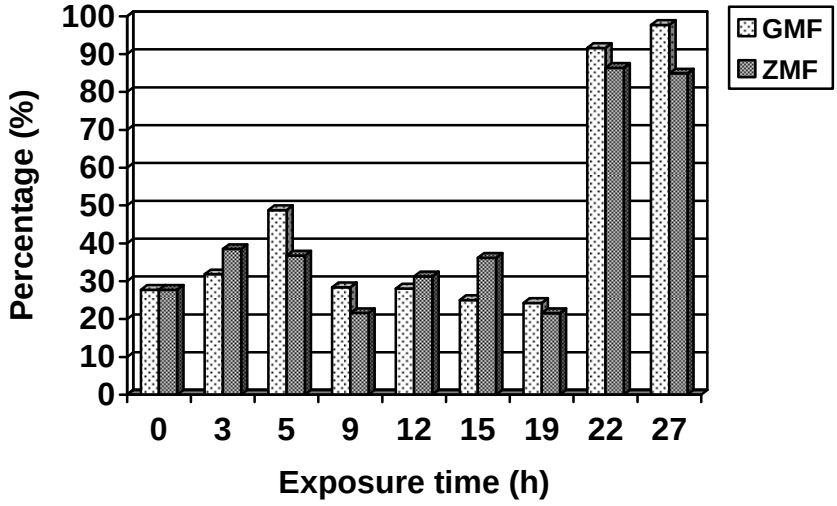

Fig. 3. Percentage of immobile cells in ZMF and GMF as control, at 22^0 C

We did not record a consistent difference between the ZMF and GMF exposed specimen for the first period of 22 hours, however the variations was smaller then in the case of slow progressive cells (Fig.2 and Fig .3)

Immobile spermatozoa proportion was maintained (between 25% - 40%) for the first 22 hours after ejaculate (Fig.3). After 22 hours the shifting to the immobile group cells was massive in both cases ZMF and GMF (Fig.3). However between 22 and 27 hours we recorded a difference in percentage of immobile spermatozoa (between 2 – 5%), GMF exposed specimen proportion was greater then ZMF exposed specimen (Fig.3).

4. Conclusions

In the case of normozoospermia, at 22^0C in vitro, ZMF delays the shifting of spermatozoa from progressive groups to immobile group with about 4 hours.

There is a critical length of time after ejaculation (about 22 hours, at 22^0C), when we recorded a massive shifting to the immobile cells group in both cases ZMF and GMF.

We suggest that the inconsistency we recorded in the slow progressive spermatozoa group is due to the nature of this category, which is just an intermediary shifting group between rapid progressive and immobile cells. These variations in percentage increase or decrease rate could be analized as a measurement of biological variations too. We further conclude that the slow progressive group of cells is not representative for characterizing the common semen quality or fertility estimates in the case of normozoospermia.

Rapid progressive spermatozoa percentage can be increased using ZMF incubation .We suggest that this increase is possible due to shifting of some of the slow progressive cells to the rapid progressive group cells during ZMF incubation.

REFERENCE

1. Derek H. Owen, David F. Katz, Journal of Andrology, 26(4), 459 (2005)
2. Fletcher D.A., Theriot J.A., Phys. Biol. 1, 1(1-2), T1-10 (2004)
3. J.Auger, Catherine Serres, Danielle Feneux,Cell Motility and the Cytoskeleton, 16(1), 22 (2005)
4. Z.Truta, Silvia Neamtu , V.V.Morariu, Rom.J.Biophys., 15(1-4),73 (2005)
5. V.Sandodze, I.K.Swnidze, E.V.Didimova, Radiats Biol Radioecol, 35(1), 19 (1995)
6. Sandra Cecconi, et all., Human Reproduction, 15(11), 2319 (2005)
7. R.J.Aitken, L.E.Bemnetts, D.Sawyer, A.M.Wiklendt, B.V. King, International Journal of Andrology, 28(6), 171 (2005)
8. Inaba K., Zoolog Sci., 20(9), 1043 (2003)
9. Haugen T.B., Grotmol T., Int. J. Andrology, 21(2), 105 (1998)

STUDIA UNIVERSITATIS BABEŞ-BOLYAI, PHYSICA, LI, 1, 2006

DWBA CALCULATIONS FOR POSITRON IMPACT IONIZATION OF O_2

I. F. TÓTH[1], R. I. CAMPEANU[2], V. CHIŞ[1] AND L. NAGY[1*]

ABSTRACT. We have carried out distorted wave calculations for positron impact ionization of O_2. Present results are compared to previously obtained ones with a more simple method, and with the results for other diatomic molecules. Our results suggest a very similar behavior of the distorted wave models as found in the case of the N_2 and CO molecules.

1. Introduction

Positron impact ionization of molecules is a research field initiated relatively recently. In the last two decades several experiments have been performed by different groups [1-5]. These experiments have involved the positron impact ionization of H_2, CO, CO_2, N_2, CH_4, and O_2. In the case of the O_2 molecule the measured ionization cross sections include also the contributions from positronium (Ps) formation [5]; there are no experimental data for the direct ionization process. The theoretical treatment of the ionization process induced by positrons is simpler than that induced by electrons, since there is no exchange interaction between the scattered positron and the ejected electron. In the last years there have been published a series of theoretical studies involving the calculation of total ionization cross sections for the direct ionization process of the above mentioned molecules. These studies [6-10] have employed the CPE (Coulomb plus plane waves with full energy range) model. The CPE model uses Coulomb waves to describe the ejected electron, while the motion of the incident and scattered positron is approximated by plane waves or Coulomb waves. The initial state of the active electron is described by multi-center, Gaussian-type wavefunctions.

In the present paper we employ the DWBA (Distorted Wave Born Approximation) method in order to describe the ionization of the O_2 molecule. In the framework of this approximation we have calculated the wavefunctions of the free particles by solving numerically the radial Schrödinger equation in the field of a more realistic potential. We have obtained this potential by spherically averaging the real potential created by the nuclei and the bound electrons. The effect of this screened potential is investigated separately on the scattered positron and the ejected electron.

[1] Faculty of Physics, Babeş-Bolyai University, 400084 Cluj, Romania
[2] Department of Physics and Astronomy, York University, 4700 Toronto, ON, Canada
[*] e-mail: lnagy@phys.ubbcluj.ro

Previously we have performed DWBA calculations [11] in the case of the N_2, CO, CO_2 and CH_4 molecules, and our results were in good agreement with experimental data measured for N_2 and CO. Here we present our results obtained for the direct ionization of the O_2 by positrons, and we compare these results with those obtained in the case of the other two diatomic molecules, N_2 and CO.

2. Theory

The detailed formalism for the ionization by positron impact of a molecule has been described elsewhere [6-10]. Here we give a short outline of the theory and we present some particularities for the O_2 case.

The triple differential cross-section for the ionization of a molecule by positron impact may be written as

$$\frac{d^3\sigma}{d\hat{\mathbf{k}}_f d\hat{\mathbf{k}}_e dE_e} = \sum_r \frac{(2\pi)^4}{E_i} \left| f_r \right|^2 . \tag{1}$$

Here E_i is the energy of the incident positron, E_e the energy of the ejected electron, while $\hat{\mathbf{k}}_e$ and $\hat{\mathbf{k}}_f$ stand for the direction of the momenta of the ejected electron and scattered positron, respectively. The summation over r is done over all occupied molecular orbitals. The amplitude can be written as

$$f_r = \left\langle \phi_f(\mathbf{r}_1)\phi_e(\mathbf{r}_2) \middle| V(r_{12}) \middle| \phi_i(\mathbf{r}_1)\phi_r(\mathbf{r}_2) \right\rangle , \tag{2}$$

where ϕ_i and ϕ_f stand for the wavefunction of the incident and scattered positron respectively, ϕ_e is the wavefunction of the ejected electron, while ϕ_r describes the initial state of the active electron. In the above amplitude $\mathbf{r}_1$ is the position vector of the positron, while $\mathbf{r}_2$ stands for the position vector of the active electron.

The ground state of the molecule has been described by Gaussian wavefunctions. In the case of linear molecules, the two-center or multi-center wavefunctions have been expanded in terms of Legendre polynomials:

$$\phi_r(\mathbf{r}_2) = \sum_{l_b} c_{l_b}(r_2, R_0) P_{l_b}(\cos\omega_2), \tag{3}$$

where $\mathbf{R}_0$ is the internuclear distance and ω_2 is the angle between $\mathbf{r}_2$ and $\mathbf{R}_0$. The expansion coefficients can be expressed with the following integral:

$$c_{l_b}(r_2, R_0) = \frac{2l_b + 1}{2} \int_{-1}^{1} d(\cos\omega_2) P_{l_b}(\cos\omega_2) \phi_r(\mathbf{r}_2). \quad (4)$$

By this method [6-10] the triple differential cross section for the ionization of a molecule by positron impact may be expressed as a sum of cross sections characterized by a certain angular momentum of the initial state

$$\frac{d^3\sigma}{d\hat{\mathbf{k}}_f d\hat{\mathbf{k}}_e dE_e} = \sum_r \sum_{l_b m_b} \frac{(2\pi)^4}{E_i} \left| f_r^{l_b m_b} \right|^2 , \quad (7)$$

where $f_r^{l_b m_b}$ denotes the partial scattering amplitude for orbital *r* with the angular momentum of the initial state characterized by l_b and m_b. In order to calculate the total ionization cross section, one has to integrate over the angles of the ejected electron and scattered positron as well as the energy of the ejected electron. Further, the method assumes that the electron orbitals in the residual molecular ion are the same as in the target molecule during the time of the collision. In the case of the O_2 molecule the molecular orbitals have been calculated in the unrestricted Hartree-Fock formalism (different spatial orbitals for electrons of α and β spin). This was necessary because O_2 has a paramagnetic behavior (there are two electrons with the same orientation of the spin on the last occupied orbital $2p\pi_g$), and once the value of the magnetic spin quantum number of the molecule is fixed, the two spin directions are not equivalent. For each of the internal orbitals ($2s\sigma_g$, $2s\sigma_u$, $2p\sigma_g$, $2p\pi_u$) we have considered separately the contributions from α and β electrons.

Our DWBA approximation includes a spherically averaging method. We have employed this method to obtain a more realistic potential by spherically averaging the real potential created by the nuclei and the bound electrons, and have calculated the wavefunctions of the continuum states numerically in this screened field of the molecule. The radial part of the continuum states were obtained from the Numerov-integration of the radial Schrödinger equation, while the normalization of these states was performed by employing the method of Burgess [12].

Spherically averaging the potential created by the electrons being on the orbital *r* we obtain:

$$V_{electrons}^{r}(r') = -n_r \frac{1}{4\pi} \int \frac{|\phi_r(\mathbf{r}_2)|^2}{r_>} d\mathbf{r}_2 , \quad (8)$$

where $r_\rangle$ denotes the greater between r_2 and r' (the distance from the center of the considered sphere), while n_r is the number of the electrons on the orbital. The total potential created by all the electrons may be written as

$$V_{electrons} = \sum_r V^r_{electrons}(r'). \tag{9}$$

The potential created by the electrons was calculated separately for the ejection of the electron from each orbital and spin state, because in each case another electron is missing. The real potential of the nuclei was spherically averaged by rotating the molecule in all directions around the center of mass. From this rotation we obtain a sphere with radius $R_0/2$ and a uniform distribution of the nuclear charge on the surface of this sphere. Mathematically,

$$V_{nuclei} = \frac{2Z}{R_0/2}, \text{ for } r' \langle \frac{R_0}{2}$$

or (10)

$$V_{nuclei} = \frac{2Z}{r'}, \text{ for } r' \rangle \frac{R_0}{2},$$

where Z is the atomic number. Since we are going to make a comparison between the different diatomic molecules, we note that in the case of CO we obtain from the rotation of the molecule two spheres with different radii.

The expressions (9) and (10) lead to the resulting potential, where the spherically averaged potential of the nuclei is screened by the spherically averaged potential created by the electrons:

$$V_x = V_{nuclei} + V_{electrons}\ , \tag{11}$$

where $x = i, f, e$. Here, the $x = i$ subscript denotes the potential used in the calculation of the wavefunction of the incident positron. When $x = f$, we have used the expression of (11) to calculate the wavefunction of the scattered positron, while in the $x = e$ case the wavefunction of the ejected electron was calculated.

We have considered two models in order to introduce the distortion of the incoming and outgoing waves gradually, and to investigate the effect of each change in the wave representation. The first model assumes that when the scattered positron is faster than the ejected electron the positron moves in the field of the neutral molecule and the electron moves in the spherically averaged potential field created by the nuclei and by the remaining electrons (after the ionization). When the ejected electron is

faster than the scattered positron the positron moves in the field of the positive ion, while the electron moves in the averaged potential created by the nuclei and the positron screened by the averaged field of the remaining electrons. In addition, the model assumes that the incident positron moves in the field of the neutral molecule. We call this model the Electron Screening (ES) model, since the screened potentials have been used only for calculating the wavefunction of the ejected electron.

The second model assumes that when the scattered positron is faster than the ejected electron the positron moves in the averaged field of the nuclei and all electrons, while the ejected electron moves in the averaged field of the nuclei and the remaining electrons. When the ejected electron is faster than the scattered positron, the positron moves in the averaged field of the nuclei and the remaining electrons, while the ejected electron moves in the averaged field of the nuclei and the positron screened by the averaged field of the remaining electrons. In addition, the incoming positron moves in the averaged potential field created by the nuclei and by the complete system of the electrons. We have named this model as Total Screening (TS) model, since the screened potentials have been used for calculating wavefunctions for both the incoming and outgoing particles.

3. Results and Discussion

Figs. 1, 2 and 3 show our total ionization cross-sections obtained in the case of the N_2, CO and O_2 molecules. In these figures we present results corresponding to models CPE, ES and TS. Figs. 1 and 2 show also the experimental data of Bluhme et al [1]. In the case of the O_2 molecule there are no available experimental data for the direct ionization process. However, we present results obtained for this molecular target in figure 3.

Figs. 1 and 2 show that our ES and TS distorted wave models produce results in good agreement with experimental data in the case of N_2 and CO molecules, respectively. The agreement is very good especially in the case of the ES model, while the TS model produces very good agreement particularly at energies higher than 200 eV. In both cases the CPE model gives ionization cross-sections a slightly higher than the experimental ones. Further, one may observe that in both of these cases the cross-sections obtained with the CPE model are higher than those obtained with our distorted wave models. In the region of the peak, the ES model produces cross-sections higher than those obtained with the TS model. One may observe from these figures that the peak produced by our distorted wave models is shifted in both cases to lower energies than that obtained in the CPE case.

In fig. 3 we present our present results obtained for the O_2 molecule. We found that the applied distorted wave models produce cross-sections lower than CPE cross-sections particularly in the region of impact energies

higher than 500 eV. For lower energies the results obtained with the TS model are similar with CPE results, while for the ES model we found higher results relative to the CPE

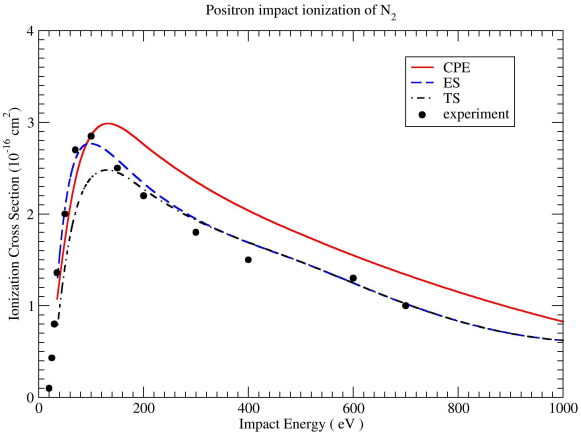

Fig. 1. Total cross-sections for positron impact ionization of N_2 as a function of the positron impact energy. The experimental points are from Bluhme et al. [1].

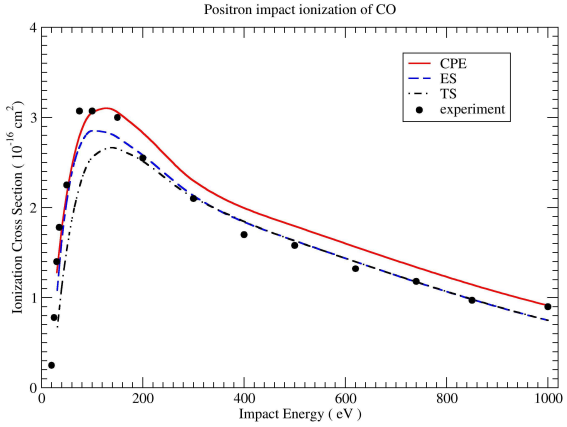

Fig. 2. Total cross-sections for positron impact ionization of CO as a function of the positron impact energy. The experimental points are from Bluhme et al. [1].

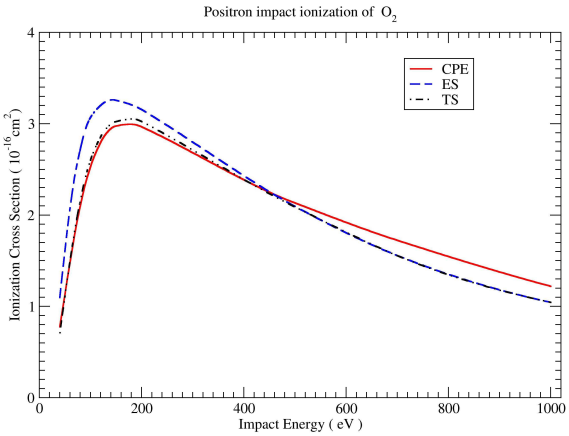

Fig. 3. Total cross-sections for positron impact ionization of O_2 as a function of the positron impact energy.

cross sections, especially in the region of the peak. However, our distorted wave models show a similar behavior as found in the N_2 and CO case. For lower energies, the cross sections obtained with the ES model are higher than that obtained with the TS model and the peak produced by these models is shifted to lower energies, compared to the position of the peak obtained in the case of the CPE model.

4. Conclusions

In the present paper we have performed DWBA calculations for the positron impact ionization of the O_2 molecule. We have calculated the wavefunctions of the ejected electron and the scattered positron in a spherically symmetric screened potential. Unfortunately, there are no available experimental results for the direct ionization of this molecular target. However, the present results have been compared to our previous results obtained for the N_2 and CO diatomic molecules. We found that our distorted wave models ES and TS, applied to the O_2, produce very similar shapes for the ionization cross-sections as those obtained in the case of the N_2 and CO molecules. It would be interesting to compare these cross-sections to the future experimental data.

Acknowledgement

The research of I. F. Tóth has been supported by KPI Sapientia Foundation.

REFERENCES

1. H. Bluhme, N. P. Frandsen, F. M. Jacobsen, H. Knudsen, J. Merrison, R. Mitchell, K.
2. Paludan, M. R. Poulsen, J Phys. B: At. Mol. Opt. Phys. **32** (1999) 5825.
3. H. Knudsen, L. Brun-Nielsen, M. Charlton, M. R. Poulsen, J. Phys. B: At. Mol. Opt.
4. Phys. **23** (1990) 3955.
5. J. Moxom, P. Ashley, G. Laricchia, Can. J. Phys. **74** (1996) 367.
6. F. M. Jacobsen, N. P. Frandsen, H. Knudsen, U. Mikkelson, D. M. Schrader, J. Phys.
7. B: At. Mol. Opt. Phys **28** (1995) 4675.
8. G. Laricchia, J. Moxom, M. Charlton, Phys. Rev. Lett. **70** (1993) 3229.
9. R. I. Campeanu, V. Chis, L. Nagy, A. D. Stauffer, Phys. Lett. A **310** (2003) 445.
10. R. I. Campeanu, V. Chis, L. Nagy, A. D. Stauffer, Phys. Lett. A **344** (2005) 247.
11. R. I. Campeanu, V. Chis, L. Nagy, A. D. Stauffer, Nucl. Instr. Meth. B **221** (2004) 21.
12. R. I. Campeanu, V. Chis, L. Nagy, A. D. Stauffer, Nucl. Instr. Meth. B **247** (2006) 58.
13. R. I. Campeanu, V. Chis, L. Nagy, A. D. Stauffer, Phys. Lett. A **325** (2004) 66.
14. I. Tóth, R. I. Campeanu, V. Chiş and L. Nagy, Phys. Lett. A, **360** (2006) 131.
15. A. Burgess, Proc. Phys. Soc. **81** (1963) 442.

STUDIA UNIVERSITATIS BABEŞ-BOLYAI, PHYSICA, LI, 1, 2006

RESONANCE EFFECTS IN QUANTUM TRANSITIONS INDUCED BY ULTRASHORT LASER PULSES WITH HIGH REPETITION RATE

S. BORBÉLY AND L. NAGY*

ABSTRACT. In the present work we investigate the interaction between a quantum system and an external laser field with high repetition rate. The presence of resonance effects in the quantum transitions is shown using an analytical approach. The interaction between the system and the laser field is described by the first order approximation of the time dependent perturbation theory. In the case of photoionization we established a threshold for the repetition rate, above which these resonance effects could be measured experimentally.

Introduction

Due to the recent technological development many experiments are performed with laser pulses of various intensities, repetition rates and durations. They interact with targets such as atoms, molecules, clusters and solids[1-3]. Valuable information can be extracted from experimental data only by the use of reliable theoretical models.

The interaction of external laser field and quantum mechanical system can be described by the time dependent Schrödinger equation (TDSE). In most cases this equation may be solved only numerically by the solution of the coupled state equations using different basis sets (Sturmian states [4], B-splines [5], etc.) or by other methods[6].

The main disadvantage of the fully numerical approaches is that they need very high computational power, consequently for complex systems (with two or more active particles) other methods based on the approximate solution of TDSE are used [7-10].

The simplest approach is based on the time dependent perturbation theory (TDPT), which gives quantitatively good results in the perturbation region. However, the TDPT could produce qualitatively good description of the transitions outside of the perturbation region, too.

In the present work we choose the TDPT approach, because our goal is to reveal the main characteristics of the resonance effects in the studied transition. In the previous theoretical studies the laser pulses are treated separately [7-10], while we study the entire pulse train. Atomic units are used throughout unless otherwise stated.

* Faculty of Physics, Babeş-Bolyai University, Kogălniceanu str. nr. 1, 400084 Cluj, Romania
Email address: lnagy@phys.ubbcluj.ro

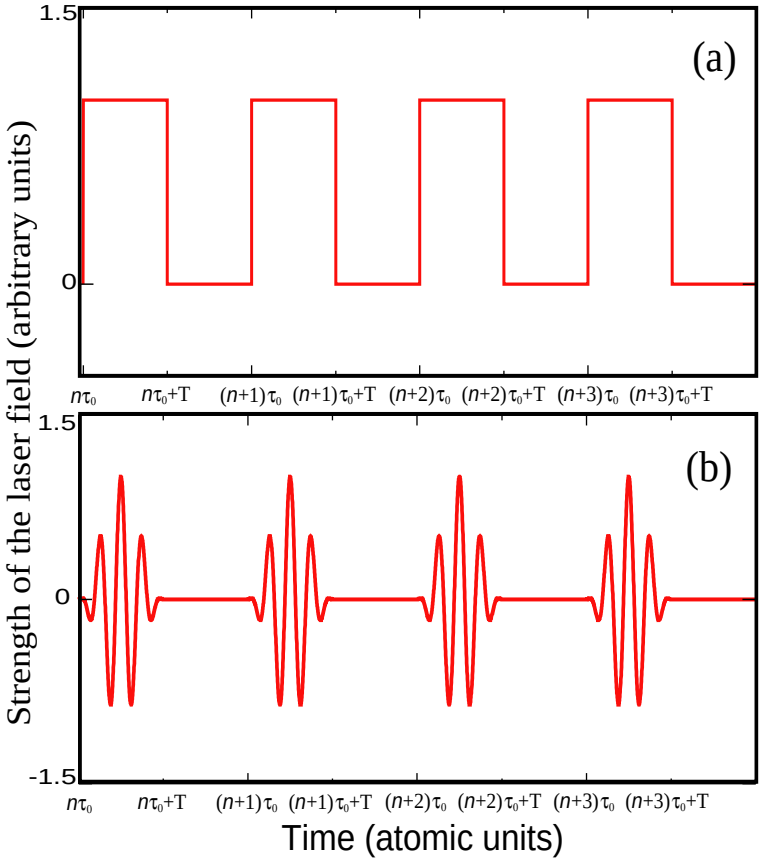

Fig.1. The shape of the used laser pulses (a) rectangular pulses, (b) time-symmetric sine-square pulses $\phi_0 = \frac{\pi}{2} - \frac{\omega T}{2}$

Theory

The external laser field is considered linearly polarized along the polarization vector $\hat{\varepsilon}$.

The shape of individual pulses are described by simple analytic functions $f(t)$. In case of rectangular pulse (see Fig. 1. (a)) we have

$$f(t) = \begin{cases} 1 & \text{if } t \in (0,T) \\ 0 & \text{elsewhere} \end{cases}, \tag{1}$$

while in case if sine-square pulse (see Fig. 1. (b)) we have

$$f(t)=\begin{cases}\sin^2\left(\dfrac{\pi t}{T}\right)\sin\left(\omega t+\phi_0\right) \text{ if } t\in(0,T)\\ 0 \qquad\qquad\qquad \text{elsewhere}\end{cases}, \tag{2}$$

where T is the pulse duration, ω is the main frequency of the laser field and ϕ_0 is the absolute phase of the laser field also called carrier-envelope phase.

The pulse train may be constructed as a sum of individual pulses (see Fig. 1.) and the external electric field at the center of the system is described as

$$\vec{E}=\sum_{n=0}^{\infty}\hat{\varepsilon}E_0 f(t-n\tau_0), \tag{3}$$

where τ_0 is the time interval between two pulses. Using the dipole approximation and equation (3), for the perturbation potential in length gauge we obtain

$$U(t)=\hat{\varepsilon}\vec{r}E_0\sum_{n=0}^{\infty} f(t-n\tau_0). \tag{4}$$

The probability amplitude for the transition from quantum state i to quantum state f, using the first order approximation of the time dependent perturbation theory, is given by

$$a^{(1)}=-i\int_0^t dt' e^{i\omega_{fi}t'}\left\langle\Psi_f\mid U(t')\mid\Psi_i\right\rangle, \tag{5}$$

where $\omega_{fi}=E_f-E_i$ is the energy difference between the two quantum states described by Ψ_i and Ψ_f wavefunctions.

The contribution of a single pulse for the transition amplitude is

$$a_m^{(1)}=-iE_0\left\langle\Psi_f\mid\hat{\varepsilon}\vec{r}\mid\Psi_i\right\rangle\int_0^t dt' e^{i\omega_{fi}t'} f(t'-m\tau_0), \tag{6}$$

which after basic transformations becomes

$$a_m^{(1)}=-iE_0\left\langle\Psi_f\mid\hat{\varepsilon}\vec{r}\mid\Psi_i\right\rangle e^{i\omega_{fi}m\tau_0}\int_0^T e^{i\omega_{fi}t} f(t)dt. \tag{7}$$

Using the notation

$$\mathrm{F}(T,\ \omega,\ \omega_{fi}) = \int_0^T e^{i\omega_{fi}t} f(t)dt \tag{8}$$

equation (7) becomes

$$a_m^{(1)} = -iE_0 \left\langle \Psi_f \mid \hat{\varepsilon}\vec{r} \mid \Psi_i \right\rangle \mathrm{F}(T,\ \omega,\ \omega_{fi}) \tag{9}$$

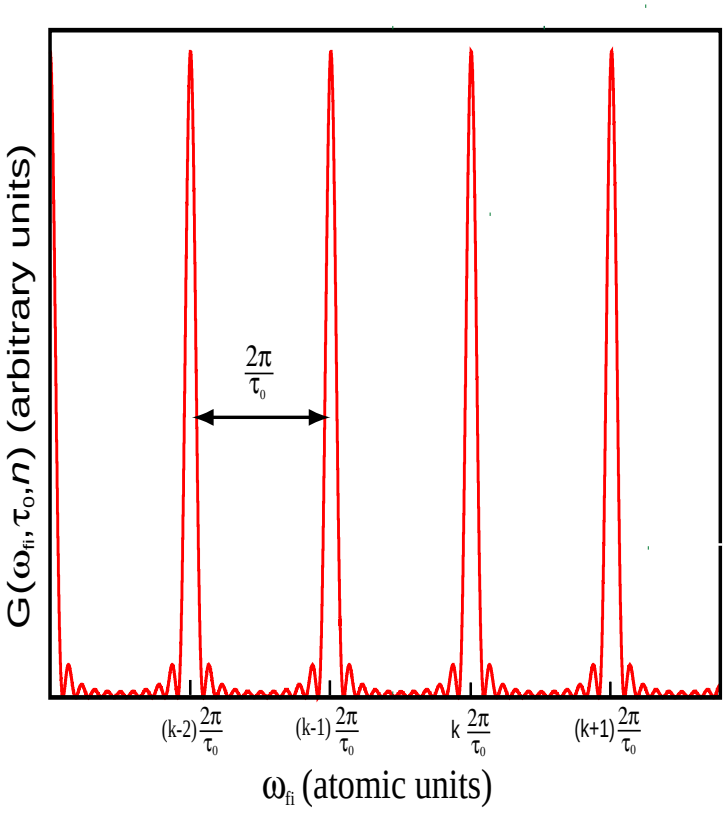

Fig. 2. $\mathrm{G}(\omega_{fi},\ \tau_0,\ n)$ as a function of ω_{fi} with $\tau_0 = 25\,a.u.$ and $n = 10.$

The probability amplitude for the first n pulses is written as a sum of the separate amplitudes defined by (9)

$$a^{(1)} = \sum_{m=0}^{n-1} a_m^{(1)} = -E_0 \left\langle \Psi_f \mid \hat{\varepsilon}\vec{r} \mid \Psi_i \right\rangle \mathrm{F}(T,\ \omega,\ \omega_{fi}) \sum_{m=0}^{n-1} e^{i\omega_{fi} m\tau_0}. \tag{10}$$

The evaluation of the sum in the above equation leads to

$$a^{(1)}(n) = -iE_0 \left\langle \Psi_f \mid \hat{\varepsilon}\vec{r} \mid \Psi_i \right\rangle \mathrm{F}(T,\ \omega,\ \omega_{fi}) \left[\frac{1 - e^{i\omega_{fi} n\tau_0}}{1 - e^{i\omega_{fi}\tau_0}} \right]. \qquad (11)$$

The last factor in equation (11) appears due to the interference between the spectral components of the different pulses and it describes the influence of the spectral interference [11].
The transition probability is the square of the modulus of the probability amplitude defined by (11).

$$P_{fi}(n) = E_0^2 \left| \left\langle \Psi_f \mid \hat{\varepsilon}\vec{r} \mid \Psi_i \right\rangle \right|^2 \left[\frac{\sin\left(\frac{\omega_{fi} n\tau_0}{2} \right)}{\sin\left(\frac{\omega_{fi}\tau_0}{2} \right)} \right]^2 \left| \mathrm{F}(T,\ \omega,\ \omega_{fi}) \right|^2. \qquad (12)$$

Discussion

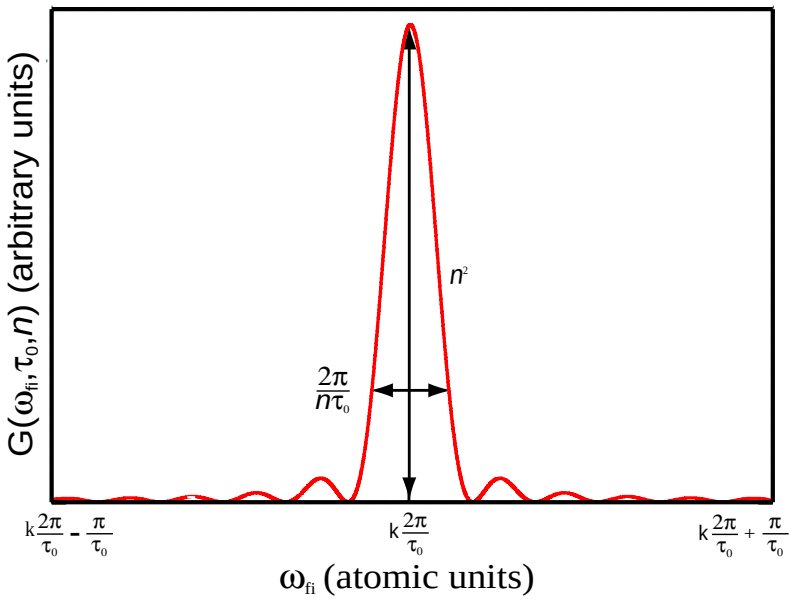

Fig. 3. The shape of the k-th peak from the spectrum of $\mathrm{G}(\omega_{fi},\ \tau_0,\ n)$ plotted on

The transition probability could be constructed as a product of three factors, each having a well defined physical meaning.

The first is the matrix element factor $E_0^2 \left| \left\langle \Psi_f \mid \hat{\varepsilon}\vec{r} \mid \Psi_i \right\rangle \right|^2$, which is proportional with the square of the absolute value of dipole transition matrix element.
The second one is denoted by

$$\mathrm{G}(\omega_{fi},\ \tau_0,\ n) = \left[\frac{\sin\left(\frac{\omega_{fi} n \tau_0}{2} \right)}{\sin\left(\frac{\omega_{fi} \tau_0}{2} \right)} \right]^2 \tag{13}$$

and is the resonance factor, which describes the influence of the spectral interference on the transition probability.
It is easy to notice that for large values of n, the expression $\mathrm{G}(\omega_{fi},\ \tau_0,\ n)$ has sharp maxima at each value of ω_{fi}, which satisfies the condition $\omega_{fi} = \frac{2k\pi}{\tau_0}$, where k is an integer (see Fig. 2.). These peaks are n^2 high, while their width is $\frac{2\pi}{n\tau_0}$ (see Fig. 3.).

The third factor is

$$\mathrm{H}(\omega_{fi},\ \omega,\ T) = \left| \mathrm{F}(T,\ \omega,\ \omega_{fi}) \right|^2 . \tag{14}$$

As equation (8) and (14) shows, $\mathrm{H}(\omega_{fi},\ \omega,\ T)$ is determined by the shape of individual pulses and it is directly connected with the Fourier spectra of the individual pulses.

In the present work calculations were performed with rectangular and sine-square pulses, for the shape of individual pulses see equation (1) and (2) .

$$\mathrm{H}(\omega_{fi},\ \omega,\ T) = \frac{1 - \cos(\omega_{fi} T)}{\omega_{fi}^2} \tag{15}$$

for rectangular pulses and

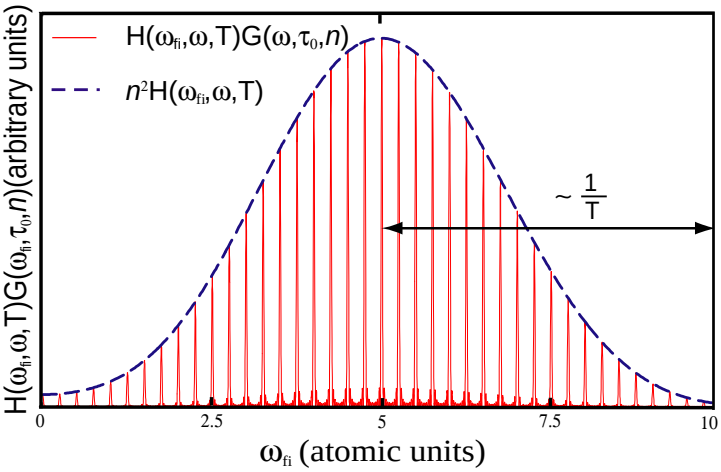

Fig. 4. $G(\omega_{fi},\ \tau_0,\ n)\,H(\omega_{fi},\ \omega,\ T)$ as a function of ω_{fi} for sine square pulses with $\tau_0 = 25\,a.u., \omega = 5\,a.u., T = 2,1\,a.u.$ and $n = 10$.

$$H(\omega_{fi},\ \omega,\ T) = 4\pi^4 \left| \frac{\omega\left[-4\pi^2 + \left(3\omega_{fi}^2 + \omega^2\right)\right]\left[\cos\left(\phi_0\right) - e^{i\omega_{fi}T}\cos\left(\omega T + \phi_0\right)\right]}{\left[\omega_{fi}^2 - \omega^2\right]\left[16\pi^4 - 8\left(\omega_{fi}^2 + \omega^2\right)\pi^2T^2 + \left(\omega_{fi}^2 + \omega^2\right)^2 T^2\right]} - \right.$$

$$\left. -i\frac{\omega_{fi}\left[-4\pi^2 + \left(3\omega^2 + \omega_{fi}^2\right)\right]\left[\sin\left(\phi_0\right) - e^{i\omega_{fi}T}\sin(\omega T + \phi_0)\right]}{\left[\omega_{fi}^2 - \omega^2\right]\left[16\pi^4 - 8\left(\omega_{fi}^2 + \omega^2\right)\pi^2T^2 + \left(\omega_{fi}^2 - \omega^2\right)^2 T^2\right]} \right|^2 \qquad (16)$$

for sine-square pulses.

In both cases $H(\omega_{fi},\ \omega,\ T)$ has a global maximum (the width of the maximum $\approx\frac{1}{T}$) placed at $\omega_{fi} = 0$ for rectangular pulses (see Fig. 4.) and at $\omega_{fi} = \omega$ for sine-square pulses (see Fig 5.) followed by several local maxima (in both cases the distance between the maxima is $\frac{2\pi}{T}$).

The shape of sine-square pulse is more closer to the experimental pulse than the rectangular one, which could lead to more reliable results for sine-square pulses.

In the special case, when T and τ_0 have close values for sine-square pulses $\mathrm{H}(\omega_{fi}, \omega, T)$ and $\mathrm{G}(\omega_{fi}, \tau_0, n)$ have a close periodicity, which

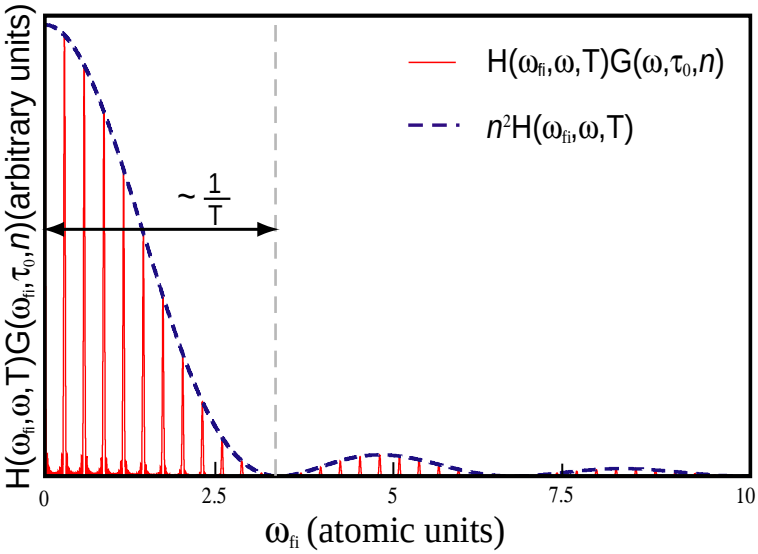

Fig. 5. $\mathrm{G}(\omega_{fi}, \tau_0, n)\,\mathrm{H}(\omega_{fi}, \omega, T)$ as a function of ω_{fi} for sine square pulses with $\tau_0 = 25\,a.u., \omega = 5\,a.u., T = 2.1\,a.u.$ and $n = 10$.

leads to beating like effects (see Fig. 6.).

The beating angular frequency is

$$2\pi\nu_b = \frac{2\pi}{\tau_0 - T}, \tag{17}$$

which makes connection between T and τ_0. It is worth to mention that this beating is not a real effect. It appears due to sine-square envelope function, which introduced a periodic envelop function in the Fourier spectrum of the pulses. The experimentally produced laser pulses do not have this periodicity in the Fourier spectrum.

In the case when the pulse duration is much smaller than the time between the pulses $(T \gg \tau_0)$ the decisive factor of the transition probability is $\mathrm{G}(\omega_{fi}, \tau_0, n)$.

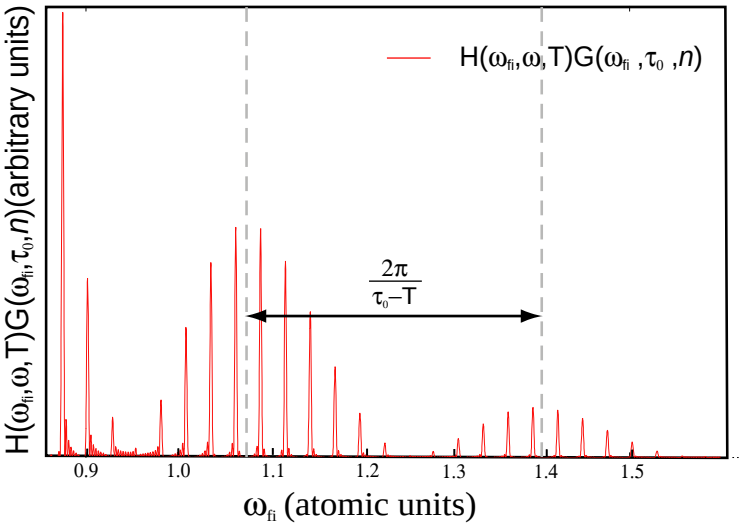

Fig. 6. $G(\omega_{fi},\ \tau_0,\ n)\,H(\omega_{fi},\ \omega,\ T)$ as a function of ω_{fi} for sine square pulses with $\tau_0 = 230\,a.u.(5.47\ fs), \omega = 0.056\,a.u.(800\,nm), T = 210\,a.u.(5\,fs)$ and $n = 10$.

In this situation is easy to observe the presence of resonance for large values of n, because we have significant transition probability only if condition $\omega_{fi} = \dfrac{2k\pi}{\tau_0}$ is fulfilled, which is equivalent with the fact that due to the spectral interference, in the Fourier spectrum of the laser pulse train only the above mentioned photon energies are present with significant weight.

In the expression of the transition probability $G(\omega_{fi},\ \tau_0,\ n)$ is modulated (see Fig. 5. and 6.) by $H(\omega_{fi},\ \omega,\ T)$, which is slowly varying function (pulse duration T is considered much smaller than the time between two pulses τ_0).

In most practical cases we are interested in quantum transitions, where the final state is a continuum state, like in the case of ionization of atoms or molecules. In these cases the theoretical spectrum of the ejected electron given by (12) could not be obtained experimentally due to the finite energy resolution of the used electron spectrometer. The measured transition probability is the average of expression (12) over a narrow energy interval defined by the energy resolution (η) of the electron spectrometer.

Let us calculate the average of the transition probability over the interval $(E_f - \eta, E_f + \eta)$:

$$\overline{P}_{fi}(n) = \frac{1}{2\eta} \int_{E_f - \eta}^{E_f + \eta} P_{fi}(n) dE_f' \tag{18}$$

In the integration domain $\left|\mathrm{F}(T, \omega, \omega_{fi})\right|^2$ and $E_0^2 \left|\left\langle \Psi_f \mid \hat{\varepsilon}\vec{r} \mid \Psi_i \right\rangle\right|^2$ could be considered as constants, because η is sufficiently small and $T \gg \tau_0$. Taking into account the above considerations the averaged transition probability defined by (18) became

$$\overline{P}_{fi}(n) = \frac{E_0^2}{2\eta} \left|\left\langle \Psi_f \mid \hat{\varepsilon}\vec{r} \mid \Psi_i \right\rangle\right|^2 \left|\mathrm{F}(T, \omega, \omega_{fi})\right|^2 \int_{E_f - \eta}^{E_f + \eta} \mathrm{G}(\omega_{fi}, \tau_0, n) dE_f' \tag{19}$$

As it could be observed on Fig. 2, and Fig. 3, the characteristic energy scale in the spectrum of the ejected electron is $\frac{2\pi}{\tau_0}$. If we choose $\eta = \frac{\pi}{\tau_0}$ the integration domain will contain at least one sharp maximum of $G(\omega_{fi}, \omega, n)$. Based on the above considerations the integral in equation (19) may be approximated by $\frac{2\pi n}{\tau_0}$, while the averaged transition probability becomes

$$\overline{P}_{fi}(n) = nE_0^2 \left|\left\langle \Psi_f \mid \hat{\varepsilon}\vec{r} \mid \Psi_i \right\rangle\right|^2 \left|\mathrm{F}(T, \omega, \omega_{fi})\right|^2 \tag{20}$$

It is easy to observe that if $\eta = \frac{\pi}{\tau_0}$ the averaged transition probability may be written as

$$\overline{P}_{fi}(n) = nP_{fi}(1). \tag{21}$$

This means that if the energy resolution of the electron spectrometer satisfies the condition

$$\eta \geq \frac{2\pi}{\tau_0}, \tag{22}$$

in the measured spectrum of the ejected electron the resonance effects vanish due to the averaging effect of measurement.

If condition (22) is fulfilled, than in the theoretical study of transitions the laser pulses can be treated separately and the total transition probability

can be expressed as a sum of the transition probabilities calculated for individual pulses; otherwise, the study of the entire pulse train is necessary.

At present, electron spectrometers with energy resolution of $\approx 70\,\mathrm{meV}$ are available, which allow the observation of the obtained resonance effects only for laser pulses with a repetition rate higher than 40 THz.

The repetition rate of the available femtosecond laser pulses is in the range of few MHz, which is below the limit established above. In the case of photoionization for femtosecond pulses the resonance effects will be averaged out, so the treatment of the laser pulses separately is justified.

The repetition rate of the newly developed attosecond laser pulses [12, 13] is higher than the above established limit so in the attosecond laser pulses driven processes the shown resonance effects could have an important role.

Conclusion

Based on a simple perturbational approach the transition probability was deduced for ultrashort laser pulses, and a pulse shape independent resonance factor was identified.

Interesting beating like effect was observed when the pulse duration and the time between two pulses were close. This beating effect appears due to the sine-square envelope of the individual pulses and it is not a real effect.

Also was shown that the resonance effects can be observed experimentally only if condition (22) is not fulfilled, which leads to a limit for the repetition rate of the used pulse. The repetition rate of the available femtosecond lasers is below the established limit, so for femtosecond laser pulses the shown resonance effects are not significant and the treatment of the pulses separately is justified. Due to the recent development of the laser technology, train of attosecond pulses with high repetition rate are experimentally observed.

The repetition rate of these attosecond pulses is much higher than the limit established here based on the energy resolution of the electron spectrometers, so in attosecond laser pulse train driven processes the shown resonance effects have an important role.

REFERENCES

1. U. SAALMAN, CH. SCHIEDSCHLANG AND J. M. ROST, J. PHYS. B: AT. MOL. OPT. PHYS. 39 (2006) R39.
2. M. PROTOPAPAS, C. H. KEITEL, AND P. L. KNIGHT, REP. PROG. PHYS. 60 (1997) 389.
3. J. H. POSTHUMUS, REP. PROG. PHYS. 67 (2004) 623.
4. M. PONT, D. PROULX AND R. SHAKESHAFT, PHYS. REV. A 44 (1991) 4486.
5. E. CORMIER AND P. LAMBRAPOULOS, J. PHYS. B: AT. MOL. OPT. PHYS. 30 (1997) 77.
6. C. E. DATEO AND H. METIU, J. CHEM. PHYS. 95 (1991) 7392.
7. K. ANDRAE, P. G. REINHARD AND E. SURAUD, J. PHYS. B: AT. MOL. OPT. PHYS. 35 (2002) 4203.
8. G. DUCHATEAU, C. ILLESCAS, B. PONT, E. CORMIER AND R. GAYET, J. PHYS. B: AT. MOL. OPT. PHYS. 33 (2000) L571.
9. P. A. MACRI, J. E. MIRAGLIA AND M. S. GRAVIELLE, J. OPT. SOC. AM. B. 20 (2003) 1801.
10. R. GAYET, J. PHYS. B: AT. MOL. OPT. PHYS. 38 (2005) 3905.
11. D. MESCHULACH, D. YELIN AND Y. SILBERBERG, J. OPT. SOC. AM. B. 14 (1997) 2096.
12. P. A. PAUL, E. S. TOMA, P. BREGER, G. MULLOT, F. AUGE, PH. BALCOU, H. G. MULLER, P. AGOSTINI, SCIENCE 292 (2001) 1689.
13. Y. NABEKAWA, T. SCHIMIZU, T. OKINO, K. FURUSAWA, H HASEGAWA, K. YAMANOUCHI, K. MODORIKAWA, PHYS. REV. LETT. 96 (2006) 083901.

STUDIA UNIVERSITATIS BABEŞ-BOLYAI, PHYSICA, LI, 1, 2006

MAGNETORESISTIVITY AND HALL EFFECT OF $Ru_{1-X}Sb_XSr_2Sm_{1.5}Ce_{0.5}Cu_2O_{10-D}$

P. BALINT[1], M. BODEA[1], T. R. YANG[2], C. LUNG[1] AND G.ILONCA[1]

ABSTRACT. Magnetoresistivity and Hall effect on the samples of $Ru_{1-x}Sb_xSr_2Sm_{1.5}Ce_{0.5}Cu_2O_{10-d}$ were investigated in the temperature range 4-300 K with a magnetic field up to 9 Tesla .

Superconducting transition temperature decreases with increases content of Sb, due to a distortion of RuO_6 octahedral, which is responsible of the increase in hole localization, reflected by Hall concentration, too.

The inhomogeneous granular structure is shown by the intragranular, T_{co}, and intergranular ,T_{cg}, transition temperatures.

Hall effect anomalous decreases below $T_{magnetic}$ can be explained within a simple two-band model by a transition from localized to more itinerant behavior in the RuO_2 layer at $T_{magnetic}$.

1.Introduction

The discovery of the coexistence of magnetic order (FM) at T_M = 60-180 K and superconductivity (SC) below T_c = 30-50 K in the tetragonal rutheno-cuprate layered $RuSr_2LnCu_2O_8$ (Ru: 1212), $RuSr_2(Ln_{1-x}Ce_x)_2Cu_2O_{10-\delta}$ (Ru:1222) and, recently, $RuSr_2LnCe_2CuO_{12}$ (Ru:1232), (where Ln = Y, Gd, Eu, Sm, Dy, Ho, Er) [1-10] raises the question how these two antagonistic states of matter can accommodate with each other. The physical nature of superconducting and ferromagnetic states is far from being understood.

Both T_m and T_c (T_m>T_c) depend on oxygen concentration and sample preparation.

The superconducting state (SC) charge carriers originate from the CuO_2 planes and the hole doping of these planes, can be optimized with appropriate variation of the Ln/Ce ratio [11-14].

Both Ru-1212 and Ru-1222 phases are structurally related to the Cu-1212 ($CuBa_2YCu_2O_{7-d}$) phase with Cu in the charge reservoir replaced by Ru such that the Cu-O chain is replaced by a RuO_2 sheet. In the Ru-1222 structure furthermore, a three-layer fluorite-type block instead of a single oxygen-free Ln (=rare earth element) [14] layer is inserted between the two CuO_2 planes of the structure Cu-1212 structure. In both Ru-1222 replacement

[1] Babes-Bolyai University, Physics Faculty, Cluj-Napoca, Romania
[2] National Taiwan Normal University, Department of Physics, No. 88, Sec 4, Thingchou Rd. Taipei 117, Taiwan, ROC

of Cu in the charge-reservoir block by the higher-valent Ru increases the overall oxygen content.

The dc magnetic susceptibility studies exhibit two magnetic transitions at T_{2m} (around 80-90K) and at T_{1m} ($T_{2m}<T_{1m}$) (around 130-180K).

Detailed magnetization and Mossbauer study [12] have shown two magnetic components which has been also supported by the muon spin rotation results [13].

The magnetic ordering temperature T_m varies between 60K and 180K. Recently, it was observed that the coexistence of superconductivity and magnetism exists in simple compounds like $EuNbO_3$ [15]and in complex borides which do not have layered structure [16].

It is known that the Sb^{3+} substitution Ru^{5+} should charge the hole concentration in CuO_2 planes and might change the superconductivity and magnetic properties in Ru:1222 system.

In this report, Hall effect and magnetoresistivity of samples of $Ru_{1-x}Sb_x Sr_2Sm_{1.5}Ce_{0.5}Cu_2O_{10-d}$ (where x = 0.02-0.06), prepared by a solid-state reaction method, are presented.

2.Experimental

$Ru_{1-x}Sb_xSr_2Sm_{1.5}Ce_{0.5}Cu_2O_{10-d}$ (x = 0.0, 0.02, 0.04, 0.06) samples were synthesized by a solid-state reaction method. The stoechiometric quantities of high-purity powders of RuO_2, Sb_2O_3, $SrCO_3$, Sm_2O_3, CeO_2 and CuO were mixed and fired at 960 ºC in air for 12h. The mixture was ground and pressed into pellets before preliminary reaction at 1020 ºC for 20h. The resulting samples were reground, pelleted again, fired at 1060 ºC in flowing oxygen for 120h, annealed 15h at 845 ºC in pure oxygen at 75 atm and finally slowly cooled to room temperature. The X-ray powder diffraction patterns were taken using XD8 Advance Bruker AXS diffractometer using CuK_α radiation. The lattice parameters were refined by a least squares fitting procedure.The magnetoresistivity of the samples and Hall effect were measured using a standard probe method DC-technique, a bar shaped pieces with silver paint contacts, in the temperature range between 4.2K and 300K, in magnetic field up to 9T.

3.Results and discussions

The structural analysis of the samples were investigated by X-ray powder diffraction. The XRD patterns recorded at room temperature for $Ru_{1-x}Sb_xSr_2Sm_{1.5}Ce_{0.5}Cu_2O_{10-d}$ samples (where x = 0.0-0.06) reveal the presence of the main phase of Ru:1222.

The lattice parameters were calculated by a least-squares method using external standard (α-Al_2O_3 with a = 4.7588(1) Å, c = 12.993(2) Å). The results are presented in Table 1.

Table 1.
Structural parameters derived from x-ray powder diffraction data for $Ru_{1-x}Sb_xSr_2Sm_{1.5}Ce_{0.5}Cu_2O_{10-d}$

x	a(Å)	c(Å)	Volume(Å^3)
0	3.8361(2)	28.5232(1)	419.7378(0)
0.02	3.8345(3)	28.5385(3)	419.6127(0)
0.04	3.8342(1)	28.5340(0)	419.4808(9)
0.06	3.8420(0)	28.5282(4)	421.1037(3)

The Sb^{3+} ion substitutes for Ru in solid solution has a dramatic effect on the transport and magnetic properties which can be seen in previous works [7, 9, 17].

The temperature dependence of the resistivity ρ(T) for samples $Ru_{1-x}Sb_xSr_2Sm_{1.5}Ce_{0.5}Cu_2O_{10-d}$ (where x = 0.00, 0.02, 0.04, 0.06) are shown in Fig (1).

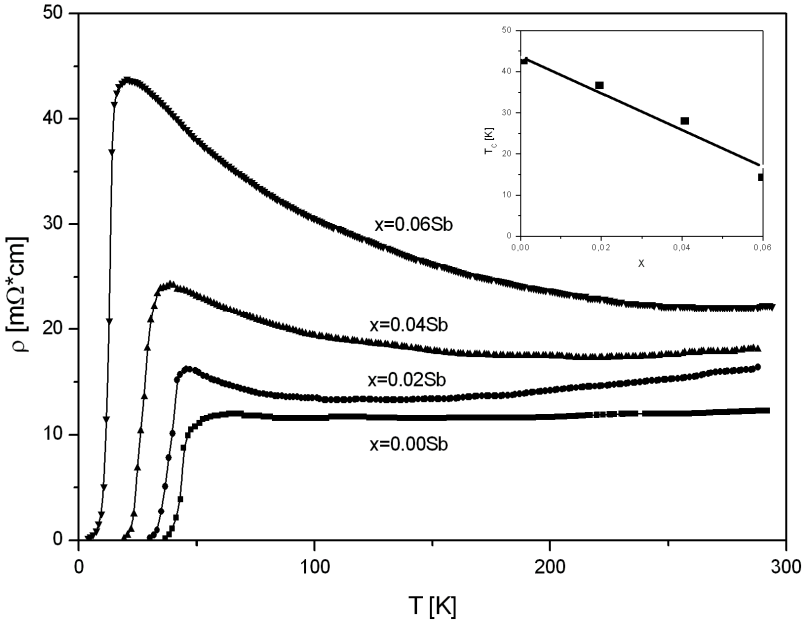

Figure 1. The temperature dependence of the resistivity for $Ru_{1-x}Sb_xSr_2Sm_{1.5}Ce_{0.5}Cu_2O_{10-d}$ samples with 0≤x≤0.06. Inset T_c versus content of Sb.

The superconducting transition is observed in all samples. The superconducting transition temperature $T_{c(onset)}$ decreases with increasing Sb content x and all samples are semiconductors-like above $T_{c(onset)}$.

The hole concentration in the CuO_2 plane decreases with Sb doping, in agreement with Ref. 18. The possible origin of this results is due to the distortion of RuO_6 octahedron in Ru:1212 that was proved through

neutron powder diffraction synchrotron experiments and X-ray diffraction experiments by Ref. [2] and [19]. The distortion of RuO_6 octahedron might lead to strong narrowing of the bands that results from the localization of carriers for Ru:1212 and Ru:1222 [2]. The Sb substitution for Ru increases the distortion of the RuO_6 octahedron and leads to more localization of carriers, so the transport behavior and the superconducting transition temperature decreases with the Sb substitution for Ru.

Temperature dependence of resistivity ρ(T) at different magnetic fields up to 9 T for samples with x = 0.00 Sb and x = 0.04 Sb annealed 15h at 845 ºC in pure oxygen at 75 atm and finally slowly cooled to room temperature are plotted in Fig. 2.

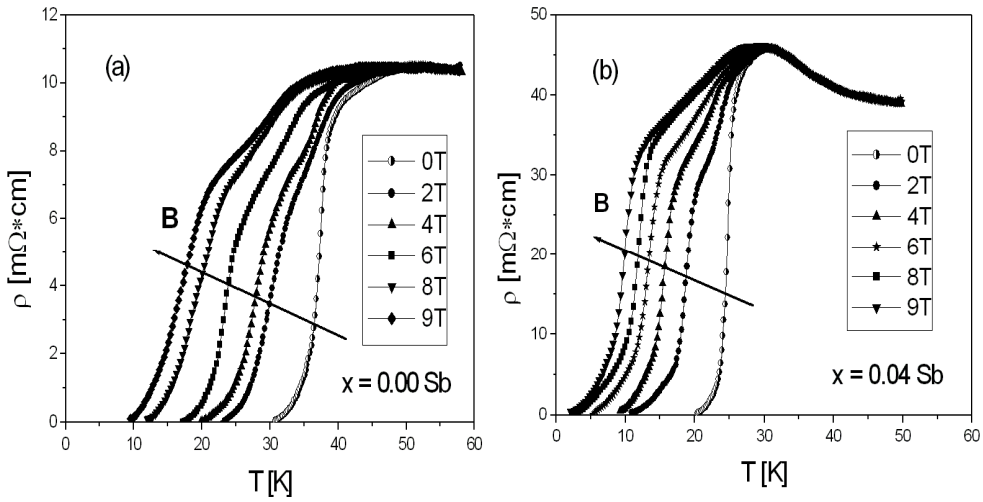

Figure 2. Temperature dependence of the resistivity at different magnetic field for $Ru_{1-x}Sb_xSr_2Sm_{1.5}Ce_{0.5}Cu_2O_{10-d}$ samples with x = 0.00 and x = 0.04.

The rather broad and shouldered ρ(T,B) curves in the region of the superconducting transition are indicative of inhomogeneity effects. The most inhomogeneity source is determined by the granular structure. Nonhomogeneous oxygen distribution can cause oxygen depletion of the grain boundary regions and a weak electrical connectivity between the grains, as it often happened in cuprates.

The onset temperature of superconductivity $T_{c(onset)}$ is about 45K with zero-resistance temperature about 30K for x = 0.00 Sb and 29K with 20K for x = 0.04 Sb. The shouldered ρ(T,B) curves in the region transition of the superconducting transition should be attributed to intragranular and intergranular superconducting transitions at temperatures T_{co} and T_{cg},

respectively. The intergranular superconductivity may be determined by Josephson coupling between the grains, in bulk cuprates.

Derivates dρ(T)/dT reveal two peaks in the region of the superconducting transitions, positions which can be attributed to intragranular and intergranular superconducting transition at temperatures T_{co} and T_{cg}, respectively. The magnetic field dependence of T_{co} and T_{cg} were shown in Figure 3 where it can be seen that T_{co} was reduced from 48K to 40K and T_{cg} from 45K to 27K for samples with x = 0.00 Sb and from 30K to 20K for T_{co} and from 25K to 10K for T_{cg} at the sample with x = 0.04 Sb.

The magnetic field has a weak influence on intragranular transition temperature T_{co}, but intergranular T_{cg} is more sensitive to magnetic field.

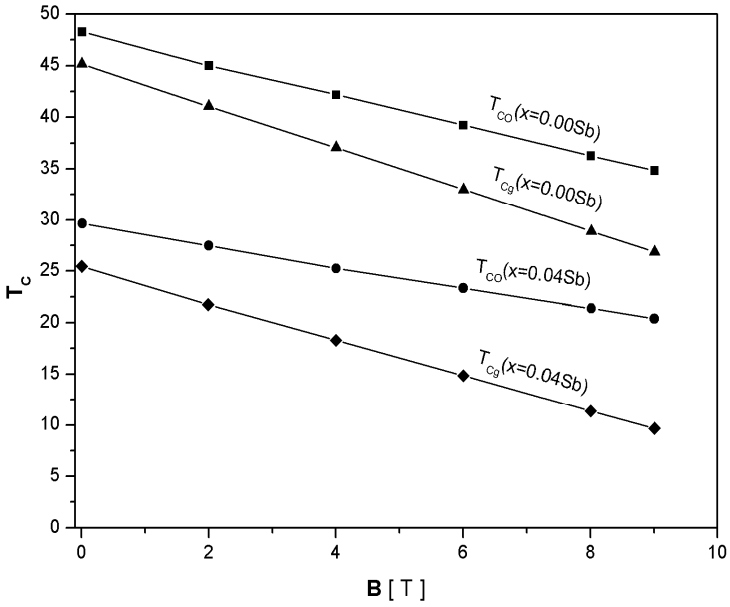

Figure 3. T_{co} and T_{cg} dependence of magnetic field for x = 0.00 Sb and x = 0.04 Sb.

The Sb substitution for Ru increases the distortion of RuO_6 octahedron and leads to more localization of carriers, so the transport behavior show typical semiconductor-like and the superconducting transition temperature decreases with increasing Sb substitution for Ru. This effect is confirmed by the Hall effect measurements which can be seen in Figure 4.

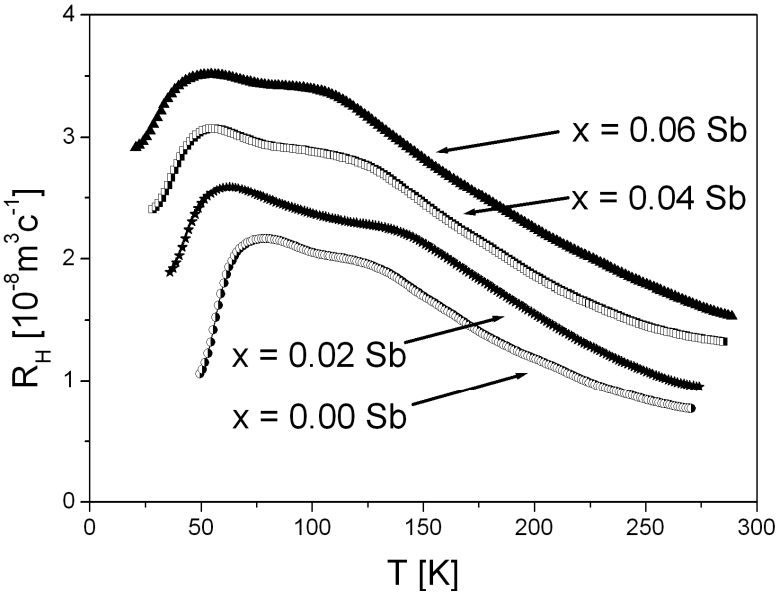

Figure 4. Temperature dependence of Hall coefficient for $Ru_{1-x}Sb_xSr_2Sm_{1.5}Ce_{0.5}Cu_2O_{10-d}$ samples with $0 \le x \le 0.06$

The holes concentration p_H extracted from R_H is $p_H = 1.24 \cdot 10^{27}/m^3$, the same value which has been obtained from thermopower measurements at room temperature for pure Ru:1222. This has been explained successfully using a simple two-band model [20]. The bands in this model are those formed by the carriers within Cu and Ru orbitals from CuO_2 and RuO_6 layers. Our data are in good agreement with this simple two-band model.

Conclusions

In summary, bulk single-phase specimens of superconductors Ru:1222 doped with Sb for Ru and Ce for Sm have been successfully synthesized . X-ray diffraction analysis has shown small differences of the lattice parameters with Sb contents.

The electrical resistivity ρ(T,B), in magnetic field up to 9 Tesla and Hall coefficient $R_H(T)$ were investigated on the same samples and all measurements data reveal a superconducting system typical of the HTS cuprates having the transition temperature and normal state transport properties consistent with granular doped cuprates.

The magnetic field has a weak influence on intragranular transition temperature T_{co}, but more sensitive to magnetic field is intergranular T_{cg}.

The Sb substitution for Ru in $Ru_{1-x}Sb_xSr_2Sm_{1.5}Ce_{0.5}Cu_2O_{10-d}$ systems reduces the T_{onset} from 43K for x = 0 at 21K for x = 0.06. This can

be due to a distortion of RuO_6 octahedron which is responsible of the increase in hole concentration.

Hall effect anomalous decreases below $T_{magnetic}$ can be explained within a simple two-band model by a transition from localized to more itinerant behavior in the RuO_2 layer at $T_{magnetic}$.

REFERENCES

1. I. Felner, U. Asaf, Y. Levi, O. Millo, *Phys. Rev. B* **55** (1997) R 3374;
2. L. Bauernfeind, W. Widder, H. F. Braun, *Physica C* **254** (1995) 151;
3. A. Ono, *Jpn. J. Appl. Phys*. **34** (1995) L 1121;
4. C. Bernhard, J. L. Tallon, Ch. Neidermayer, Th. Blasius, A. Golnik, E. Brucher, R. K. Kremer, D. R. Noakes, C.E. Stonach, E. J. Ansaldo, *Phys. Rev. B* **59** (1999) 14099;
5. J. D. Jorgensen, O. Chmaissen, H. Shaked, S. Short, P. W. Klamut, B. Dabrowski, J. L. Tallon, *Phys. Rev. B* **63** (2001) 054440;
6. B. L. Orentz, R. L. Meng, Y. Y. Xue, C. W. Chu, *Physica C* **383** (2003) 337 ;
7. G. Ilonca, S. Patapis, E. Macocian, F. Beiusan, T. Jurcut, G. Stiufiuc, R. Stiufiuc, *Int. J. Mod. Phys. B* **18, 15** (2004) 2177;
8. I. Felner, G. Kopnov, G. Koren, *Physica C* **432** (2005) 270;
9. T. R. Yang, G. Ilonca, F. Beiusan, A. V. Pop, V. Toma, I. Matei, S. Patapis, *Int. J. Mod. Phys. B* **19, 22** (2005) 3511;
10. V. P. S. Awana, H. Kishan, T. Kawshima, E. Takyama-Muromachi, C. A. Cardoso, *J. Appl. Phys.* **97** (2005) 10-B111;
11. I. Felner, I. Asaf, U. E. Galstyan, *Phys. Rev. B* **66** (2002) 024503;
12. I. Felner, E. Galstyan, I. Nowik, *Phys. Rev. B* **71** (2005) 064510;
13. A. Shengelaya, R. Khasanov, D. G. Eshchenko, I. Felner, U. Asaf, I. M. Savić, H. Keller, K. A. Müller, *Phys. Rev. B* **69** (2004) 024517;
14. V. P. S. Awana, E. Takayama-Muromachi, *Physica C* **390** (2003) 101; T. Kawashima, E. Takayama-Muromachi, *Physica C* **398** (2003) 85;
15. G. K. Shukova, D. V. Shovkun, U. N. Zverev, I. E. Batov, S. A. Zver'Kov, S. S. Khasanov, *Physica C* **351** (2001) 363;
16. S. L. Bud'Ko, P. C. Canfield, *Physica B* **280** (2000) 356;
17. G. Ilonca, T. R. Yang, F. Beiusan, A. V. Pop, I. Matei, E. Macocian, *Int. J. Mod. Phys. B* **17** (2003) 1-6;
18. L. Shi, G. Li, X. D. Zang, S. J. Feng, X. G. Li, *Physica C* **383** (2003) 450.
19. J. W. Lynn, B. Keimer, C. Ulrich, C. Berhard, J. L. Tallon*, Phys. Rev. B* **61** (2000) 14964;
20. J. E. McCrone, J. L. Tallon, J. R. Cooper, A. C. McLaughlin, J. P. Attfield, C. Bernhard, *Phys. Rev. B* **68** (2003) 064514.

STUDIA UNIVERSITATIS BABEŞ-BOLYAI, PHYSICA, LI, 1, 2006

SOME PROPERTIES OF THE NMR SPIN-SPIN RELAXATION OF THE POLYBUTADIENE-TOLUENE SOLUTIONS

C. V. POP[1], M. TODICA[1]*, S. ASTILEAN[1],

ABSTRACT. The NMR relaxation of the transverse magnetization of the protons attached to the polymeric chains was observed for the molten polybutadiene and for some polybutadiene-toluene solutions in a large temperature domain. The superposition properties of the relaxation curves, the linear temperature dependence of the experimental parameter $t_{0.6}(T)$, and the observation of the pseudo solid echoes, were correlated to the existence of the temporary junctions between the polymeric chains.

Keywords: NMR spin-spin relaxation; residual dipolar interaction; temporary junctions

Introduction

One of the most important propertie of the polymeric materials, the viscoelasticity, is determined by the temporary junctions between the polymeric chains, the entanglements, or by the permanent junctions of the cross-linked polymers [1, 2, 3]. The direct detection of the existence of these junctions is very difficult. However the observation of some microscopic properties of the dynamics of the plymeric chains can provide indirect information concerning these junctions.

NMR is one of the most utilised methods for the investigation of the molecular structure or the microscopic dynamics of the polymeric chains [4]. The characteristic time of the relaxation of the transverse magnetization can be corelated with the dynamics of the polymeric chains in the space and temporary scale corresponding to the temporary junctions. This time was mesured for samples with different solvent concentration in a large temperature domain. The temperature and concentration dependence of this parameter can suggest a correlation with the temperature dendence of the moduls of the elasticity.

The special pulse sequence called the pseudo-solid echo, applied in the same time scale of the characteristic time of the relaxation of the transverse magnetization, was used to evidentiate the existence of the dipolar residual interaction between the nuclear spins of the chain. This residual dipolar interaction is correlated to the existence of the entanglements of the

[1] "Babes-Bolyai" University, Faculty of Physics 400084 Cluj-Napoca, Romania
* corresponding author: email: tami@phys.ubbcluj.ro

polymeric chains. These two kinds of observations can be correlated with the viscoelastic properties of the polymers.

Experimental

We studded the molten polybutadiene PB with whit the microstructure 97% cis and the molecular mass Mn=110 000 g/mol, and some solutions of this polymer in toluene C_7D_8 with different concentrations: Φ=50%, Φ=60%,Φ=70%,Φ=80%, and Φ=88%. All the measurements were performed using a CXP Bruker spectrometer at the resonance frequency 45 MHz, in the temperature range 244-334 K. The relaxation of the transverse magnetization was measured by the standard Carr-Purcell sequence, [5, 6]. The sample temperatures were controlled within 1K.

Results and discussions

The viscoelastic behavior of the polymers is mainly determined by the entanglements between the polymeric chains. These temporary junctions induce some restrictions of the dynamics of the entire chain that affects the dipolar interaction between the nuclear spins attached to the polymeric chains. This interaction is the main mechanism, which governs the relaxation of the transverse magnetization of the nuclear spins [7, 8]. The characteristic time of the relaxation lie in the time domain of the fluctuations of the polymeric chain between the entanglements. For this reason it is interesting to observe some correlation between the characteristics parameters of the spin-spin relaxation process and the existence of the temporary network.

The relaxation curves of the transverse magnetization are complex and cannot be described by a single exponential function. However a partial

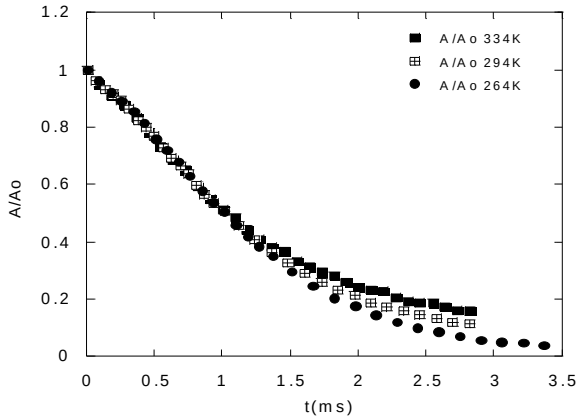

Fig. 1. The superposition property observed for the relaxation curves of the molten polymer.

superposition of the curves, obtained by a simple shift of the time scale with a constant factor, can be observed for all the samples in a large temperature domain (Fig.1). In the superposition domain we can assume that the relaxation of the transverse magnetization is governed by the same mechanism. We can introduce the experimental parameter $t_{0.6}$, designing the characteristic relaxation time corresponding to the decay of the transverse magnetization from its maximum value until 0.6 of its amplitude. This time is measured in the superposition domain of all the samples, and for this reason can be used as a descriptive parameter of the relaxation process. This parameter was measured for all the samples in a large temperature and solvent concentration domain.

For the molten polymer the superposition property is observed in the temperature domain 244-334K and the parameter $t_{0.6}$ presents linear temperature dependence (Fig. 2).

The superposition property of the relaxation curves was observed also for the polymeric solutions. The parameter $t_{0.6}$ (T) for these samples presents linear temperature dependence in a large temperature and concentration domains (Fig. 2). This behavior suggests a correlation between the linear variation of the parameter $t_{0.6}$ (T) and the superposition property of the

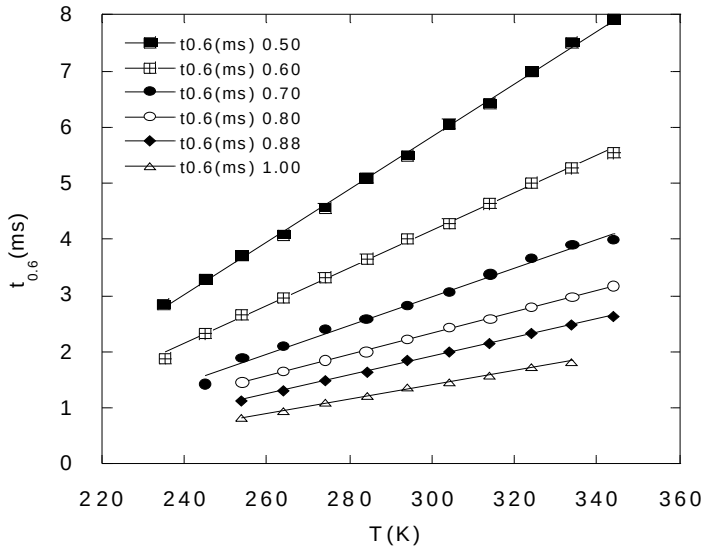

Fig. 2. The temperature dependence of the parameter $t_{0.6}$(T) for the molten polymer and for the polymeric solutions

relaxation curves. On the other hand it is known that the elasticity modulus G(T) of the ideal chains is characterized by linear temperature dependence. This common behavior of G(T) and $t_{0.6}$(T) suggest the possibility of some correlation between the two parameters and the possibility of characterizing the viscoelastic behavior by the NMR parameters. This supposition is sustained by the specific pseudo-solid behavior of the relaxation curves.

The fluctuations of the polymeric segments are the most important factor, which affects the dipolar interaction between the nuclear spins of the chain. For completely free nuclear spins, under the thermal agitation, this dipolar interaction is averaged to zero during the NMR observation, and the relaxation of the transverse magnetization is very long. This situation is characteristic for the majority of the simplest liquids. In the polymeric samples the nuclear spins attached to the chain are not completely free to move due to the chemical links along the chain and due to the entanglements between different polymeric chains. As the result the dipolar interaction is not completely averaged to zero during the NMR observation. More the rigidity of the chain is high, more the residual dipolar interaction is important. The existence of the residual dipolar interaction can be observed by a special pulse-sequence called the *pseudo-solid echoes* pulse sequence. The pulse sequence applied to the spin system is as follows:

$$\left(\frac{\pi}{2}\right)_{y} - \frac{\tau}{2} - (\pi)_{y} - \frac{\tau}{2} - \left(\frac{\pi}{2}\right)_{-x} - \frac{\tau_1}{2} - (\pi)_{y} - \frac{\tau_1}{2} - (\text{echo}) \qquad (1)$$

The description of the spin system behavior under this pulse sequence and the properties of the recorded echoes are very well presented in reference

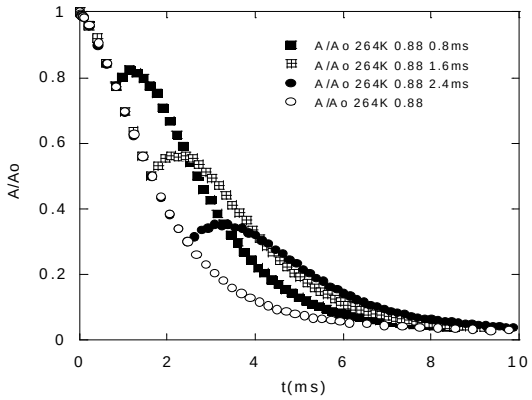

Fig. 3. The pseudo-solid echoes with characteristic properties observed for the polymeric solution PB 0.88 at 264K. The echoes were generated at different instants: τ=0.8ms, τ=1.6ms, and τ=2.4ms

[9]. The specific properties of the pseudo-solid echoes are characteristic for samples with important residual dipolar energy and can be correlated to the existence of the temporary network determined by the entanglements. When the dipolar interaction is strongly affected by the movement, these properties of the pseudo-solid echoes are not fulfilled.

For our samples we observed the pseudo-solid echoes with characteristic properties in the superposition domain of the relaxation curves (Fig.3). This fact indicates the existence of the temporary network determined by the entanglements between the polymeric chains. This domain corresponds also to the linear dependence of the parameter $t_{0.6}(T)$. Thus we can associate the linear dependence of the parameter $t_{0.6}(T)$ to the existence of the temporary network.

Conclusions

The fluctuations of the polymeric chain between the entanglements affect the relaxation of the transverse magnetization of the nuclear spin attached to the polymeric chains. The experimental parameter $t_{0.6}(T)$ can be used to characterize this relaxation process. This parameter presents linear temperature dependence in the superposition domain of the relaxation curves and can be associated with the existence of the temporary network.

The entanglements between the polymeric chains induce a non-zero average dipolar interaction that can be observed by the pseudo-solid echo sequence. The pseudo-solid echoes with specific properties were observed in the superposition domain of the relaxation curves and can be associated with the existence of the temporary network.

REFERENCES

1. W. W. Graessley, S. F. Edwards, Polymer, 22, 1329, (1981).
2. J. D. Ferry, Viscoelastic Properties of Polymers, Third. Ed., Wiley, New York, (1980).
3. P. G. De Gennes, Scaling Concepts in Polymer Physics, Cornell University Press, Ithaca, (1979).
1. 4. J. P. Cohen-Addad, NMR and Fractal Properties of Polymeric Liquids and Gels, Pergamon Press, London, (1992).
4. N. Bloembergen, E. M. Purcell, and R.V. Pound, Phys. Rev, 73, 679, (1948).
5. H. Y.Carr and E. M. Prcell, Phys. Rev., 94, 630, (1954).
6. A. Abragam, The Principles of Nuclear Magnetism, Clarendon Press, Oxford, (1961).
7. I. Ya. Slonim, A. N. Lyubimov, The NMR of Polymers, Plenum Press, New York, (1970).
8. J. P. Cohen-Addad, Carlo Schmit, Polymer, 29, 883-893, (1988).

STUDIA UNIVERSITATIS BABEŞ-BOLYAI, PHYSICA, LI, 1, 2006

INFRARED SPECTRUM CALCULATIONS FOR SMALL WATER CLUSTERS

TITUS A. BEU* **AND ANA-MARIA FLORESCU**

ABSTRACT. We report calculated infrared spectra for water clusters composed of up to twenty molecules, using a formalism based on second order perturbation theory. We have investigated the frequency domain between 3000 and 4000cm^{-1}, which includes the symmetric and asymmetric bond stretching modes and the overtone of the angle bending mode. The stretch modes are found to be redshifted, while the bending mode is blueshifted.

1. Introduction

Water is one of the most intensively studied substances, due to its special properties, many of them being related to the presence of hydrogen bonds. One of the most sensitive methods of probing the hydrogen bond network is vibrational spectroscopy. The spectral lines appear to be either redshifted (the stretch modes) or blueshifted (the bending mode) in comparison with those of the monomer. We have studied the frequency interval between 3000 and 4000 cm^{-1}, comprising the symmetric and asymmetric stretch modes and the first overtone of the angle bending mode (all three modes being non-degenerate). There are only few experimental studies of water cluster spectra in this frequency range, among which the most accurate are those published by Buck et al. 1-4 and Huisken et al. 5. Other experiments were carried out using less effective size-selection techniques. For example, Huang and Miller 6 have measured spectra only for the dimer, while Cocker et al. 7 have reported spectra for larger clusters, however with no size selection.

2. Theoretical methods

We have employed the minimal energy structures of the clusters calculated previously using a deterministic-stochastic method and two well known potential models(TIP4P 10 and TIP5P 11) and we have calculated the infrared spectra using a quantum mechanics formalism based on second order perturbation theory 8,9.

This formalism 8,9,12 is based on the idea of treating the anharmonic contributions to the intramolecular force field and the intermolecular potential

* University "Babeş-Bolyai", Faculty of Physics M. Kogălniceanu 1, RO-3400 Cluj-Napoca, Romania
E-mail: tbeu@phys.ubbcluj.ro

as perturbation of the molecular vibration, described in the normal mode approach. This formalism was successfully applied to several systems until now.1314.

For a homogeneous cluster formed of n molecules, the first order frequency shifts $\Delta\nu_{mi}^{(1)}$ relative to a particular vibrational mode m of the monomer i have been shown to result from the eigenvalue problem

$$\sum_{m'\in\Gamma}\sum_{i'=1}^{n}\left(\frac{\partial^2 U}{2\partial q_{mi}\partial q_{m'i'}}-hc\Delta\nu_{mi}^{(1)}\delta_{mm'},\delta_{ii'}\right)c_{m'i',mi} \quad = \quad 0, \quad i=1,2,...,n. \tag{1}$$

The second order line shifts can be explicitly expressed as:

$$\Delta\nu_{mi}^{(2)} = \sum_{m',m''\in\Gamma}\sum_{i',i''}c_{m'i',mi}c_{m''i'',mi}^{*}\Delta\nu_{m'i',m''i''}^{(2)}, \tag{2}$$

where the coefficients $c_{m'i',mi}$ are components of the eigenvectors yielded by the eigenvalue problem (1), and the partial contributions $\Delta\nu_{m'i',m''i''}^{(2)}$ are given by:

$$\begin{aligned}\Delta\nu_{m'i',m''i''}^{(2)} &= -\frac{\delta_{i'i''}}{2hc}\sum_{r}\frac{1}{\omega_r}\frac{\partial U}{\partial q_{ri'}}\phi_{m'm''r} \\ &+\frac{1}{4(hc)^2}\sum_{r\notin\Gamma}\sum_{j}\frac{1}{\omega_m-\omega_r}\frac{\partial^2 U}{\partial q_{m'i'}\partial q_{rj}}\frac{\partial^2 U}{\partial q_{m''i''}\partial q_{rj}} \\ &-\frac{1}{4(hc)^2}\sum_{r}\sum_{j}\frac{1}{\omega_m+\omega_r}\frac{\partial^2 U}{\partial q_{m'i'}\partial q_{rj}}\frac{\partial^2 U}{\partial q_{m''i''}\partial q_{rj}}.\end{aligned} \tag{3}$$

Here ω_m and $\phi_{m'm''r}$ are harmonic frequencies and cubic force constants, respectively. The most significant second order contributions are generally due to the first term, coupling the generalized intermolecular forces $-\partial U/\partial q_{ri'}$ with the cubic intramolecular force constants $\phi_{m'm''r}$.

In the first step in our approach, the normal mode analysis of the water monomer is performed using the G-F method of Wilson 15. In the second step, the transformation of the intramolecular force field from valence to normal coordinates is accomplished by the L-tensor formalism of Hoy, Mills and Strey 16, yielding anharmonic monomer frequencies and transformed cubic force constants $\phi_{m'm''r}$.

The IR frequencies are obtained by adding the first and second order frequency shifts to the experimental monomer frequencies corresponding to each normal mode. The second order frequency shifts couple the considered normal mode with the closest overtones, thus accounting also for the Fermi resonances. The line spectrum for a given cluster size was averaged over a Boltzmann ensemble of computed cluster configurations, averaged at 150K, consistent with experimental measurements.

3. Results and discussion

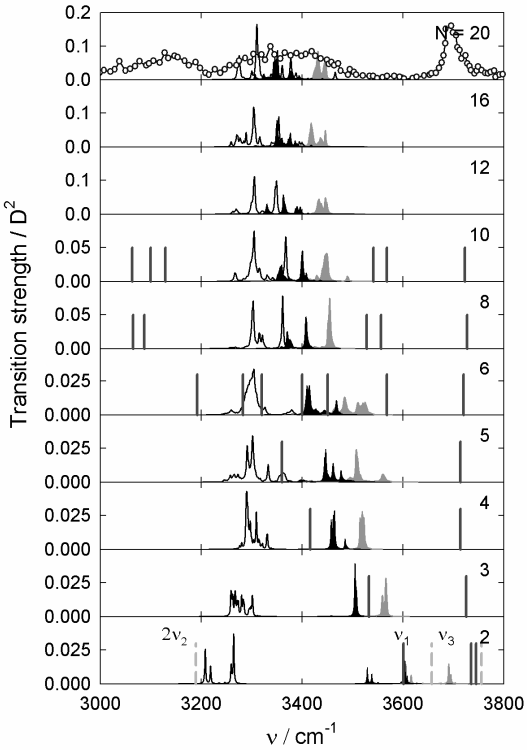

Figure 1. IR spectra for $(H_2O)_n$ clusters. The dotted drop-lines in the lower panel represent the monomer frequencies, while the solid drop lines are the experimental frequencies of Huisken et al. 5 (up to the pentamer). The data for liquid water reported by Buck et al. 3 was depicted in the upper panel.

The equilibrium structures of the water clusters ($n = 2-20$) have been determined by stochastic minimization of the total interaction energy, considering the clusters as being composed of rigid monomers. The methodology and results are presented in our previous paper.

We have carried out the frequency shift calculations using both potential models under consideration (TIP4P and TIP5P). In order to better describe the vibrational modes, we have used the atomic displacements provided by the normal-mode analysis of the monomer. For the motion of the supplementary sites adopted a prescription according to which they move together with the oxygen atoms.

The TIP4P model renders more realistic values mainly because the supplementary site is positioned closer to the hydrogen atoms and the charges oscillate less, rendering more realistic variations of the dipole moment. The TIP5P model leads to an underestimation of the frequency shifts which can be accounted by the fact that in this model the charges are overspread. Also the TIP4P model is known to more accurately reproduce the dipole moment of water 10,11. However, for both potential models the frequency shifts show the same general tendencies, and further on only the results for TIP4P will be presented.

Figure 1 shows ensemble-averaged IR-spectra for the considered H_2O clusters obtained by applying the approach described above to the symmetric stretch mode ν_1, the asymmetric stretch mode ν_3, and the overtone $2\nu_2$ of the symmetric bending mode. While the two OH-stretch modes present a red shift that was expected, the overtone of the asymmetric bending vibration shows a pronounced blue shift. The shifts are due to the presence of the hydrogen bonds in the cluster.

The asymmetric stretch mode ν_3 exhibits the largest frequency shifts. This can be explained by the presence of hydrogen bonds that hinder the OH-stretch vibration. The symmetric stretch lines (ν_1) are the least intense, and are also less shifted that the asymmetric stretch lines. The lines corresponding to the bending mode overtone are the most intense of the spectra and also the least shifted, the bending mode being less perturbed by the presence of the other molecules in the cluster. The line shifts increase with cluster size, but for larger clusters the shifts tend to saturate, the spectrum appearing rather like a broad band than separate lines, in agreement with the liquid-state bands.

Our infrared spectra are compared with the experimental results for size-selected water clusters obtained by Huisken et al. ($n = 2-5$) 5 and Buck et al. ($n = 6-10$) 1-4. For clusters larger than the decamer there is no accurate size-selective study in literature. For the dimer and trimer our results are in good agreement with the experiments. For the tetramer and the pentamer the experimental lines assigned to the stretch modes are strongly redshifted to values that correspond rather to the bending mode overtone predicted by our calculations.

For the hexamer all our spectral lines have experimental counterparts. For larger clusters the results are not very reliable because they are at the limit of the size-selection technique and the measurement of cluster size is not very accurate.

4. Conclusions

We have computed infrared line shifts for water clusters formed of up to 20 molecules using two site-site intermolecular potentials(TIP4P and TIP5P).The best results were obtained for the TIP4P model, the TIP5P model rendering underestimated shifts, probably because the charges are overspread. The line shifts appear to increase with cluster size, tending to saturate for larger clusters. The largest shifts appear for the asymmetric stretch mode, while the bending mode overtone seems to be the least affected by the intermolecular force field.

The authors gratefully acknowledge a CEEX and a CNCSIS grant from the Romanian Ministry of Education and Research.

REFERENCES

1. U. Buck, I. Ettischer, M.Melzer, V. Buch and J. Sadlej, Phys. Rev. Lett. **80**, 2578 (1998).
2. J. Brudermann, M. Melzer, U. Buck, J. Kazimirski, U. Buck, J. Chem. Phys, **110**, 10649(1999).
3. U. Buck, F. Husiken, Chem. Rev. **100**, 3863 (2004).
4. C. Steinbach, P. Andresson, M. Melzer, J.K. Kazimirski, U. Buck, V. Buch, Phys. Chem. Chem. Phys. **6**, 3320 (2004).
5. F. Huisken, M. Kaloudis, A. Kulcke, J. Chem. Phys. **104**, 1 (1996).
6. Z.S. Huang, R. E. Miller, J. Chem. Phys. **91**, 6613 (1989).
7. D. F. Cocker, R. E. Miller, R.O. Watts, J. Chem. Phys. **82**, 3554 (1985).
8. T.Beu , Z.Phys: At., Mol. Clusters **31**, 95 (1995).
9. T. A. Beu and K. Takeuchi, J. Chem. Phys. **103**, 6394 (1995).
10. M.W. Mahoney and W.L. Jorgensen, J. Chem. Phys. **112**, 20 (2000).
11. W.L. Jorgensen, J.Chandrasekhar, J.D. Madura, R.W. Impey,M.L. Klein J. Chem. Phys. **79**, 2 (1983).
12. U. Buck and B. Schmidt, J. Chem. Phys. **98**, 9410 (1993).
13. T. A. Beu and U. Buck, J. Chem. Phys. **114**, 7853 (2001).
14. T. A. Beu and U. Buck, J. Chem. Phys. **114**, 7848 (2001).
15. E. B. Wilson, J. C. Decius, and P.C. Cross, Molecular Vibrations (McGraw-Hill, New York, 1955).
16. A.R. Hoy, I. M. Mills, and G. Strey, Mol. Phys. **24**, 1965, (1972).

STUDIA UNIVERSITATIS BABEŞ-BOLYAI, PHYSICA, LI, 1, 2006

ISING-TYPE SPIN MODEL FOR BARKHAUSEN NOISE AND MAGNETIZATION PHENOMENA

KATALIN KOVÁCS*

ABSTRACT. A 1D Ising-type model aimed to reproduce megnetization phenomena is presented and studied by Monte-Carlo simulations. Disorder is introduced in the model through pinning centers which act as potential barriers on the ferromagnetic domain boundaries. The model captures and reproduces the accepted properties of domain-wall dynamics. Simulation results indicate that the model is able to reproduce the main characteristics of hysteresis and Barkhausen noise statistics. Jump size distribution, power spectrum, signal area- and duration distribution show scaling behavior in the critical regime, in agreement with the experimental data.

Keywords. Barkhausen noise, Monte-Carlo simulation, scaling behavior
PACS: 75.10.Hk, 75.60.-d, 05.10.-a

1. Introduction

The study of disordered media is a fascinating research field of the modern statistical physics. Much attention has been paid in the last decades to the experimental and theoretical investigation of disordered magnetic systems and study of the related magnetic Barkhausen noise (BN). For a detailed review see Ref [1].

BN belongs to the family of the so-called crackling noises [2]. It appears as a series of discrete and abrupt jumps in the magnetization whenever a ferromagnetic sample is placed under varying external magnetic field. In standard ferromagnets where magnetization is driven by the motion of domain walls, it is believed that the BN is a consequence of the fast movement of domain walls between pinning centers, which are either defects or impurities.

The Barkhausen phenomenon is interesting and worth to study from several points of view. A practical reason is that by measuring the BN there is a possibility for non-destructive and non-invasive material testing and control. On the other hand, there is a conceptual viewpoint: by studying the BN one might reach a better understanding of the complex dynamics of domain walls during magnetization processes in the presence of pinning centers opposing to the motion of magnetic walls. It is also a clear example for the dynamics of a system presenting collective pinning when a quenched disorder is present.

* Department of Physics, Babeş-Bolyai University, str. Kogălniceanu 1, RO-400084 Cluj-Napoca, Romania E-mail:kkovacs@phys.ubbcluj.ro

Since its discovery (1917) BN has been intensively studied [3]. Numerous measurements were done to clarify the statistical properties of the BN [3-5]. Regarding the nature of the Barkhausen noise (white noise, $1/f$ noise, or $1/f^2$ noise) a variety of conflicting statements can be found in the experimental literature. Measurements performed with different devices on different materials yielded qualitatively similar, but quantitatively very different results. The qualitative agreement in the experimental results consist in the finding that the distribution functions describing the statistics of BN follow power-law for a wide range of parameters and materials. The most relevant measured quantity is the avalanche size distribution, but many results have been reported concerning the power spectrum, signal area-, signal energy-, signal duration distribution. Numerical results for scaling exponents depend strongly on the experimental technique and on the characteristic features of the material itself.

Many conceptually different models were elaborated to explain BN and its scaling properties. Without the intention of making a complete review, here we will mention only a few selected theoretical approaches.

Models aimed to explain magnetization phenomena and domain wall dynamics can be classified basically into two categories. A first group of models consider the dynamics of single or multiple domain walls in a spatially rough coercive field created by the defects [6-10].

The second class of models is based on the Ising model. These models consider an Ising-type spin system on a lattice. The differences between these models come from the way how they implement the effect of the disorder on the spin system. These are the random field (RFIM) [11,12], random bond (RBIM) [4], random anisotropy (RAIM) [5] Ising models.

In this paper we present a new Ising-type model aimed to reproduce at least qualitatively the real magnetization phenomena and the expected statistical properties of the magnetic Barkhausen noise.

In Ref [6] we presented another magnetization model which is a 1D Burridge-Knopoff [7] type spring-block model. It is based on a simple mechanical analogy and it is able to explain successfully the basic phenomena related to the magnetization of ferromagnetic materials and gives qualitatively good results for the statistical properties of the BN: shape of the hysteresis loops, avalanche size distribution, power spectrum, signal area distribution. Despite its advantages and qualities, the spring-block model has several serious drawbacks. First, it operates with forces instead of a well defined Hamiltonian. Second, the number of domain walls separating oppositely oriented magnetic domains is a-priori fixed. This constraint is artificially imposed in the model, but it is not realistic. In the case of ferromagnets domains can appear and disappear during the magnetization-demagnetization

cycles. The new model which is to be presented here is designed in a way to overcome and eliminate both deficiencies of the previous model.

2. The Spin Model with Random Pinning Centers

The ferromagnetic system is modeled by a one dimensional spin chain on mesoscopic level. Spins (that represent mesoscopic parts of a magnetic domain) may have two states: up ($s = +1$) or down ($s = -1$) oriented. Ferromagnetic domain structure is taken into account in the following simple way: neighboring spins with the same orientation are members of one magnetic domain. Between two oppositely oriented spins is considered to be a 180 degree Bloch-wall that separates two domains. Wherever in the model system there are inversely oriented neighboring spins, they will automatically belong to different domains and between them is considered to be a Bloch-wall.

Defects and impurities that are present in the crystalline structure of real magnetic systems in this model are taken into account through the presence of pinning centers. The pinning centers act as potential barriers which block the free movement of the Bloch-walls until the wall acquires the needed amount of energy to jump over the barrier.

2.1. Hamiltonian

the model system built up in this way we introduce basic interactions that usually take place in ferromagnetic systems: Ising-type exchange interaction, pinning interaction, interaction with the external driving magnetic field, magnetic self-energy.

The model and the interactions are all enclosed in a Hamiltonian:

$$\begin{aligned} H &= -J\sum_{i=1}^{N_S} S_i S_{i+1} + \sum_{i=1}^{N_S} \left(S_i S_{i+1} - 1\right) T_i - B\sum_{i=1}^{N_S} S_i + \\ &+ K([\sum_{i=1}^{N_S}\sum_{j=i}^{N_S}\prod_{k=i}^{j}(\frac{1+S_i S_k}{2})] - \frac{N_s}{2}) \end{aligned} \tag{1}$$

The four terms in the Hamiltonian include all the interactions that are supposed to govern the dynamics of a domain wall. The first term represents the Ising-type exchange interaction between neighboring spins with $J > 0$ (ferromagnetic system) coupling constant. According to this term an energetically favorable situation is when all spins have the same orientation. Thus, this term drives the system toward a single-domain state. We define the units in such a way that $J = 1$. The second term contains the effects of the pinning centers, where $T_i > 0$ are the strengths of the pinning centers. These follow Gaussian distribution, the standard deviation of the distribution (σ) is called disorder. This term acts in a way that it decreases the total energy only if

neighboring spins have inverse orientation. When two neighboring spins have the same orientation the pinning term vanishes. In this way the Hamiltonian contains the very important fact that pinning centers act only on domain walls by blocking their free movement. The pinning term drives the system toward the many-domains state. The third term in the Hamiltonian contains the interaction with the external driving magnetic field (B). It is energetically favorable when spins have the same orientation with the external field. The last term in the Hamiltonian represents the magnetic self-energy of each domain, with a $K > 0$ constant. This energy is proportional with $M_j{}^2$, where M_j is the magnetization of domain j. In this model we define the magnetization of a domain to be proportional with its length, e.g. with the number of spins in a certain domain. This term acts in the direction to create as many (and consequently as short) domains as possible. Each domain has a positive contribution to the total energy. This contribution is proportional with the length of the domain.

Let us see in more detail what does the last term in the Hamiltonian mean. Take the first spin and check which is the first opposite oriented spin in the array. At this point the next domain begins. Let the length of the j th domain (i.e. the number of spins in the domain) be l_j. This domain contributes to the total Hamiltonian with a self-energy proportional with $\frac{l_j^2}{2}$. Indeed, according to the self-energy term the j th domain contributes with $(1+2+...+l_j)-\frac{l_j}{2}=\frac{l_j^2}{2}$. The product in this term actually detects the end of a domain by becoming zero whenever it meets the first time an opposite oriented spin. This way the domains can be also counted. Let the number of domains be n, then the self-energy term reads as follows:

$$E_{self} = K\sum_{j=1}^{n}\frac{l_j^2}{2} \tag{2}$$

The Hamiltonian (1) contains two fundamental differences from the standard Ising-type Hamiltonians of magnetization models. The RFIM Hamiltonian has the form:

$$\mathcal{H} = -J\sum_{ij} s_i s_j - \sum_i (H(t)+h_i)s_i \tag{3}$$

This Hamiltonian contains the exchange interaction, the interaction with the external field and contains a random field at each site. We consider it non-realistic

to let a pinning center act on every single spin in the system. Experiments suggest that pinning centers become important only on domain boundaries where they block the free movement of the walls. In our model the pinning effect is taken into account in a more realistic way. The Hamiltonian (3) does not account for the domains' magnetic self-energy. This deficiency is also solved in our model because in the Hamiltonian (1) the last term is the magnetic self energy.

2.2. Dynamics

The model is aimed to reproduce real magnetization phenomena in a simple way. Its dynamics is governed by the tendency to reach the minimum energy state (called equilibrium) under certain parameter values and externally imposed conditions. It is a one-spin dynamics, and goes through the following steps:

First an initial random configuration of the spins is generated. The size of the system is given by the N_s number of spins. The external magnetic field has zero intensity yet. The initial value of the Hamiltonian is computed. One spin is flipped. This has to be the spin that causes the greatest energy-decrease. We continue this way flipping one spin until the Hamiltonian cannot be decreased further with this one-spin method. This state is called equilibrium.

Once the initial equilibrium is reached we start to simulate the magnetization phenomena. We increase the intensity of the external magnetic field with small dB steps. The new value of the Hamiltonian is computed, equilibrium state is found with the one-spin dynamics. This is taken to be one simulation step. We repeat this procedure until the sample under study is saturated. Demagnetization process begins: the external magnetic field is decreased step by step until opposite oriented saturation. The model system is driven through one or more complete hysteresis loops.

The magnetization is performed at a slow rate, so that at each step equilibrium is reached. Under the assumption of a quasistatic process, when the applied external magnetic field B is changed at a low constant rate, all the derivatives with respect to time are proportional with derivatives with respect to B. Throughout this paper all time derivatives will be replaced by derivatives with respect to B.

From the dynamics sketched above it results that the number of Bloch-walls and magnetic domains is not a-priori fixed. The number of walls in the system is determined solely by the minimum energy criterion under given parameters and externally imposed conditions.

During the simulation we keep evidence of the variation of the magnetization and we study the shape of the hysteresis loops, the corresponding jump size distribution, signal area- and duration distribution, power spectrum for different system sizes. Our aim is to investigate whether the model reproduces the expected statistical properties of the BN.

The hysteresis loop shows the relation between the external driving magnetic field (B) and the magnetization (M) when the system is driven through successive magnetization and demagnetization processes.

Barkhausen jump size distribution ($g(s)$) is the distribution function of the sizes of discrete magnetization jumps throughout many hysteresis cycles. Experimentally Barkhausen signal is given by $\frac{dM}{dt}$. Taking into account the substitution presented in the above paragraph, in our model Barkhausen jumps are defined like $\frac{dM}{dB}$. Thus the simulated jump sizes are not absolute values because they might depend on the external magnetic field driving rate. All our simulations were made with one well defined driving rate, namely: $dB = 10^{-4}$. This rate is low enough to correspond for quasistatic driving.

Signal duration ($g(d)$) and signal area ($g(A)$) distribution functions (histograms) were also studied. In terms of this spin model signal duration is defined as the number of consecutive dB steps (= simulation steps) when Barkhausen jumps occur (the length of a $\Delta M/dB \neq 0$ sequence). Signal area measures the area under the nonzero $\Delta M/dB$ sequence versus B.

2.3. Effect of the free parameters

The free parameters of the model are: N_s - number of spins, dB - driving rate, K - demagnetization constant. The low number of free parameters makes simulation easier, and the effect of each parameter can be clearly understood.

A simple test can reveal the role of parameters and in the same time checks whether the Hamiltonian describes the interactions in a proper way and the dynamics is correct.

In the absence of pinning terms and external field the Hamiltonian (1) simplifies to

$$H = -J\sum_{i=1}^{N_S} S_i S_{i+1} + K([\sum_{i=1}^{N_S}\sum_{j=i}^{N_S}\prod_{k=i}^{j}(\frac{1+S_i S_k}{2})] - \frac{N_s}{2}) \qquad (4)$$

Theoretically one would expect that the system will reach an equilibrium number of domains of equal size, so that the magnetization of the sample under study will be zero. The system governed by the simplified Hamiltonian (4) has reached the equilibrium domain number n_e when

$$\frac{dH}{dn} = 0 \qquad (5)$$

In equilibrium all domains have equal length, $l_e = \frac{N_s}{n_e}$, and $\sum_{j=1}^{n} l_j = N_s$ holds always where l_j is the length of j th domain. The self-energy term from (2) takes the form

$$E_{self} = K \frac{N_s^2}{2n} \tag{6}$$

Given n domains the Ising-type exchange interaction can be written as

$$E_{ex} = -J(N_s - 1 - 2n) \tag{7}$$

The Hamiltonian (4) is now written in the form

$$H = -J(N_s - 1 - 2n) + K \frac{N_s^2}{2n} \tag{8}$$

Calculating the equilibrium domain number with relation (5):

$$n_e = \frac{N_s}{2} \sqrt{\frac{K}{J}} \tag{9}$$

For example: if $N_s = 2000$, $K = 10^{-4}$, $J = 1$ then $n_e = 10$. Our simulation code reproduces this result correctly.

Parameter N_s defines the size of the model system, and consequently the equilibrium domain number for a given K value in the absence of external driving magnetic field and pinning effect. From relation (9) one can read that increasing the system size will linearly increase the equilibrium number of domains, but the average length of a domain will remain unchanged. This observation is very important, since it allows us to vary N_s without rescaling parameter K.

Parameter K measures the significance of the magnetic self-energy of the domains, it acts as a demagnetizing factor. The greater K is the larger the equilibrium domain number is. This parameter also influences the width of the hysteresis loop. Increasing K the hysteresis loops become narrow. In the absence of pinning centers for $K = 0.01$ the hysteresis vanishes.

Parameter dB is the driving field rate, defines the step by which the external magnetic field is changed after one simulation step. Since we deal with a quasistatic dynamics, it is recommended to change external magnetic field intensity with very small steps. We have found that best results are obtained with $dB = 10^{-4}$.

The ferromagnetic coupling (first) term in the Hamiltonian (1) and the external field (third term) act in the direction to create a single-domain state. By the other hand, disorder (second term) together with the magnetic self-energy of the domains (last term) favorize the multi-domain state. This means that exchange with external driving and disorder with self-energy compete. During the simulations we have fixed the coupling constant $J = 1$, and all the quantities are defined according to this convention. Almost all models use this convention, except the random bond Ising model, where the coupling strengths contain actually the randomness, but even though their mean is set to be -1.

Taking into account the above considerations regarding the free parameters of the system, simulation results are presented with following parameter values: $N_s = 3000$, 5000 and 10000, $K = 10^{-3}$, $dB = 10^{-4}$.

3. Simulation Results

Characteristic **hysteresis loops** are plotted on Fig. 1. The shape of the curves fulfills the requirements for the real magnetization phenomena. Many discrete jumps with different sizes are detectable. This means that the model exhibits Barkhausen noise. The hysteresis loops plotted on Fig. 1. are obtained by driving the model sample through more consecutive complete magnetization--demagnetization cycles while all the simulation parameters were unchanged. One can clearly observe (see inner graph on Fig.1.) that the magnetization does not follow the same path during successive cycles. This fact proves that this model can reproduce the irreversible character of the magnetization--demagnetization process.

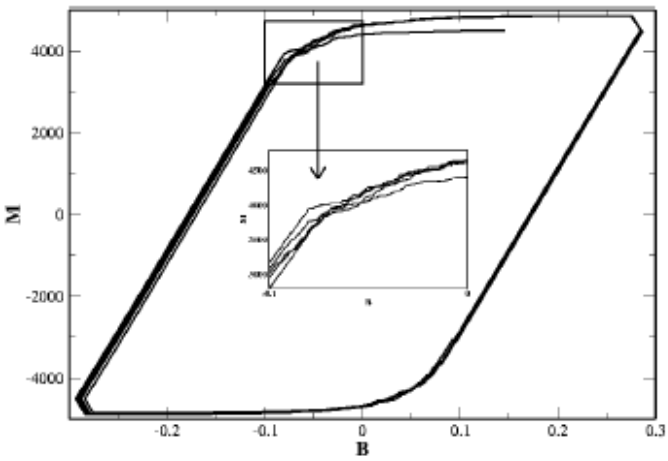

Figure 1. Hysteresis loops. Parameters: $N_s = 5000$, $K = 10^{-3}$, $dB = 10^{-4}$, 5 successive loops. Inner graph shows in detail the indicated region

A typical **power spectrum** in terms of $1/dB$-type frequency is plotted on Fig. 2. Statistics was performed on 1000 configurations. One configuration corresponds to one certain initial random spin- and pinning center arrangement. Compared to experiments every configuration means different ferromagnetic sample (identical sized) with different pinning center distribution. The spectrum shows that our model exhibits $1/f$ -type Barkhausen noise with -0.91 exponent through three decades of data. Power spectrum was computed and averaged over data collected from whole hysteresis loops. Here we emphasize again that in our model the frequency is in terms of $1/dB$. This substitution is allowed because all the simulations were made in the adiabatic limit where the driving rate of the external magnetic field is constant and in every simulation step equilibrium state is reached.

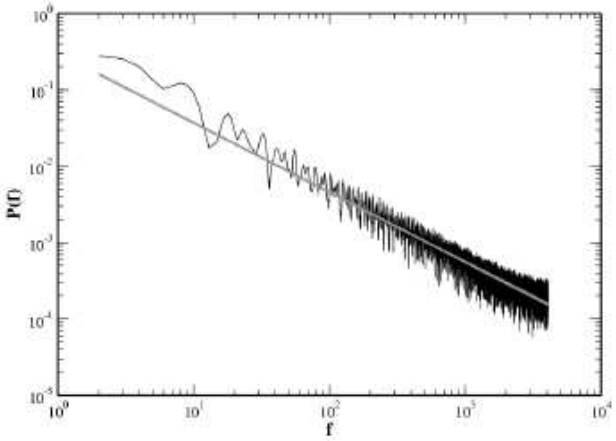

Figure 2. Power spectrum for the simulated BN (black curve). FFT performed on 2^{13} data, statistics on 1000 configurations, with $N_s = 10000$, $K = 10^{-3}$, $dB = 10^{-4}$. Data fitted with power-function, exponent -0.91 (gray solid line)

All the distribution functions we have computed for the statistics of the Barkhausen noise are normalized and defined as

$$g(y) = \frac{N(y, y+dy)}{N_t \cdot dy}, \tag{10}$$

where N_t denotes the total number of occurrences, $N(y, y+dy)$ is the number of occurrences with sizes between y and $y+dy$, y is the quantity under focus which can be jump size (s), signal duration (d) or signal area (A).

Statistics over 1000 different initial configurations and whole hysteresis loops were performed.

Figure 3. shows a comparative plot of **jump size distribution** histograms for different system sizes. Jump size distribution in terms of our model corresponds to the avalanche size distribution of the experiments, and it is the most relevant distribution function in the study of the BN. From the graph we can read some properties of the distribution function: (i) The jump size distribution histogram has scaling behavior over more then three decades of data for $N_s = 10000$ with scaling exponent -1.6. (ii) No relevant exponential cut-off is detectable. Only the histogram for $N_s = 3000$ exhibits a slight exponential tail. As the system size increases the distribution approaches power law and the cut-off vanishes. (iii) Since for $N_s = 10000$ we do not detect exponential cut-off anymore, we can affirm that this histogram already indicates the trend that would be followed in the thermodynamic limit. (iv) The finite size effect has a weak influence on the scaling exponent, since it increases slightly from -1.7 (obtained for $N_s = 3000$) until -1.6 for $N_s = 10000$. (v) As expected for smaller system size the scaling regime is also shorter. By the other hand for smaller systems less data are obtained because an avalanche cannot be larger then the system itself. For example (read data from Fig. 3.): in the $N_s = 10000$ case the probability of occurrence for an avalanche that spans over 3000 spins is nonzero, but a same-sized avalanche is impossible to occur in a system that consists of only 3000 spins.

The fact that our simulation results indicate a power-law distribution in the thermodynamic limit means that jump (avalanche) sizes exhibit a scale-invariance. This characteristic is expected to be common for all types of crackling noises.

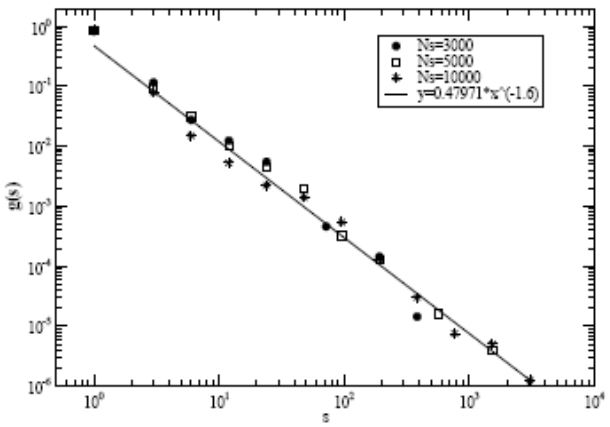

Figure 3. Jump-size distribution. $N_s = 3000$ (filled circles); $N_s = 5000$ (empty squares); $N_s = 10000$ (stars). The latter fitted with power-law: $g(s) = 0.48 \cdot s^{-1.6}$ (solid line)

Figure 4. (left) shows a comparative plot of **signal duration distribution** histograms for increasing system sizes. In experiments this quantity measures the length of a Barkhausen jump (measured as a voltage peak induced in the surrounding coil) on time scale. Since in our model the driving rate (step) of the external driving field is equivalent with the time evolution in real systems, signal duration in the model counts the consecutive dB steps (simulation steps) when magnetization jumps occur, i.e. when $\Delta M \neq 0$.

From the graph the following properties can be read: (i) The signal duration distribution histogram has scaling behavior over more then three decades of data for $N_s = 10000$ with scaling exponent -1.61. (ii) In the case of small systems ($N_s = 3000$ black circles) a clear exponential cut-off is observable. As the system sizes is increased the exponential tail reduces, and for $N_s = 10000$ the histogram can be well fitted with pure power function. This change from power-law with exponential cut-off to simple power-law as the model system's size increases underlines the generally accepted conception that the cut-off is due to the finite sizes effect. (iii) For $N_s = 10000$ we do not detect exponential cut-off anymore. This means that in a system with $N_s = 10000$ does not exhibit measurable finite size effect, thus the signal duration histogram indicates the trend that would be followed if the system would be increased to infinity. (iv) In a similar manner like in the case of the jump sizes distribution histogram, finite size effects have a slight influence on the value of the scaling exponent: it changes from -1.7 ($N_s = 3000$) to -1.61 ($N_s = 10000$).

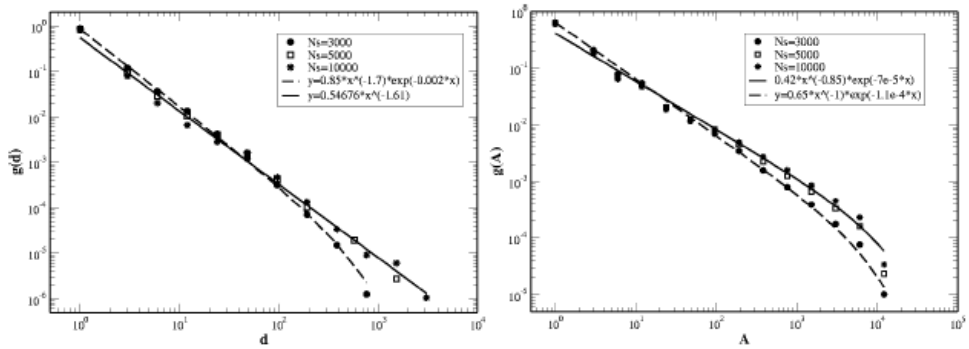

Figure 4.: (left) Signal duration distribution. Ns = 3000 (filled circles); Ns = 5000 (empty squares); Ns = 10000 (stars). The latter fitted with power-law: $g(d) = 0.55 \cdot d^{-1.61}$ (solid line); (right) Signal area distribution. Ns = 3000 (filled circles); Ns = 5000 (empty squares); Ns = 10000 (stars). The latter fitted with: $g(A) = 0.42 \cdot A^{-0.85} \cdot e^{-7 \cdot 10^{-5} \cdot A}$ (solid curve)

Figure 4. (right) shows a comparative plot of **signal area distribution** histograms for increasing system sizes. In experiments signal area measures the area under a voltage peak, thus the dimension of this area is Voltage $\times$ Time. In the present model the equivalent quantity is the area under a magnetization jump with length ΔB (the duration of the signal) and height ΔM. Thus the signal area is a quantity measured in $B \times M$ units. From the graph we can conclude that: (i) The histograms exhibit scaling-law with exponential cut-off over four decades of data. The histogram for $N_s = 10000$ is well fitted with formula: $g(A) = 0.42 \cdot A^{-0.85} \cdot e^{-7 \cdot 10^{-5} \cdot A}$. (ii) For smaller system sizes scaling regime is shorter comparative to larger system sizes and exponential cut-off appears sooner and is more relevant. This observation is in accordance with the conception that the cut-off appears due to the finite size effect. (iii) In contrast to the former distribution histograms, the signal area distribution histogram still exhibits exponential tail even for $N_s = 10000$. For larger systems the scaling regime is longer, the cut-off appears later and becomes less relevant. These results indicate the tendency that in the thermodynamic limit one should obtain pure power-law distributions.

4. Conclusions

The simple 1D Ising-type model elaborated to reproduce magnetization phenomena in ferromagnets reproduces successfully the statistical properties of magnetization phenomena, and in particular BN. The shape of the hysteresis loops is in qualitative agreement with the experimental magnetization curves, and the occurrence of large number of discrete Barkhausen jumps is correctly reproduced. The model captures the main elements of the microscopic domain-wall dynamics.

The studied distribution functions of the jump sizes, durations and areas show scaling behavior over several decades of data. This result is qualitatively in agreement with the experimental results. However, we cannot expect exact numeric correspondence of the critical exponents found in the experiments with those given by the model for several reasons: (1) the experimental results are very sensitive on the special characteristics of the material under study and the experimental setup; (2) this model is a very simple 1D model at mesoscopic scale and its purpose is to reproduce the main general characteristics of magnetic domain-wall dynamics without the intention to focus on special properties of particular materials.

The present model has two main advantages compared to other well known spin models like RFIM: first, the pinning effect is taken into account realistically in this model since the pinning centers act only on domain

boundaries; second, the demagnetization effect is included in the present model, which is very important in real magnetic materials. This property was ignored in numerous previous models, or taken into account in a very complicated manner, so it made the calculations and simulations very difficult.

The model in its present form was studied at zero temperature. Due to the used Hamiltonian formalism it is easy to be studied at any finite temperature as well. Our further goalis to use this model in order to study the influence of temperature and driving frequency on the dynamic susceptibility in ferromagnetic materials.

REFERENCES

1. G. Durin and S. Zapperi, cond-mat/0404512, 2004
2. J. P. Sethna, K. A. Dahmen, Ch. R. Myers, Nature, **410**, 242 (2001)
3. D. Spasojevic, S. Bukvic, S. Milosevic, H. E. Stanley, Phys. Rev. E **54**, 2531 (1996)
4. P. Plewka, J.J. Zebrowski, M. Urbanski, Phys. Rev. E **57**, 6422 (1998)
5. K. P. O'Brien, M. B. Weissman, Phys. Rev. E **50**, 3446 (1994)
6. B. Alessandro, C. Beatrice, G. Berotti, A. Montorsi, J. Appl. Phys. **68**. 2901, 2908 (1990)
7. G. Durin, P. Cizeau, S. Zapperi, H.E. Stanley, J. Phys. IV France **8**, Pr2-319 (1998)
8. O. Narayan, Phys. Rev. Lett. **77**, 3855 (1996)
9. J. Urbach, R. Madison, J. Markert, Phys. Rev. Lett. **75**, 276 (1995)
10. S. Zapperi, P. Cizeau, G. Durin, and H. E. Stanely, Phys. Rev. B **58**, 6353 (1998)
11. J. P. Sethna, K. Dahmen, S. Kartha, J. A. Krumhansl, B. W. Roberts, and J. D. Shore, Phys. Rev. Lett. **70**, 3347 (1993)
12. O. Perkovic, K. Dahmen, J.P. Sethna, Phys. Rev. B **59**, 6106 (1999)
13. E. Vives and A. Planes, Phys. Rev. B **50**, 3839 (1994)
14. E. Vives and A. Planes, Phys. Rev. B **63**, 134431 (2001)
15. K. Kovacs, Y. Brechet and Z. Neda, Model. Sim. Mat. Sci. **13**, 1-12 (2005)
16. R. Burridge and L. Knopoff, Bull. Seis. Soc. Amer. **57**, 341 (1967)